Universidad Autónoma de Madrid
Facultad de Ciencias
Departamento de Física Teórica de la Materia Condensada

Programa de doctorado de Física de la Materia Condensada

Spin Dependent Electron Transport through Single and Double Quantum Dot Systems

Tesis para optar al grado de Doctor en Ciencias Físicas presentada por:

Carlos Fco. López-Monís de Luna

Directora:
Dra. Gloria Platero Coello

Codirector:
Dr. Jesús Iñarrea las Heras

Tutor:
Dr. Carlos Tejedor de Paz

Madrid, Octubre de 2011

Agradecimientos

En primer lugar quiero agradecer a mis directores, Gloria y Jesús, y en especial a Gloria, por la haberme dado la impagable oportunidad de hacer una tesis, por haber siempre confiado en mí, por su infatigable apoyo y por haberme abierto el camino de la investigación científica.

Quiero dedicar un agradecimiento especial en primer lugar a Clive Emary, por las maravillosas discusiones de las que tanto he aprendido, sobre todo a pensar y a mimar los detalles, y a disfrutar con la ciencia. Y, en segundo lugar, pero no menos importante, a Mathias Lunde, por su infinita generosidad y su fino sentido crítico.

Agradezco a Allan MacDonald por haberme acogido en su grupo en Austin (Texas), a María y Pete, y en especial a Jeil, quién en todo momento estuvo pendiente de mí.

Agradezco a Tobias Brandes, por haberme dado la oportunidad de trabajar en su grupo en Berlín, la cual ha sido una experiencia fundamental tanto en el plano científico como en el personal. Durante este período he podido disfrutar de la experiencia investigadora en un equipo maravilloso, por eso quiero agradecer a Gerold y a Gernot, a los que siempre podías acudir cuando surgía alguna duda, a Jung y Anja, mis compañeros de despacho con los que tantas horas he compartido, y en especial a Philip y Alex, con los que pude construir un relación que espero dure por muchos años. También quería agradecer, fuera del terreno científico, a Justin, por su hospitalidad.

De la universidad Carlos III quiero agradecer a Luis Bonilla, por sus siempre valiosas aportaciones.

En el Insitituto quiero agradecer a Ricardo, que ha sido mi compañero desde el inicio hasta el final, comenzamos juntos y terminamos juntos, y por el camino disfrutamos juntos. A Rafa, mi *hermano* mayor, con quién he dado mis primeros pasos y junto al que sigo caminando, y por mucho tiempo espero. A Jángel, qué se puede decir de Jángel que no se haya dicho ya!, pero diré que le estoy agradecido por su generosidad y compañerísmo. Y a Rebeca, libre y voluntariosa, gracias, no cambies.

Quiero agradecer a los *antidiluvianos*, me refiero Ivan Gerardus, el chupa-puertas del planeta de los cinco soles, al *temible* José de Jesús Araiza, el zacatecano y a Ricardo el Grande, qué tiempos gloriosos vivimos su compañía. Y de esa horda (con todo el respeto del mundo), aunque más presentes a Samuel y a Ramón, por intuir que amanecer no es poco.

Quiero agradecer a toda la gente con la que he compartido despacho, empezando por Lucía, cuántas conversaciones y divagaciones, cuantas palabras buscadas en el diccionario, cuantas canciones y anécdotas. A Merche, y a Diego por su gran sentido del humor. A Virginia, ejemplo de trabajora donde las haya. Y, en este momento, a Mariano y a Chicho, que han contribuido a que esta recta final se mucho más llevadera. Sin duda, he tenido mucha suerte con todos las personas con las que he compartido despacho, espero al menos no haberles incordiado demasiado.

Quiero agradecer a mis compañeros de las comidas y meriendas, con los que he compartido el día, al menos durante un tiempo, Fer. de Juan, Gladys y, en particular, a David.

Quiero agradecer a los demás miembros del grupo de Gloria que aun no he mencionado, María, Fernando, Sigmund, Robert y Álvaro, por los seminarios y discusiones compartidas.

De mis compañeros del grupo teoría no pueden faltar Alberto (y Fátima), Juan Luis, Débora, César y Rafa, de los primeros tiempos, y Fito, Unai y Héctor, del presente. Y de otros grupos del instituto no quier olvidarme de Laura y Covadonga.

Quiero agradecer a los músicos del instituto con los que he tenido la oportunidad de tocar e improvisar, Miguel, Wagner, Simone, Luis y Alex.

Fuera del instituto quiero en primer lugar dar gracias a mis amigos. A Elena y a Jose, a los que debo gran parte de lo que soy y siento como mis hermanos, pues siempre hemos estado juntos. A Javi, mi compañero durante la tesis, con el que he madurado como persona y científico, y con el que construido un profunda amistad. A Mario -y su esposa Andrea-, con el que comparto a través de maravillosas conversaciones dos de las cuestiones más importantes de mi vida, la libertad y el arte. A Fernando, por su voluntad, su valentía y sobre todo, su lucidez. Y a Alex y a Santiago, mis compañeros de siempre.

No quiero olvidarme de La Mongoose Band, el Combo, Pocholo y mi maestro Miguel Juanilla, gracias por la música.

Quiero agradecer muy especialmente a mi familia. A mi madre y a mi hermana, las mujeres más fuertes, luchadoras y valientes que he conocido, por las que siento una profunda y eterna admiración. Y a mi padre que, a su manera, ha luchado para que yo llegue a ser lo que soy.

Quiero agradecer a María Dolores, José Manuel, Teresa (y Carlitos) y Manuel (y Lucía), también mi familia, su gran apoyo.

Agradezco también a Julio y a Inma, que en muchos aspectos han sido como padres para mí.

Y, por último, y más importante, quiero agredecer a mi amor, mi compañera, María, por *ser* juntos.

List of acronyms

2DEG Two-dimensional electron gas. (*Gas bidimensional de electrons.*)

QD Quantum dot. (*Punto cuántico.*)

DQD Double quantum dot. (*Doble punto cuántico.*)

CB Coulomb blockade. (*Bloqueo de Coulomb.*)

SB Spin blockade. (*Bloqueo de espín.*)

HF Hyperfine. (*Hiperfina.*)

ST Singlet-triplet. (*Singlete-triplete.*)

EOM Equation of motion. (*Ecuación de movimiento.*)

Abstract

The following thesis belongs to the field of condensed matter physics, and particularly, to the theory of low-dimensional mesoscopic systems. In this dissertation, we have drawn special attention to electron transport through quantum dot systems. Over the last decade, the spin of current electrons that tunnel through a set of quantum dots have been thoroughly investigated experimental and theoretically, due to the interaction of this quantum degree of freedom with the spins of the surrounding environment. A wide number of works have shown that this spin interaction is responsible for relaxation and decoherence phenomena. This thesis is devoted to the study of spin scattering processes between electrons confined in quantum dot systems and a spin bath resembling the environment; special attention is payed to the effect that these processes have on the electron current through the system. The thesis is structured as follows.

In chapter one, we present a brief review of quantum dots, focusing mostly on the basic concepts underlying the theoretical model that is used in this thesis for the description of a quantum dot system.

Chapter two consists of a short introduction to electron transport through quantum dots. Fundamental time scales of the transport process are firstly reviewed. Then, we summarize the different transport regimes that are possible depending on the relation between the time scales discussed in the first part of the chapter.

Through chapters three and four, we study the effect of the hyperfine interaction on the electron transport through a double quantum dot system in the spin blockade regime. In chapter three, we develop a theoretical model for describing the spin relaxation process due to the interaction between the spins of the electrons trapped in the double quantum dot and the spins of the nuclei of the the host material; we also derive the rate equations for describing the hyperfine-mediated transport process. In chapter four, we present the results obtained by solving the rate equations obtained in the previous chapter.

In chapter five, we investigate electron transport through a single quantum dot. The electrons in the dot are anisotropically coupled to a large isolated spin -resembling a spin bath- in presence of an external magnetic field. We develop a model for describing the system, and derive and find the solutions of the equations of motion that describe the dynamics of the quantum dot electrons and the large spin.

Finally, the thesis has three short appendices. In the first one, a simple model for describing the spin-blockade regime is developed. In the second appendix, we review the hyperfine structure in atomic systems before deriving the hyperfine Hamiltonian for quantum dots. The third appendix consist of additional calculations to chapter five, including a detailed derivation of the equations of motion.

Resumen

La presente tesis pertenece al campo de la física de la materia condensada, y en particular, a la teoría de sistemas mesoscópicos de baja dimensionalidad. Esta tesis se concentra en el transporte electrónico a través de puntos cuánticos. Durante la última década, el espín de los electrones de una corriente eléctrica que circula a través de un sistema de puntos cuánticos ha sido investigada exhaustivamente experimental y teóricamente, debido a su interacción con los espines del entorno en el que se encuentra el sistema. Gran cantidad de trabajos han comprobado que esta interacción entre espines es responsable de fenómenos de relajación y decoherencia. Esta tesis está consagrada al estudio de procesos de dispersión entre electrones confinados en un sistema de puntos cuánticos y un baño de espines que describe el entorno; se ha prestado special atención al efecto que tienen estos procesos sobre la corriente eléctrica a través del sistema. Esta tesis está estructurada de la siguiente forma.

En el capítulo uno presentamos un breve resumen sobre puntos cuánticos, concentrándonos sobre todo en los conceptos básicos detrás del modelo teórico usado a lo largo de esta tesis para describir sistemas de puntos cuánticos.

El capítulo dos consiste en una breve introducción al transporte electrónico a través de puntos cuánticos. En primer lugar, se describen las escalas de tiempo fundamentales en el proceso transporte electrónico. A continuación, resumimos los diferentes regímenes de transporte posibles en función de la relación entre las escalas de tiempo introducidas en la primera parte del capítulo. Para finalizar, presentamos el modelo usado en esta tesis para describir transporte electrónico a través de puntos cuánticos.

A lo largo de los capítulos tres y cuatro, estudiamos el efecto de la interacción hiperfina sobre el transporte electrónico a través de un doble punto cuántico en el régimen de bloqueo de espín. En el capítulo tres desarrollamos un modelo teórico para describir los procesos de relajación de espín debidos a la interacción entre los espines de los electrones atrapados en el doble punto cuántico y los espines de los núcleos del material hospedador; además, derivamos ecuaciones de balance para describir el proceso de transporte mediado por la interacción hiperfina. En el capítulo cuatro presentamos los resultados obtenidos al resolver las ecuaciones de balance obtenidas en el capítulo anterior.

En el capítulo cinco investigamos el transporte electrónico a través un punto cuántico. Los electrons del punto cuántico están acoplados anisotrópicamente a un espín *grande* (i.e., cuyo momento angular es mucho mayor que 1/2) y aislado -que modeliza un baño de espines- en presencia de un campo magnético externo. Desarrollamos un modelo para describir dicho sistema, y derivamos y encontramos la soluciones para las ecuaciones de movimiento que describen la dinámica de los electrons del punto cuántico y del espín grande.

Finalmente, la tesis posee tres apéndices. En el primero se desarrolla un modelo sencillo para describir el régimen de bloque de espín. En el segundo apéndice, repasamos la estructura hiperfina en átomos para luego derivar el hamiltoniano de la interacción hiperfina en puntos cuánticos. El tercer apéndice consiste en cálculos complementarios al capítulo cinco, incluyendo una derivación detallada de las ecuaciones de movimiento.

Contents

List of Figures

Chapter 1

Brief review of quantum dots

In this chapter we review the concept of quantum dot. The description shows that a quantum dot is obtained by confining in all spatial dimensions an electron in the conduction band of a semiconductor. We revise the band structure of a solid and, in particular, the conduction and the valence bands. The effective mass approximation is reviewed, which allows to consider electrons in the conduction band as free electrons by changing there mass to include the band structure. And finally, we will see that a quantum dot is described through a confinement potential defined by the characteristic length of the quantum dot.

1.1 Motivation

To grasp the beauty of the concept of *quantum dot* we should fall back on to two leading milestones of modern physics: atomic systems and condensed matter systems. In an atom, the attractive Coulomb force between the nucleus and the electrons in it confines the electrons in a tiny region ($\sim 10^{-10}$m) around the nucleus. Due to this confinement, the energy of an electron bound in an atom is quantized in a set of discrete levels. Thereby, energy quantization in atoms can be understood as a *size effect* due to their microscopic nature. In a solid, electrons are confined due to the attractive Coulomb forces between the electrons and the underlying ion-lattice structure of the crystal. In this case, the energy of an electron is allowed to have quasi-continuous values within zones known as energy bands, interspersed with forbidden energy zones known as band gaps. This energy band structure of a solid is a consequence of the periodicity of the underlying crystal lattice, which gives rise to a periodic ion potential. In brief, quantum dots are a solid-state systems in which a few electrons are confined to a region small enough so that the energy quantization effects are observable in its physical properties. Therefore, quantum dots are a new kind of systems that emerge in a land between atoms and solids.

1.1.1 Brief history of quantum dots

The history of quantum dots belongs to the history of research on quantum size effects and quantum confinement. In [1, 2] they place the appearance of the first *quantum dots*[1] in the year 1932, when H. P. Rooksby published an article where he related the yellow or red colors of some silicate glasses to tiny inclusions of CdSe and CdS [4].[2] Nevertheless, it seems that research in quantum dots did not begin as a proper field until the first half of the eighties. At this time, going beyond Rooksby's work, A. I. Ekimov *et al.* [5, 6] studied the size dependence of exciton absorption spectrum of the semiconductor microcrystals CdSe and CdS -among others- grown in a dielectric matrix. Similar experiments were performed at the same time by R. Rossetti *et al.* (e.g. in [7, 8]). In both experiments, they claimed that there observations could be understood as quantum size effects resulting from confining an electron and hole in a small volume (10-100 Å) [8].[3] During the second half of the eighties, M. A. Reed *et al.* [3] published one of the first works (if no the first) with evidence of transport through a the discrete spectrum of states of a quantum dot. In this work we can find probably the first appearance of the name "quantum dot", applying to a "semiconductor heterostructures with quantum confinement to zero dimensions". Finally, in the early nineties quantum dots began to be regarded as *artificial atoms* [9,10]. Many works were devoted to study similarities and differences between real atoms and these artificial ones. For e.g., S. Tarucha *et al.* [11] analyzed the electronic states of a few-electron vertical quantum dot. For low magnetic fields they observed antiparallel filling of the spin-degenerate states, whereas near to zero magnetic field, they noticed the filling of states with parallel spins in accordance with Hund's rule. At this time, the field had already exploded and since then the field has been constantly evolving.

Despite their three-dimensional character, electrons can be made to behave as if they were only free to move in fewer dimensions. This might be accomplished by trapping them in a confinement potential that restricts their motion in either one (*quantum wells*), two (*quantum wires*) or even three (*quantum dots*) dimensions to discrete energy levels. If the separation between these energy levels is much larger than the thermal energy (k_BT), the quantization will be important, the electrons will appear to be frozen into the ground state and no motion will be possible in the confined dimensions. Notice that low dimensional electron systems are, therefore, low dimensional only in the dynamical sense [2, 12, 13].[4]

[1] The designation *quantum dot* however, did not appear until the late eighties, see for e.g. [3].

[2] Most probably this hypothesis belongs only to [1], since the last name Rooksby is misspelled *Rocksby* in both texts.

[3] Surprisingly or not, neither of them cite each other's works neither Rooksby's, though according to [2], Efimov's and Rossettis's experiments explain Rooksby's observations.

[4] The term *dimensions* can refer to the confinement potential, thus, we say that the potential has one, two or three dimensions; however, it can also refer to the motion of an electron, thus, we say that the system where it lives is one, two or three dimensional if the electron is free to move in one, two or three dimensions, respectively, or zero-dimensional, if the electron is completely trapped in all directions, as in the case of quantum dots.

Although quantum dot fabrication is a highly nontrivial subject, under the theoretical framework of this thesis, we choose to delve into their theoretical description throughout this short introduction. Moreover, despite the several models for describing a quantum dot on a theoretical level, in the following sections we will present a rather simple theoretical description, though probably the most intuitive. Furthermore, this description will serve as a starting point for the works presented in this thesis.

1.2 Band structure

Ordinary quantum dots are made by confining the motion of the valence and the conduction band electrons in all three spatial dimensions. Therefore, in this section we first provide a brief review of the electronic band structure of a solid.

The non-relativistic Hamiltonian[5] for a solid-state system is written as the sum of the kinetic and potential energy of the ionic system and the electronic system treated independently, and the Coulomb interaction between the two systems:

$$\hat{H} = \left(\hat{T}_{\text{ion}} + \hat{V}_{\text{ion}-\text{ion}}\right) + \left(\hat{T}_{\text{el}} + \hat{V}_{\text{el}-\text{el}}\right) + \hat{V}_{\text{el}-\text{ion}}. \tag{1.1}$$

Under the so called *phenomenological lattice approach* [14], we take the experimental determination of the crystal structure, lattice parameters and elasticity constants as input to the theory, and from there calculate the electronic and phononic properties. This lattice has an energy E_{latt} and a potential energy $\hat{V}_{\text{el}-\text{latt}}$ associated with it, both coming from a combination of $\hat{T}_{\text{ion}}$, $\hat{V}_{\text{ion}-\text{ion}}$ and $\hat{V}_{\text{el}-\text{ion}}$ in the original Hamiltonian (1.1). At finite temperature, the ions can vibrate around their equilibrium positions with the total electric field acting as a restoring force. These vibrations can be described in terms of quantized harmonic oscillators, giving rise to the concept of phonons. The non-interacting part of the phonon field is described by the Hamiltonian $\hat{H}_{\text{ph}}$. The electrons are described by their kinetic energy $\hat{T}_{\text{el}}$, their mutual interaction, $\hat{V}_{\text{el}-\text{el}}$, and the vibrating part, i.e., the phonons, $\hat{V}_{\text{el}-\text{ph}}$. The latter term must be there since a vibrating ion is giving rise to an electrical vibrational potential influencing the electrons. The Hamiltonian for the phenomenological lattice model changes $\hat{H}$ of Eq. (1.1) into

$$\hat{H} = \left(E_{\text{latt}} + \hat{H}_{\text{ph}}\right) + \left(\hat{T}_{\text{el}} + \hat{V}_{\text{el}-\text{el}}\right) + \left(\hat{V}_{\text{el}-\text{latt}} + \hat{V}_{\text{el}-\text{ph}}\right). \tag{1.2}$$

At zero temperature, the ions are not vibrating except for their quantum mechanical zero point motion. Therefore, we can drop all the phonon related terms in the Hamiltonian. Moreover, neglecting the electron-electron interaction, known as the *independent electron approximation*, one arrives at the Hamiltonian used in Bloch's

[5] Namely, the Hamiltonian describing the gross structure, neglecting fine structure effects due to relativistic corrections (for e.g., spin-orbit interaction).

theory to describe non-interacting electrons in a static and periodic ion lattice,

$$\hat{H}_{\text{Bloch}} = \hat{T}_{\text{el}} + \hat{V}_{\text{el-latt}}(\mathbf{r}) \tag{1.3}$$

where $\hat{V}_{\text{el-latt}}(\mathbf{r}+\mathbf{R}) = \hat{V}_{\text{el-latt}}(\mathbf{r})$ for any lattice vector $\mathbf{R}$.

1.2.1 One-dimensional lattice potential

In order to show with a simple example how the band structure of a crystal arises because of the periodic character of the lattice potential, we now calculate the eigenfunctions and eigenenergies of the Bloch Hamiltonian (1.3) for an electron in a one-dimensional lattice potential. Therefore, consider a solid in which the positive ions comprise a uniform array of fixed ions, where the distance between the sites is a. Inside the solid the lattice potential is periodic with the distance a

$$\hat{V}_{\text{el-latt}}(x) = \hat{V}_{\text{el-latt}}(x+a). \tag{1.4}$$

For simplicity, let us consider the special case of the *Kronig-Penney potential* [15] (Fig. 1.1a). We shall assume periodic boundary conditions, which is equivalent to consider that the lattice potential lies on a circle (Fig. 1.1b). The Bloch Hamiltonian is then:

$$\hat{H}_{\text{Bloch}} = \frac{\hat{p}^2}{2m} + \hat{V}_{\text{el-latt}}(x). \tag{1.5}$$

The eigenfunctions correspond to *Bloch wave functions*,

$$\phi(x) = e^{ikx}u(x) \tag{1.6}$$

$$u(x) = u(x+a). \tag{1.7}$$

In this model, $\phi(x) = \phi(x+Na)$, where N is the number of ions in the solid. Thus, $e^{ikNa} = 1 \rightarrow kNa = 2\pi n$, $n = 0, \pm 1, \pm 2 \ldots$ The ratio $2\pi/ka = N/n$ is a rational number, thus the eigenfunctions are periodic. The allowed values of k form a discrete spectrum ($k_n = 2\pi n/Na$). Since N is very large, the difference between successive values of k is very small and the spectrum of the allowed values of k may be taken to comprise a continuum. The shape of this wave function suggests the manner in which the crystal structure influences the wave functions of particles propagating through the crystal. This structure is primarily contained in the periodic factor $u(x)$, which in turn includes the lattice constant a and which modulates the free-particle form, e^{ikx}.

Let us now briefly review how to obtain the eigenenergy spectrum. In the well domain,

$$\phi_{\text{I}}(x) = Ae^{ik_1 x} + Be^{-ik_1 x} \quad (0 \leq x \leq b) \tag{1.8}$$

$$E = \frac{\hbar^2 k_1^2}{2m}. \tag{1.9}$$

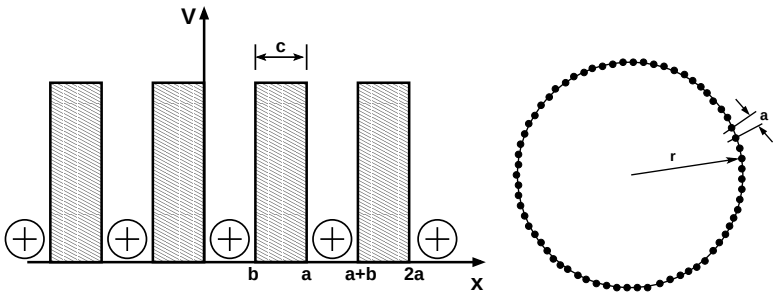

(a) (b)

Figure 1.1: a) The Kronig-Penney model for a potential due to fixed ion sites separated by a distance a. b) Ring model of a one-dimensional periodic potential. Black dots represent positive ion sites. For N sites and $N \gg 1$, $Na \simeq 2\pi r$.

In the barrier domain (with $E > V$),

$$\phi_{\rm II}(x) = Ce^{ik_2 x} + De^{-ik_2 x} \quad (b \le x \le b + c = a) \tag{1.10}$$

$$E - V = \frac{\hbar^2 k_2^2}{2m} \tag{1.11}$$

and for the case $E < V$,

$$\phi_{\rm II}(x) = Ce^{\kappa x} + De^{-\kappa x} \quad (b \le x \le b + c = a) \tag{1.12}$$

$$V - E = \frac{\hbar^2 \kappa^2}{2m} \tag{1.13}$$

Assuming $\phi(x)$ and $\phi'(x)$ to be continuos, after some algebra one obtains the following dispersion relations

$$\cos k_1 b \cos k_2 c - \frac{k_1^2 + k_2^2}{2k_1 k_2} \sin k_1 b \sin k_2 c = \cos ka \tag{1.14}$$

$$k_1^2 - k_2^2 = \frac{2mV}{\hbar^2} \tag{1.15}$$

and

$$\cos k_1 b \cosh \kappa c - \frac{k_1^2 + \kappa^2}{2k_1 \kappa} \sin k_1 b \sinh \kappa c = \cos ka \tag{1.16}$$

$$k_1^2 + \kappa^2 = \frac{2mV}{\hbar^2} \tag{1.17}$$

These dispersion relations can be only solved numerically. The values of the right-hand-side of equations (1.14) and (1.16) lies between $+1$ and -1 ($|\cos ka| \le 1$). Therefore, the only solutions to equations (1.14) and (1.16) are values of E for

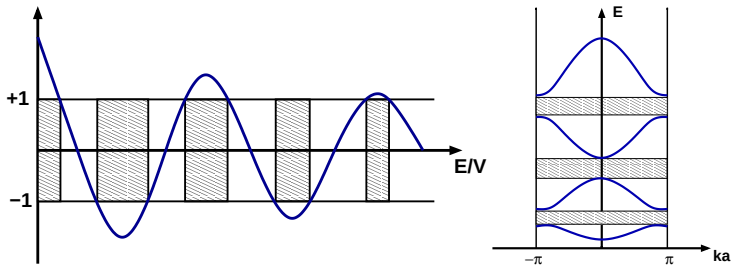

(a) (b)

Figure 1.2: a) Band structure of the energy spectrum of the Kronig-Penney Hamiltonian. The dashed regions represent the forbidden regions, while the regions in between represent the energy bands. The only eigenenergies are those values for which the left-hand side of Eq. (1.14) or Eq. (1.16) (blue line) lies between ± 1. b) The first four bands in the reduced-zone scheme (blue lines). Also shown the first three energy gaps (dashed regions).

which their left-hand-side (LHS) fall in the same interval, that is, values of E for which

$$-1 \leq \text{LHS} \leq +1 \tag{1.18}$$

The values of E that violate this condition are excluded from the energy spectrum. Condition (1.18) gives rise to a *band structure* of the spectrum of eigenenergies. Fig. 1.2a illustrates the band property of a particle in a periodic lattice potential. Note that the value of E that satisfies equations (1.14) and (1.16) for a given value of kd satisfies it for $kd + 2\pi n$. Thus, it suffices then to draw all bands in the single interval $-\pi \leq ka \leq \pi$. This gives the *reduced-zone* description of eigenstates (Fig. 1.2b). These consist of very closely packed discrete energies and constitute all eigenenergies of the Hamiltonian. Thus, the discrete nature of the energy spectrum is a consequence of the boundedness of the system, however, the quasi-continuous character of the spectrum (bands of closely packed levels) reflects the propagating nature of the eigenstates.

Finally, the spectrum of eigenenergies of electrons in an actual three-dimensional crystalline solid is similar to that of the Kronig-Penney model. In the three-dimensional case a band structure for the allowed energy eigenvalues is also obtained, and the electrons in a solid occupy these bands. In the following section we will see how solids can be classified depending on how electrons are distributed in these bands. In particular, this will lead us to semiconductor materials, which is today the standard substrate for quantum dot fabrication.

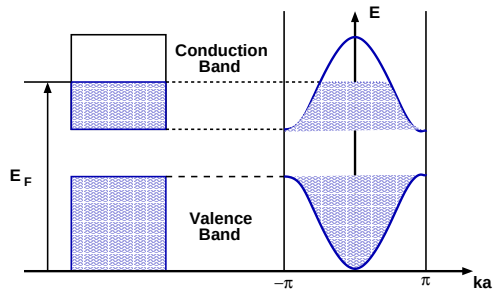

Figure 1.3: The diagram to the right indicates the manner in which electrons fill the corresponding bands in the reduced-zone description for the idealized one-dimensional model. The Fermi energy E_F is also shown.

1.2.2 Semiconductors

An electron in a completely filled band can carry no current, since it has no nearby unoccupied states. Within the independent electron model this result is the basis for the distinction between insulators and metals: In the ground state of an insulator all bands are either completely filled or completely empty; in the ground state of a metal at least one band is partially filled. We can characterize insulators by the *energy gap* between the top of the highest filled band(s) and the bottom fo the lowest empty band(s). A solid with an energy gap will be nonconducting at zero temperature. When the temperature is not zero there is a non vanishing probability that some electrons will be thermally excited across the energy gap into the lowest unoccupied bands, which are called, in this context, *conduction bands*, leaving behind unoccupied levels in the highest occupied bands, called *valence bands* (Fig. 1.3).[6] The thermally excited electrons are capable of conducting, and the hole-type conduction can occur in the band out of which they have been excited.

Solids that are insulators at zero temperature, but whose energy gaps are such of a size that thermal excitation can lead to observable conductivity at temperatures below the melting point, are known as *intrinsic semiconductors*. The conduction of an *extrinsic* semiconductor is due to the presence of impurities in the sample. The most striking feature of semiconductors is that, unlike metals, their electrical resistance declines with rising temperature; i.e, they have a "negative coefficient of resistance". However, as pointed in the previous section, in this thesis we are interested in semiconductors because they are frequently used for quantum dot fabrication. A more comprehensive survey on semiconductors can be found in, e.g., the books in Ref. [12, 16]

[6] The Fermi energy is the energy of the highest occupied electron level.

1.3 Effective mass approximation

In general, the electronic band structure of a material is often to complicated to compute. However, to calculate electronic and optical properties of quantum dots it is usually enough to focus only on the valence band, the conduction band or both bands at most. Therefore, in this section we briefly review the so-called effective mass approximation [12], which essentially assumes that the band structure of the crystalline semiconductor can be included by changing the mass of the electron.

Consider a perturbation is added to a perfect crystal (e.g., a confinement potential). The Schrödinger equation is

$$[\hat{H}_{\text{Bloch}} + \hat{V}(\mathbf{r})]\psi(\mathbf{r}) = E\psi(\mathbf{r}) \tag{1.19}$$

where $\hat{H}_{\text{Bloch}}$ is the perfect crystal Hamiltonian (1.3) and $\hat{V}(\mathbf{r})$ is the perturbation. As in the previous section, for simplicity, let us consider the one-dimensional case, hence

$$\hat{H}_{\text{Bloch}}\phi_{nk}(x) = \varepsilon_n(k)\phi_{nk}(x), \tag{1.20}$$

where $\phi_{nk}(x)$ are the Bloch wave functions (1.6), n is the band index and k the wavevector. These solutions form a complete set. The wave function $\psi(x)$ of the system with the perturbation can be expanded in terms of the Bloch wave functions as

$$\psi(x) = \sum_n \int_{-\pi/a}^{\pi/a} \tilde{\chi}_n(k)\phi_{nk}(x)\frac{dk}{2\pi} \tag{1.21}$$

where $\tilde{\chi}_n(k)$ are expansion coefficients. This has both a summation over all bands n and an integral in k's over the reduced-zone to include all states.

The first assumption of the effective mass approximation is to consider the wave functions from only one band to play a significant role, so the summation over n can be dropped. In the case of a semiconductor this will be the either conduction band or the valence band.

The second assumption is to consider that the states from only a small region of k-space contribute significantly to the integral in (1.21). Thereby, we shall assume that most of the variation in $\phi_{nk}(x)$ with k comes form the plane wave, so that the term $u_{nk}(x)$ in (1.6) can be treated as independent of k over a small region of k-space. Thus, we write

$$\phi_{nk}(x) \approx \phi_{n0}(x)e^{ikx} = u_{n0}(x)e^{ikx} \tag{1.22}$$

for small values of k.

With these two simplifications, the wave function (1.21) takes the form of a Fourier transform,

$$\psi(x) \approx \phi_{n0}(x)\int_{-\pi/a}^{\pi/a} \tilde{\chi}(k)e^{ikx}\frac{dk}{2\pi} = \phi_{n0}(x)\chi(x). \tag{1.23}$$

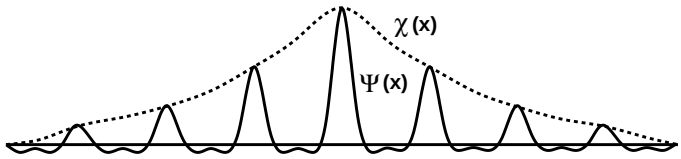

Figure 1.4: Wave function around a quantum dot, showing the envelope function $\chi(x)$ that modulates the Bloch function to give the full wave function $\Psi(x)$.

Therefore, the wave function can be written approximately as the product of the Bloch function of the local extremum of the host's energy band and an *envelope function* $\chi(x)$: $\psi(x) \approx \phi_{n0}(x)\chi(x)$. We have assumed that $\tilde{\chi}(k)$ contains only a small range of wave numbers, which in turn means that $\chi(x)$ must be a slowly varying function in real space (Fig. 1.4).

We next need an equation for the envelope function. To obtain it we substitute the expansion (1.21) into the Schrödinger equation (1.19), and make the reduction to the single band. The effect of $\hat{H}_{\text{Bloch}}$ gives

$$\begin{aligned} \hat{H}_{\text{Bloch}}\psi(x) &= \hat{H}_{\text{Bloch}} \int_{-\pi/a}^{\pi/a} \tilde{\chi}(k)\phi_{nk}(x)\frac{dk}{2\pi} = \int_{-\pi/a}^{\pi/a} \tilde{\chi}(k)\varepsilon_n(k)\phi_{nk}(x)\frac{dk}{2\pi} \\ &\approx \phi_{n0}(x) \int_{-\pi/a}^{\pi/a} \tilde{\chi}(k)\varepsilon_n(k)e^{ikx}\frac{dk}{2\pi}. \end{aligned} \tag{1.24}$$

Next, we expand the energy band as a power series in k: $\varepsilon_n(k) = \sum_m a_m k^m$. Substituting this expansion in the previous equations and making use of the general property of the Fourier transform of the derivative [7] it becomes

$$\hat{H}_{\text{Bloch}}\psi(x) \approx \phi_{n0}(x) \sum_m a_m \left(-i\frac{d}{dx}\right)^m \chi(x) \equiv \phi_{n0}(x)\varepsilon_n\left(-i\frac{d}{dx}\right)\chi(x). \tag{1.25}$$

The remaining terms $\hat{V}\psi$ and $E\psi$ in (1.19) simply multiply the wave function. The common factor of $\phi_{n0}(x)$ cancels to leave

$$\left[\varepsilon_n\left(-i\frac{d}{dx}\right) + \hat{V}(x)\right]\chi(x) = E\chi(x) \tag{1.26}$$

which is a Schrödinger equation for the envelope function, containing an *effective Hamiltonian*. The Bloch functions have vanished, as has the periodic potential of the host, in favor of a complicated kinetic energy that contains the band structure.

[7] $k^m\tilde{f}(k) \to (-id/dx)^m f(x)$. The inverse Fourier transform of $\tilde{\chi}(k)k^m$ is

$$\int_{-\pi/a}^{\pi/a} \tilde{\chi}(k)k^m e^{ikx}\frac{dk}{2\pi} = \left(-i\frac{d}{dx}\right)^m \chi(x).$$

The effective Hamiltonian would still be extremely complicated if we retained the full band structure for $\varepsilon_n(k)$. However, since we have already assumed that the wave function is drawn from only a small region of k-space, we can simplify $\varepsilon_n(k)$ to be consistent with this. For instance, the bottom of the conduction band is approximately,

$$\varepsilon_n(k) \approx E_C + \frac{\hbar^2 k^2}{2m^*} \tag{1.27}$$

and the replacemente $k \to (-id/dx)$ gives,

$$\varepsilon_n(k) \approx E_C - \frac{\hbar^2}{2m^*}\frac{d^2}{dx^2}. \tag{1.28}$$

Substituting this into the effective Schrödinger equation (1.26) gives,

$$\left[-\frac{\hbar^2}{2m^*}\frac{d^2}{dx^2} + \hat{V}(x)\right]\chi(x) = (E - E_C)\chi(x) \tag{1.29}$$

which is a Schrödingder equation that resembles that of free electrons except for the effective mass m^*, with the energy measured from the bottom of the conduction band.

For the three-dimensional case it becomes:

$$\left[-\frac{\hbar^2}{2m^*}\nabla^2 + \hat{V}(\mathbf{R})\right]\chi(\mathbf{R}) = (E - E_C)\chi(\mathbf{R}). \tag{1.30}$$

Therefore, the *effective mass approximation* allows the ions in the lattice to be completely ignored, and electrons in the conduction band (or holes in the valence band) to be treated as if they were free particles, but with a different mass. In brief, the effective mass approximation is a refined version of the *free electron approximation* (Sommerfeld model), which simple neglects the effect of the lattice ions from the beginning without further considerations.

Finally, being this thesis devoted to electron transport through quantum dots, onwards we shall consider the *single-band* effective mass approximation, since in this case just electrons in the conduction band are taken into account.

1.3.1 Envelope function approximation

In order to use the effective mass approximation for quantum dots, the system must be treated as a bulk sample. We assume that the single-particle electron wave function can be written in terms of Bloch functions and that the concept of effective mass still has a meaning in a small quantum dot. Therefore, we consider the band structure of these mesoscopic systems as only weakly changed in comparison to the corresponding bulk material. This approximation, called the *envelope function approximation*, is valid when the size of the quantum dot is much larger than the *lattice constant* of the material.

Under this approximation, one assumes that only the envelope part of the wavefunction is modified through the existence of the confinement potential (see below). Typical quantum dot sizes range from a few hundred to many thousands of atoms. For e.g., a typical self-assembled quantum dot has a base of $\sim 30\,\text{nm}$ and a height of $\sim 5\,\text{nm}$, so the dot itself may contain $\sim 10^5$ atoms [2].

1.4 Confinement potential

In the last section we saw that the motion of electrons in the conduction band could be described by means of the effective Schrödinger equation (1.30). In this section, we consider the perturbation in equation (1.30) to be a potential $\hat{V}_{\text{conf}}(\mathbf{r})$ responsible for the three-dimensional confinement of these electrons. A quantum dot is ultimately described by this *confinement potential*. The domain of $\hat{V}_{\text{conf}}(\mathbf{r})$ determines the size of the quantum dot, and causes the conduction band to be quantized into a ladder of electron levels. This phenomenon, which is known as the *quantum size effect*, leads to atomic like behavior as the bulk bands become quantized. In the artificial atom picture, the confinement potential plays the role of the potential of the nucleus in a real atom.

Quantum confinement effects arise as soon as the linear extension of the quantum dot is smaller than the electron's de Broglie wavelength,

$$\lambda_e = \frac{h}{m^* v} \tag{1.31}$$

where h is Planck's constant, and m^* and v are the effective mass and the velocity of an electron in the conduction band, respectively. At the end of the last section we saw that for the effective mass approximation to be safe, the size of the quantum dot had to be much larger than the lattice constant of the material. Therefore, the length of the quantum dot is bounded to the range

$$\boxed{\text{lattice constant} \ll \text{QD length} \ll \lambda_e.} \tag{1.32}$$

This relation, however, provides only an heuristic estimation of the size of a quantum dot, since both the lattice and the electron velocity are temperature dependent magnitudes. For example, the velocity of electrons due to thermal energy is

$$v_{th} = \sqrt{\frac{3k_B T}{m^*}} \quad \Rightarrow \quad \lambda_e = \frac{h}{\sqrt{3m^* k_B T}} \tag{1.33}$$

where T is the temperature and k_B Boltzmann's constant. Thus, for a given temperature the length of the quantum dot must be smaller than $h/\sqrt{3m^* k_B T}$. For e.g., in GaAs semiconductors the electron effective mass is $m^* = 0.067 m_0$, where m_0 is the electron rest mass. Therefore, if $T = 1\,\text{K}$ the wavelength associated with thermal excitations is $\lambda_e \simeq 417\,\text{nm}$, meaning quantum dots have to be in the nanometer scale in order to observe quantum confinement effects.

Finally, it is also necessary to take into account that for the energy quantization in the quantum dot to be relevant k_BT must be smaller than the distance between the quantized energy levels, though this will be discussed later.

Some examples of quantum dots

In this section we give a few examples of confinement potentials used to model real quantum dots. The specific form of $\hat{V}_{\text{conf}}(\mathbf{r})$ depends on the geometry of the quantum dots, which in the end depends on the fabrication technique used for confining electrons.

Probably the most intuitive example of quantum dots are *nanocrystals*, also known as colloidal quantum dots [6, 8]. To describe this type of quantum dots the simplest confinement potential used is a spherical well potential, i.e, a *particle-in-a-sphere* model [17]

$$\hat{V}_{\text{conf}}(r) = \begin{cases} 0, & 0 < r < R_0, \\ \infty, & \text{otherwise}, \end{cases} \tag{1.34}$$

where $|\mathbf{r}| = r$ and R_0 is the radius of the sphere. In this case, the three-dimensional Schrödinger equation (1.30) is exactly solvable. The eigenenergy spectrum of the particle is given by

$$E_{n,l} = \frac{\hbar^2 \alpha_{n,l}^2}{2m^* R_0^2}, \tag{1.35}$$

where $\alpha_{n,l}$ is the n-th zero of l-th order spherical Bessel function. These are atomic-like orbitals which can be labeled by the quantum numbers n $(1, 2, 3\ldots)$, l $(0, 1, 2\ldots)$ and m $(-l \leq m \leq l)$. Note that the energy depends on $1/R_0^2$ and, thus, depends strongly on the size of the sphere. However, this kind of quantum dots are particularly interesting for investigating optical properties, while in this thesis we have concentrated on their electronic properties.

An example of more suitable quantum dots for studying the properties of an electric current made to pass through them are semiconductor *vertical* [11] and *lateral* [18] quantum dots. In a nutshell, these type of quantum dots are made by confining the motion of electrons in a two-dimensional electron gas by means of advanced growth techniques (vertical dots, see Fig. 1.5a) or electrical gates (lateral dots, see Fig. 1.5b).

Electrons in a quantum well form a two-dimensional electron gas. A common choice of the confinement potential for this kind of quantum dots is a two-dimensional parabolic potential [13],

$$\hat{V}_{\text{conf}}(x, y) = \frac{1}{2} m^* \omega_0^2 (x^2 + y^2), \tag{1.36}$$

where we have considered that electrons in the 2DEG are confined in the z-direction. The energy spectrum of a single electron confined in a parabolic dot and subjected to an external magnetic field was first investigated theoretically eighty years ago in

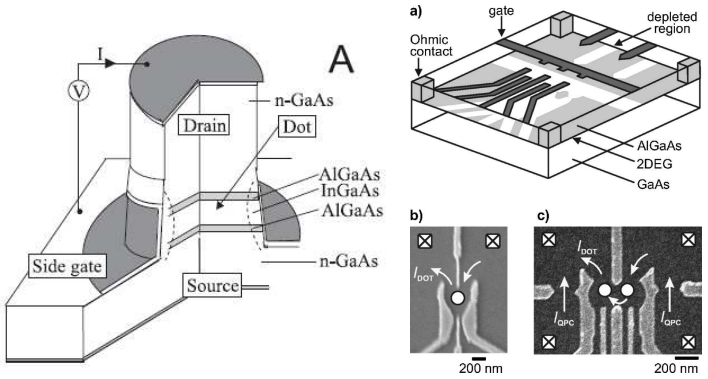

(a) (b)

Figure 1.5: a) Vertical quantum dot fabricated from semiconductor heterostructures using electron beam lithography and etching techniques [21]. b) Lateral quantum dot defined by metal surface electrodes on top of a 2DEG [22].

the works of V. Fock [19] and C. G. Darwin [20]. They found that the eigenenergy spectrum obtained when solving the Schrödinger equation (1.30) is

$$E_{n,l} = (2n + |l| + 1)\hbar\Omega - \frac{1}{2}l\hbar\omega_c \tag{1.37}$$

where $\Omega^2 = \omega_c^2/4 + \omega_0^2$, $\omega_c = eB/m^*c$ is the cyclotron frequency and B is the intensity of the magnetic field. Here, the two quantum numbers are, $n = 0, 1, \ldots$ the radial quantum number, and $l = 0, \pm 1, \ldots$ the azimuthal quantum number. The interest on this model system today is the realization of that ideal calculation in today's state of the art low-dimensional semiconductor nanostructures.

Finally, quantum dots with more exotic geometries can be fabricated, like pyramidal or lens shaped dots.

Chapter 2

Brief review of electron transport through quantum dots

In this chapter we review the basic ideas of electron transport through quantum dots. Firstly, the relevant time scales are seen, namely, the lifetime of an electron in a quantum and the phase-coherence time. Secondly, from these time scales we define the coherent and sequential tunneling regimes, and discuss Coulomb Blockade and single electron tunneling phenomena. Finally, we introduce the Anderson impurity model, which is the model that is going to be used throughout this thesis.

2.1 Simple picture: the double-barrier model

In the previous chapter, we saw that under certain assumptions conduction band electrons in a semiconductor can be treated as free electrons with an effective mass. Furthermore, we saw that these electrons could be trapped by means of a confinement potential, which was used to define the quantum dot systems.

In order to describe electron transport through a quantum dot, an intuitive choice for the confinement potential in the Schrödinger equation (1.30) is simply a tunnel junction or *double-barrier* structure, consisting of two tunneling barriers in series (Fig. 2.1). An electron confined in a double-barrier well can tunnel through one of the barriers and escape from the well, thus, no true bound states are formed. Nevertheless, the electron may remain in the well for a long time if the barriers are thick enough, and a remnant of the bound states persists as *resonant* or *quasi-bond* states. The energy of these states cannot be precisely defined but is spread into a range $\hbar/\tau_d$, where τ_d is the lifetime of the electron in the quantum dot before it tunnels away.

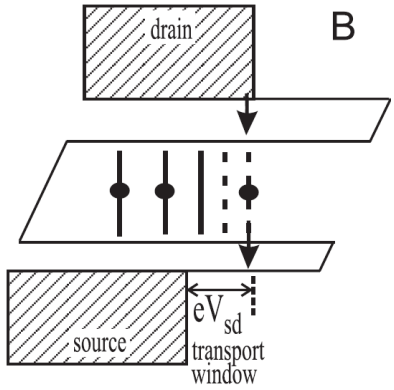

Figure 2.1: Tunnel junction schematic energy (horizontal axis) diagram. Dashed regions are occupied electron states in the source and the drain contacts. Two electrons are permanently trapped in the quantum dot. The third electron can tunnel through on of the states that lie in the transport window.

The double-barrier well is embedded in the conduction band, thus, the region which is not within the barriers is going to define the *leads*. These can be regarded as two independent electron reservoirs coupled through the quantum dot structure. The electrons in the leads can be regarded as non-interacting, which is not always the case for the electrons in the quantum dot. Consider now that for e.g. a positive bias voltage V is applied to the right lead, which lowers the energies there by $-eV$. Each lead has now its own chemical potential, μ_L on the left and μ_R on the right. These differ by the applied bias giving $\mu_L - \mu_R = eV$, which will finally drive an electron current through the quantum dot.

2.1.1 Phase-coherence time

The *phase-coherence* time is the scale on which the electrons preserve their quantum mechanical phase, i.e., the scale on which the wave function evolves according to the one-particle Schrödinger equation. Phase-coherence is needed for the appearance of quantum interference effects. However, it is lost when the interaction with its environment is considered. Therefore, phase-coherence is conserved only during a finite time τ_ϕ. For e.g., if an electron interacts with another electron or with a phonon through an inelastic scattering event its energy changes, and hence, so does the evolution of its phase. Due to these processes the phase of the electron wave acquires some randomization or *dephasing*, and its phase-coherence time becomes finite.

In general, only scattering processes during which an excitation of the environment (a phonon, an electron-hole excitation, etc.) is created or destroyed, leads to a loss of phase-coherence. These processes are typically inelastic and connected

to a transfer of energy, however, other types of scattering events that alter the environment without energy transfer like, for e.g., spin-flip processes can also lead to decoherence. In turn, the scattering of electrons off static impurities is always elastic. However, even though the phase of electrons may be modified in these scattering processes, this happens in a well-defined way and does not destroy the phase coherence effects [14]. Finally, as temperature is lowered quantum mechanical coherence becomes more important. For e.g., at low temperatures a dominant dephasing mechanism is electron-electron scattering, which scattering rate is proportional to $(k_B T)^2$. Hence, $\tau_\phi \propto (k_B T)^{-2}$ can become very large at sufficiently low temperatures. A common technique for computing τ_ϕ is Fermi's Golden rule, which will be studied in detail in the next chapter. A more comprehensive survey on phase relaxation processes can be found in, for e.g., the books [14, 23].

As will be discussed in the following sections, the ratio between the lifetime of an electron in a quantum dot τ_d, and the phase-coherence time τ_ϕ, is used to define the different transport regimes that describe electron tunneling through quantum dots.

2.2 Transport regimes

In this section we briefly summarize the different regimes for electron transport through quantum dots.

2.2.1 Coherent tunneling

When the average time an electron spends in a quantum dot resonant state is much less than the phase-coherence time, $\tau_d \ll \tau_\phi$, the electrons transmit from the left to the right lead in a single quantum mechanical process whose probability can be calculated from a Schrödinger equation. Hence, the current can be obtained by calculating the coherent transmission through the structure. This is called the *coherent tunneling* regime [12,23]. This phenomenon is based on the phase coherence of the entire process, i.e., the transport through the quantum dot (the double-barrier) is fully phase coherent. In this regime electrons can be treated as pure waves, a coherent scattering state extended from the left lead throughout the dot region until the right lead exists.

A special feature of the coherent tunneling regime is that near a resonance the transmission probability of the double-barrier reaches its maximum value of unity if the structure is symmetric, meaning there is a perfect transmission, however opaque the individual barriers. This is the most dramatic case of coherent transport and is known as *resonant tunneling*. A common underlying assumption, however, in the coherent tunneling regime is that the charge carriers are viewed as non-interacting particles.

2.2.2 Sequential tunneling

Opposite to the coherent tunneling regime, i.e., when $\tau_d \gg \tau_\phi$, the phase-coherence is broken while the electron is in the quantum dot. This regime is called weak or *sequential tunneling*, since the events can be ordered in time:

1. An electron tunnels from a lead to the dot,
2. its phase-coherence is lost, and
3. the electron tunnels from the dot to a lead again.

Hence, the sequential tunneling regime assumes that the time spent in the quantum dot is much longer than the time between tunneling events. In other words, the time scale between tunneling events is assumed to be the largest in the problem.

In this regime Coulomb interactions play a dominant role for the transport properties. This is understood physically because if the charge tends to be localized in the quantum dot the flow of electrons becomes correlated due to the Coulomb interactions. The degree of correlation is controlled by the charging energy, which is the Coulomb energy cost for adding or removing electrons to the quantum dot (see below). Thus, because of this charging effect it is not possible to consider the electrons as independent quantities and, hence, a many-body approach is needed.

2.2.3 Coulomb blockade and single electron tunneling

In this section we resume the tunnel junction picture for quantum dots discussed at the beginning of this chapter. We consider the junction as a capacitor with an extremely low capacity, C, due to the ultra small area of the junction. The energy corresponding to the charging of the capacitor having such a small capacitance with one single electron is

$$E_C = \frac{e^2}{2C}. \tag{2.1}$$

This charging energy is a consequence of the Coulomb interaction between the electrons and influences the transport properties of the tunnel junction in the following way.

The charge

$$Q = CV \tag{2.2}$$

induced by the bias voltage on the capacitor does not need to be an integer multiple of the elementary charge e. However, the tunneling of the electron through the barrier changes this charge by exactly one elementary charge. Therefore, immediately after the tunneling event the charge in the capacitor is

$$Q' = Q - e. \tag{2.3}$$

The electronic transport is based on tunneling through the barriers and since tunneling conserves energy, these processes are suppressed when the energy needed to

change the charge on the capacitor exceeds the available energy. Energy conservation requires

$$\epsilon_1 + \frac{Q^2}{2C} = \epsilon_2 + \frac{(Q-e)^2}{2C} \tag{2.4}$$

where ϵ_1 and ϵ_2 correspond to the one-particle energy of the electron before and after tunneling, respectively. Replacing Q by the voltage (Eq. (2.2)) and writing the voltage in terms of the chemical potential difference $\mu_L - \mu_R$ one gets,

$$\epsilon_1 - \epsilon_2 + \mu_L - \mu_R = \frac{e^2}{2C} = E_C. \tag{2.5}$$

At low temperatures, if the energy of the electron before tunneling is below the chemical potential $\epsilon_1 \leq \mu_L$, and the energy after tunneling is above the other chemical potential $\epsilon_2 \geq \mu_R$, one has $\epsilon_1 - \epsilon_2 \leq \mu_L - \mu_R$ and obtains from the previous equation the condition for tunneling

$$2eV = 2(\mu_L - \mu_R) \geq E_C. \tag{2.6}$$

This is the origin of the suppression of the linear conductance through ultra small capacitances, measured in series with a large resistance, and explains the voltage offset

$$V_{of} = \frac{E_C}{2e} \tag{2.7}$$

in the current voltage characteristic. This suppression of the conductance is a consequence of the granular structure of electronic charge combined with electron-electron interactions. It is called *Coulomb blockade* effect and can lead to *single electron tunneling* [18, 23–28].

Therefore, to observe the Coulomb blockade effect, two main conditions must be fulfilled:

- Thermal fluctuations should be small enough in order not to provide the charging energy. This requires
$$E_C \gg k_B T, \tag{2.8}$$
a condition that can be fulfilled in small quantum dots and low temperatures.

- Quantum fluctuations should be smaller than the charging energy. According to a rough estimate, the energy uncertainty is due to the lifetime τ_d of the electron in the junction before it tunnels out, i.e., the time it takes to restore the initial charge Q on the capacitor. If this time is short, the energy uncertainty smears out the charging energy. Thus,
$$E_C \gg \Delta E = \frac{\hbar}{\tau_d} \tag{2.9}$$
must be fulfilled. If one estimates the time scale from the exponential decay of the capacitor charge in a classical RC circuit, $\tau_d \approx RC$, this results in the

requirement to have a resistance of

$$R \gg \frac{1}{\pi}\frac{h}{e^2} \tag{2.10}$$

in series.

Two important paradigms of mesoscopic transport have been discussed in this brief review, namely, resonant tunneling and single-electron tunneling. The physical mechanisms underlying the two phenomena are fundamentally different. Resonant tunneling arises from the *wave* nature of electrons which gives rise to energy quantization in confined structures, while single-electron tunneling arises from the *particle* nature of electrons which gives rise to charge quantization. Resonant tunneling is not observed if the distance between the barriers is long enough that the spacing between the allowed energy levels is negligible compared to k_BT. But single-electron tunneling can still be observed, as long as the capacitance is small enough that the electrostatic energy of a single electron (e^2/C) exceed k_BT. This effect would be absent if charge were not quantized.

2.3 Anderson impurity model

In the previous section we described the transport regimes for electron tunneling through quantum dots. In this thesis we have focused on the Coulomb blockade regime, where we have seen that electron-electron scattering plays a dominant role and single-electron tunneling occurs.

As mentioned earlier, because of the charging effect it is not possible to consider the electrons as independent quantities, so a many-body approach is needed. Therefore, for studying a system consisting of a quantum dot coupled to leads we use the Anderson impurity model [29,30]. The capacitor model seen in the previous section is most relevant when there are many single particle levels within the energy window of interest. However, when the dot is so small that the single particle levels inside are resolved, an Anderson type model is more suitable. The impurity model was originally introduced by P. W. Anderson for studying localized magnetic states in metals [31]. The Hamiltonian model is

$$\hat{H} = \sum_{i=1}^{N_0}\left[\frac{\hat{\mathbf{p}}_i^2}{2m} + \hat{V}_{\mathrm{el-latt}}(\mathbf{r}_i) + \hat{V}_{\mathrm{imp}}(\mathbf{r}_i)\right] + \frac{1}{2}\sum_{i\neq j}^{N_0}\frac{e^2}{|\mathbf{r}_i - \mathbf{r}_j|}, \tag{2.11}$$

for N_0 electrons. This is just the Hamiltonian for solid-state system discussed in the previous chapter (section 1.2), plus the potential describing the impurity, $\hat{V}_{\mathrm{imp}}$. The first two terms correspond to the Bloch Hamiltonian (1.3), where $\hat{\mathbf{p}}_i$ is the momentum operator and m the electron rest mass. Recall that the electron-lattice interaction, $\hat{V}_{\mathrm{el-latt}}(\mathbf{r}_i)$, can be incorporated in the kinetic term through the effective mass approximation (section 1.3). This allows to ignore the band structure of

the crystal and focus only on the electrons in the conduction band. The impurity potential, $\hat{V}_{\rm imp}$, is now the confinement potential that describes the quantum dot (section 1.4). The last term in Eq. (2.11) accounts for the Coulomb interaction between electrons, $\hat{V}_{\rm el-el}$. Finally, the Hamiltonian (2.11) becomes

$$\hat{H} = \sum_{i=1}^{N_0} \left[\frac{\hat{\mathbf{p}}_i^2}{2m^*} + \hat{V}_{\rm conf}(\mathbf{r}_i) \right] + \frac{1}{2} \sum_{i \neq j}^{N_0} \frac{e^2}{|\mathbf{r}_i - \mathbf{r}_j|}. \tag{2.12}$$

The last step is to represent this Hamiltonian in the second quantization form. To do this we need to choose a specific basis. In the Anderson model the basis is given by the continuum set of **k**-states in the leads, and the quantum dot isolated states. In this thesis, however, we consider that transport occurs only through the single state of the quantum dot, meaning the excited states are assumed to be out of the bias window. Thus, the quantum dot has only one orbital level. Moreover, we ignore the orbital degeneracy, and treat it as a state with spin degeneracy only. Therefore, a generalized state field operator for representing Eq. (2.12) is the following

$$\hat{\Psi}_{\mathbf{k}\sigma}(\mathbf{r}) = \psi_d(\mathbf{r})\hat{d}_\sigma + \sum_{\mathbf{k}} \psi_{\mathbf{k}}(\mathbf{r})\hat{c}_{\mathbf{k}\sigma}, \tag{2.13}$$

where $\psi_d(\mathbf{r})$ and $\psi_{\mathbf{k}}(\mathbf{r})$ are the quantum dot and **k**-state electron wave functions, respectively, in the envelope function approximation (section 1.3); the operators $\hat{d}_\sigma$ and $\hat{c}_{\mathbf{k}\sigma}$ annihilate an electron with spin σ in the the dot and the lead, respectively.

We now evaluate the first terms of the Hamiltonian (2.12) for the field operator (2.13),

$$\begin{aligned} \int d\mathbf{r}\, \hat{\Psi}^\dagger_{\mathbf{k}\sigma}(\mathbf{r}) \left[\frac{\hat{\mathbf{p}}_i^2}{2m^*} + \hat{V}_{\rm conf}(\mathbf{r}_i) \right] \hat{\Psi}_{\mathbf{k}\sigma}(\mathbf{r}) &= \sum_{\mathbf{k}\sigma} \epsilon_{\mathbf{k}} \hat{c}^\dagger_{\mathbf{k}\sigma}\hat{c}_{\mathbf{k}\sigma} + \sum_{\sigma} \epsilon_d \hat{d}^\dagger_\sigma \hat{d}_\sigma \\ &+ \sum_{\mathbf{k}\mathbf{k}'\sigma} V_{\mathbf{k}\mathbf{k}'} \hat{c}^\dagger_{\mathbf{k}'\sigma}\hat{c}_{\mathbf{k}\sigma} \\ &+ \sum_{\mathbf{k}\sigma} \left(\gamma_{\mathbf{k}} \hat{c}^\dagger_{\mathbf{k}\sigma}\hat{d}_\sigma + \gamma^*_{\mathbf{k}} \hat{d}^\dagger_\sigma \hat{c}_{\mathbf{k}\sigma} \right) \end{aligned} \tag{2.14}$$

The first two terms on the right hand side are the unperturbed parts of the Hamiltonian for the continuum state and the quantum dot, where $\epsilon_d/\epsilon_{\mathbf{k}}$ is the energy of the dot/**k**-level. The third term involves the scattering of the continuum states from the impurity. This problem may be solved by scattering theory [29]. The last term is the tunneling term, where $\gamma_{\mathbf{k}}$ is the tunneling matrix element between the lead and the quantum dot. This term describes processes whereby the electron hops off the quantum dot and becomes a continuum state or vice versa. It is a consequence of the nonorthogonality of the continuum and local wave functions. Note, however, that the spin direction is maintained during the tunneling process. If the field operators (2.13) are chosen to be eigenstates of the Hamiltonian which includes the

scattering term $V_{\mathbf{k}\mathbf{k}'}$, this Hamiltonian becomes the *Fano-Anderson model*

$$\hat{H}_{FA} = \sum_{\mathbf{k}\sigma} \epsilon_{\mathbf{k}} \hat{c}^{\dagger}_{\mathbf{k}\sigma} \hat{c}_{\mathbf{k}\sigma} + \sum_{\sigma} \epsilon_d \hat{d}^{\dagger}_{\sigma} \hat{d}_{\sigma} + \sum_{\mathbf{k}\sigma} \left(\gamma_{\mathbf{k}} \hat{c}^{\dagger}_{\mathbf{k}\sigma} \hat{d}_{\sigma} + \gamma^{*}_{\mathbf{k}} \hat{d}^{\dagger}_{\sigma} \hat{c}_{\mathbf{k}\sigma} \right). \quad (2.15)$$

This model may be solved exactly [29].

Finally, the term in Eq. (2.12) involving the electron-electron interaction evaluated for the field operator (2.13) is

$$\int d\mathbf{r}_i d\mathbf{r}_j \, \frac{e^2}{|\mathbf{r}_i - \mathbf{r}_j|} \hat{\Psi}^{\dagger}_{\mathbf{k}\sigma}(\mathbf{r}_i) \hat{\Psi}_{\mathbf{k}\sigma}(\mathbf{r}_i) \hat{\Psi}^{\dagger}_{\mathbf{k}\sigma}(\mathbf{r}_j) \hat{\Psi}_{\mathbf{k}\sigma}(\mathbf{r}_j) \quad (2.16)$$

The Anderson model only regards the Coulomb interaction for electrons in the quantum dot, meaning it considers only four local operators:

$$\begin{aligned} & U \hat{d}^{\dagger}_{\sigma} \hat{d}^{\dagger}_{\sigma'} \hat{d}_{\sigma''} \hat{d}_{\sigma'''} \\ & U = \int d\mathbf{r}_i d\mathbf{r}_j \, |\psi_d(\mathbf{r}_i)|^2 \frac{e^2}{|\mathbf{r}_i - \mathbf{r}_j|} |\psi_d(\mathbf{r}_j)|^2. \end{aligned} \quad (2.17)$$

If the quantum dot is non degenerate, as in an s-orbital (which will be the case considered in this thesis), then the two electrons can be in the same site only in opposite spin states. The spin indexes must pair up as $\sigma''' = \sigma$ and $\sigma'' = \sigma'$, so we get

$$U \hat{n}_{\uparrow} \hat{n}_{\downarrow} \quad (2.18)$$

where $\hat{n}_{\sigma}$ is the occupation number operator associated to the σ-level. Therefore, the Hamiltonian we arrive to is the one in Eq. (2.15) plus this interaction term

$$\hat{H}_A = \sum_{\mathbf{k}\sigma} \epsilon_{\mathbf{k}} \hat{c}^{\dagger}_{\mathbf{k}\sigma} \hat{c}_{\mathbf{k}\sigma} + \sum_{\sigma} \epsilon_d \hat{d}^{\dagger}_{\sigma} \hat{d}_{\sigma} + \sum_{\mathbf{k}\sigma} \left(\gamma_{\mathbf{k}} \hat{c}^{\dagger}_{\mathbf{k}\sigma} \hat{d}_{\sigma} + \gamma^{*}_{\mathbf{k}} \hat{d}^{\dagger}_{\sigma} \hat{c}_{\mathbf{k}\sigma} \right) + U \hat{n}_{\uparrow} \hat{n}_{\downarrow} \quad (2.19)$$

which is known as the *Anderson model* [14, 29, 31]. The Hamiltonian describes the interaction of the conduction electrons with a quantum dot.

The Fano-Anderson model (2.15) and the Anderson model (2.15) are going to be the models used throughout this thesis to study spin dependent electron transport through single and double quantum dot systems.

Chapter 3

Hyperfine interaction in electron transport in double quantum dots: Theory

Through this chapter and the the next one, we analyze electron spin relaxation in electronic transport through coherently coupled double quantum dots in the spin blockade regime. In particular, we focus on hyperfine interaction as the spin relaxation mechanism. We pay special attention to the effect of the dynamical nuclear spin polarization induced by the electronic current on the nuclear environment. We discuss the behavior of the electronic current and the induced nuclear spin polarization versus an external magnetic field for different hyperfine coupling intensities and interdot tunneling strengths. We take into account, for each magnetic field, all hyperfine mediated spin relaxation processes coming from the different opposite spin levels approaches. We find that the current as a function of the external magnetic field shows a peak or a dip, and that the transition from a current dip to a current peak behavior is obtained by decreasing the hyperfine coupling or by increasing the interdot tunneling strength. We give a physical picture in terms of the interplay between the electrons tunneling out of the double quantum dot and the spin flip processes due to the nuclear environment.

3.1 Introduction

In the last decade solid-state spintronics and quantum computing have experienced a great development. In particular, quantum dots (solid-state fabricated zero dimensional devices) have been widely investigated both experimentally and theoretically. For quantum computing and quantum information they have become major candidates for implementing quantum bit units [32] (*qubits*), but also from a fundamental

point of view, since quantum dots resemble artificial atoms, they are highly interesting systems for studying basic atomic physics. In this context, spin decoherence and relaxation are among the most desirable mechanisms to be understood since they represent the main sources of quantum computing errors.

We investigate spin relaxation in double quantum dots (DQD). Spin Blockade (SB) [33] is a very suitable regime for attempting single electron spin manipulation because two electrons are trapped in a DQD, since Pauli Exclusion Principle avoids electron transport through the dots. Moreover, SB is attainable through transport experiments in DQDs in several materials. However, spin relaxation processes can partially destroy the SB releasing the trapped electrons, leading to a small, though still measurable leakage current ($\sim$ pA-fA) [33–37]. Spin-orbit coupling [38], cotunnelling [39, 40] and hyperfine (HF) interaction between the DQD electrons and the surrounding nuclei spins of the host material represent the main mechanisms for spin-relaxation. Depending on the material, one or more mechanisms may be involved collaborating or competing [34, 35, 37].

In this work, we study theoretically spin relaxation in a DQD in SB regime due to HF interaction with the lattice nuclei spins, which has been in the last years a very active field both experimentally [34, 35, 37, 41–48] and theoretically [49–54]. We pay special attention to the dynamical nuclear spin polarization *induced by the electronic leakage current* [44, 49, 53, 55, 56] emerging from the spin-relaxation transitions (Fig. 3.1). This effect is often not taken into account when studying the current through the DQD in SB regime.

In the present work we calculate both the electronic leakage current and the nuclei spin polarization induced by the electrons tunnelling through the DQD. In the SB regime, two electrons in the DQD can be either in a triplet or in a singlet state. Nevertheless, current is only allowed to pass through the DQD when they are in a singlet, otherwise they remain trapped in a triplet state. HF interaction mixes triplet and singlet subspaces, and thereby lifts SB. The mixing is due to the different HF interaction strengths, i.e., two different effective magnetic fields (induced Overhauser fields on the electrons by the nuclei), within each dot. In addition, scattering processes between electron and nuclei spins that lead to spin relaxation, also induce a non-negligible nuclear spin polarization as the current flows through the DQD. Moreover, this induced nuclear spin polarization itself, as we shall see below, modifies the mixing between the triplet and singlet subspaces, acting back on the electronic current through the DQD. Furthermore, we find that the Overhauser field proportional to the electron current induced nuclear spin polarization, is in general larger than the one obtained when just considering HF interaction as a random stationary magnetic field acting on the electron spins.

In previous works [53, 55, 56], the interdot tunnel coupling between the quantum dots was considered incoherent, namely, the system was assumed to be in the sequential interdot tunnelling regime. However, in the present work we focus on the resonant tunnel regime and we consider coherently coupled quantum dots (Fig. 3.1a). We have found in this case a different behaviour both for the current and the induced nuclear spin polarization with respect to previous works. In the coherent coupling

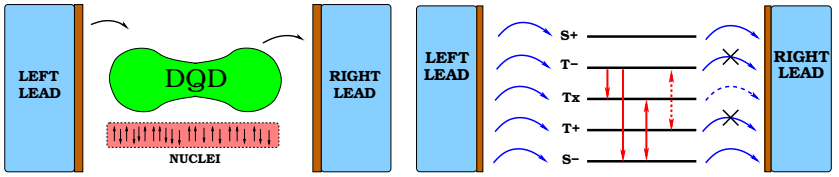

(a) DQD, leads and the lattice nuclei. (b) Transport scheme.

Figure 3.1: a) A coherently coupled DQD is coupled through tunnelling barriers to leads and to the surrounding nuclei of the host material. b) Transport scheme. Electrons tunnel from the left lead into the DQD states (solid blue arrows online). When electrons fall into the singlet states ($S_\pm$), tunnelling out of the DQD to the right lead is allowed (solid blue arrows online). However, when electrons fall into a triplet state ($T_\pm$) Pauli Exclusion principle prevents them from tunnelling out of the DQD into the right lead, thus, SB occurs. Finally, if electrons tunnel into the T_x state (a mixture of a singlet state and the antiparallel spins triplet T_0), they can only tunnel out of the DQD to the right lead if there is a net nuclear spin polarization (dashed blue arrow online), otherwise T_x becomes T_0, which is also a blocked state. Electrons trapped in $T_\pm$ states interact with the nuclei and relax to a singlet state or to the T_x state (solid red arrows online) through spin-flip processes. However, electrons in T_x state can also spin-flip back to a SB state (red dashed arrows online). Therefore, when electrons are in the T_x state there is a competition between the tunnelling rate from the T_x to the right lead, and the spin-flip rate from T_x to the $T_\pm$ triplets (a detailed discussion is given in section 3.3.1). We will show that this competition will give rise to different physical features in the tunnelling current as a function of an external magnetic field (see chapter 4).

regime, in addition to the two spin parallel triplets, there is a spin antiparallel triplet. Thus, in addition to the spin-flip transitions between the singlet and triplet states, spin-flip processes between triplet states are also present, and contribute to the nuclear spin polarization and the electronic leakage current. Furthermore, in the present model we find that the transition rates between the DQD and the leads depends on the nuclear spin polarization (Fig. 3.1b). This effect will lead to new features in the current through the DQD.

3.2 Hamiltonian and DQD eigenstates

The system we investigate is a DQD coupled to two uncorrelated electron reservoirs (leads) and to the nuclei spins of the surrounding host material (Fig. 3.1a). We consider a spin up and a spin down level in each dot. The Hamiltonian is the following:

$$\hat{H} = \hat{H}_{DQD} + \hat{H}_{leads} + \hat{V}_{LR} + \hat{V}_T + \hat{V}_{HF} \tag{3.1}$$

where $\hat{H}_{DQD}$ and $\hat{H}_{leads}$ are the Hamiltonians for the isolated DQD and the electron reservoirs, respectively, $\hat{V}_{LR}$ is the inter-dot tunnelling Hamiltonian, and $\hat{V}_T$ and $\hat{V}_{HF}$ correspond to the DQD coupling with the leads, and the HF interaction with the nuclei spins, respectively. We neglect cotunnelling processes because we consider that the tunnelling coupling through the contact barriers is much smaller than the thermal energy and the bias voltage [14]. Moreover, the energy of the DQD levels are strongly detunned respect to the contacts chemical potentials [39, 40].

We consider contact HF interaction, as we regard electronic wave functions with s like symmetry [57]. $\hat{H}_{DQD}$ and $\hat{V}_{LR}$ are:

$$\begin{aligned}\hat{H}_{DQD} &= \sum_{l\sigma}\epsilon_l\hat{n}_{l\sigma}+\sum_l U_l\hat{n}_{l\uparrow}\hat{n}_{l\downarrow}+U_{LR}\sum_{\sigma\sigma'}\hat{n}_{L\sigma}\hat{n}_{R\sigma'}+\sum_l g\mu_B B_{\rm ext}\hat{S}_{lz}\\ \hat{V}_{LR} &= t_{LR}\sum_\sigma\left(\hat{d}^\dagger_{L\sigma}\hat{d}_{R\sigma}+{\rm h.c}\right)\end{aligned}$$

where $l = L$ (left dot), R (right dot) and $\sigma =\uparrow,\downarrow$. $\hat{d}^\dagger_{l\,\sigma}$ ($\hat{d}_{l\,\sigma}$) creates (annihilates) an electron with spin σ and energy ϵ_l in the l-th dot. $\hat{n}_{l\sigma} = \hat{d}^\dagger_{l\sigma}\hat{d}_{l\sigma}$ is the occupation number operator and $\hat{\mathbf{S}}_l$ the electron spin operator. U_l (U_{LR}) is the intra-dot (inter-dot) Coulomb interaction, $B_{\rm ext}$ the external magnetic field and t_{LR} the tunnelling matrix element between the dots. We do not focus on any particular material, thus we take $g = 2$. $\hat{H}_{leads}$ and $\hat{V}_T$ are:

$$\begin{aligned}\hat{H}_{leads} &= \sum_{lk\sigma}\epsilon_{lk\sigma}\hat{c}^\dagger_{lk\sigma}\hat{c}_{lk\sigma}\\ \hat{V}_T &= \sum_{lk\sigma}\left(\gamma_{lk}\hat{c}^\dagger_{lk\sigma}\hat{d}_{l\sigma}+{\rm h.c.}\right)\end{aligned}\tag{3.2}$$

where $\hat{c}^\dagger_{lk\sigma}$ ($\hat{c}_{lk\sigma}$) creates (annihilates) an electron in the l-th lead with momentum $\mathbf{k}$, spin σ and energy $\epsilon_{lk\sigma}$. γ_{lk} are the tunnelling matrix elements between the dots and the contacts. Finally, the HF interaction term $\hat{V}_{HF}$ is:

$$\hat{V}_{HF} = \sum_{l=L,R}\sum_{i=1}^{N} A^l_i\,\hat{\mathbf{S}}_l\cdot\hat{\mathbf{I}}_i\tag{3.3}$$

where $A^l_i = \nu A|\Psi^l_0(\mathbf{r}_i)|^2$ is the HF coupling [58] between the i-th nuclei spin $\hat{\mathbf{I}}_i$ at site $\mathbf{r}_i$ and the electron spin $\hat{\mathbf{S}}_l$, where ν is the volume of a unit cell containing one nuclear spin, A characterizes the hyperfine coupling strength and $\Psi^l_0(\mathbf{r}_i)$ is the single-particle electronic wave function for dot l, evaluated at site $\mathbf{r}_i$. For simplicity, we only consider spin-$\frac{1}{2}$ nuclear species. The HF couplings for the left and right dots depend on the square modulus of the electron wave functions at the position of the nuclei, therefore, for realistic dots they are in principle different for each dot [59, 60]. We consider the case of homogeneous hyperfine couplings [61] within each dot, hence,

$A_i^l = A_l/N$, where N is total number of nuclear spins, and split $\hat{V}_{HF}$ (see Eq. (3.4)) in the following two terms:

$$\hat{V}_{HF} = \sum_{l=L,R} \frac{A_l}{N} \sum_{i=1}^{N} \left(\frac{1}{2} \left(\hat{S}_{l+}\hat{I}_{i-} + \hat{S}_{l-}\hat{I}_{i+} \right) + \hat{S}_{lz}\hat{I}_{iz} \right) = \hat{V}_{sf} + \hat{V}_z \ , \qquad (3.4)$$

where $\hat{S}_\pm = \hat{S}_x \pm \imath \hat{S}_y$ and $\hat{I}_\pm = \hat{I}_x \pm \imath \hat{I}_y$ are the raising and lowering operators for the electron and the nuclei spins, respectively. $\hat{V}_{sf}$ corresponds to the x-y-components, which are perpendicular to the external magnetic field and, thus, is responsible for the flip-flop transitions between electron and nuclei spins; and $\hat{V}_z$ corresponds to the z-component, which is parallel to the external field and, hence, contributes to the Zeeman splitting, as we will see below. We treat these two terms separately. For $\hat{V}_z$ we perform a mean-field approximation which gives [53]:

$$\hat{V}_z \to \hat{V}_z^{MF} = \frac{1}{2} \sum_l A_l \hat{S}_{lz} P \qquad (3.5)$$

where $P = (\langle N_\uparrow \rangle - \langle N_\downarrow \rangle)/N$ is the net nuclear spin polarization, and $\langle N_\uparrow \rangle$ ($\langle N_\downarrow \rangle$) is the average number of spin up (down) nuclei. $\hat{V}_z^{MF}$ is now equivalent to an effective magnetic field within each dot induced by the nuclei on the electrons (the Overhauser field), and proportional to the nuclear polarization given by:

$$B_{\text{nuc}}^{L(R)} = \frac{A_{L(R)} P}{2 g \mu_B}. \qquad (3.6)$$

This effective field is in general different for each dot [50], and gives rise to an effective Zeeman splitting within each dot that adds to the one produced by the external field. Below we shall see that this inhomogeneity is essential for lifting SB [34]. We consider $\hat{V}_T$ and $\hat{V}_{sf}$ as perturbations. Thus, the unperturbed Hamiltonian for the isolated DQD is the following:

$$\hat{H}_0 = \hat{H}_{DQD} + \hat{V}_{LR} + \hat{V}_z^{MF}. \qquad (3.7)$$

SB occurs when the source-drain voltage is tuned so that the number of electrons in the DQD varies between one and two. The right quantum dot is always occupied with one electron while another electron can tunnel from the source to the drain through the DQD. The transport scheme is the following:

$$(0,\sigma) \longrightarrow (\sigma',\sigma) \longrightarrow \begin{cases} (0,\uparrow\downarrow) \longrightarrow (0,\sigma'') & \text{if} \quad \sigma \neq \sigma' \\ (\sigma,\sigma) \quad \text{(SB)} & \text{if} \quad \sigma = \sigma' \end{cases} , \qquad (3.8)$$

where in (n,m), n (m) accounts for the population of the left (right) dot level, and $\sigma, \sigma', \sigma'' = \uparrow, \downarrow$. Interdot tunnelling ($\hat{V}_{LR}$) is allowed only between states with the same total spin. Since the state $(0,\uparrow\downarrow)$ has total spin zero, while the states with $\sigma = \sigma'$ have total spin one, the transitions $(\sigma,\sigma) \to (0,\uparrow\downarrow)$ are forbidden. The Hilbert space that we have considered, consists of the *atomic basis* $\{|0,\uparrow\rangle, |0,\downarrow\rangle, |\uparrow,\downarrow\rangle, |\downarrow,\uparrow\rangle, |\uparrow,\uparrow\rangle, |\downarrow,\downarrow\rangle, |0,\uparrow\downarrow\rangle\}$. We investigate the coherent *resonant transport* regime. In this regime, the energies of the DQD two electrons states $|\sigma,\sigma'\rangle$ and $|0,\uparrow\downarrow\rangle$

are degenerate in the absence of a magnetic field, i.e., the so called zero detuning regime. In this case $\hat{H}_0$ (see Eq. (3.7)) is exactly diagonalizable. Its eigenenergies and eigenstates are the following:

$$\begin{aligned} E_{T_x} &= \epsilon_L + \epsilon_R + U_{LR} \\ E_{S_\pm} &= \epsilon_L + \epsilon_R + U_{LR} \pm \sqrt{2}\mathcal{N} t_{LR} \\ E_{T_\pm} &= \epsilon_L + \epsilon_R + U_{LR} \pm \left(g\mu_B B_{\text{ext}} + \frac{A_+}{2} P \right) \end{aligned} \tag{3.9}$$

and:

$$\begin{aligned} |T_+\rangle &= |\uparrow,\uparrow\rangle \\ |T_-\rangle &= |\downarrow,\downarrow\rangle \\ |T_x\rangle &= \frac{1}{\mathcal{N}} \left(|T_0\rangle - x|S_{02}\rangle \right) \\ |S_\pm\rangle &= \frac{1}{\sqrt{2}} \left(|S_{11}\rangle \pm \frac{1}{\mathcal{N}} \left(|S_{02}\rangle + x|T_0\rangle \right) \right) \end{aligned} \tag{3.10}$$

where:

$$\begin{aligned} |T_0\rangle &= \frac{1}{\sqrt{2}} \left(|\uparrow,\downarrow\rangle + |\downarrow,\uparrow\rangle \right) \\ |S_{11}\rangle &= \frac{1}{\sqrt{2}} \left(|\uparrow,\downarrow\rangle - |\downarrow,\uparrow\rangle \right) \\ |S_{02}\rangle &= |0,\uparrow\downarrow\rangle \end{aligned} \tag{3.11}$$

being:

$$\begin{aligned} \mathcal{N} &= \sqrt{1+x^2} \\ x &= \frac{1}{\sqrt{2}} \frac{A_- P}{2\, t_{LR}} \\ A_\pm &= \frac{1}{2} \left(A_L \pm A_R \right). \end{aligned} \tag{3.12}$$

Thus, the two electron *molecular basis* is $\{|\pm\rangle, |S_\pm\rangle, |T_x\rangle, |T_\pm\rangle\}$, where $|+(-)\rangle = |0,\uparrow(\downarrow)\rangle$ are the single electron states. Eq. (3.10) shows that $\hat{V}_{LR}$ mixes S_{11} and S_{02} singlets, and $\hat{V}_z^{MF}$ mixes T_0 triplet with S_{11} and S_{02} singlets when $A_L \neq A_R$. The singlet-triplet (ST) mixing is given by the weight $x/\mathcal{N}$. This quantity is the ratio between the Zeeman splitting difference within each dot ($A_- P/2$), and the *exchange energy* defined as $|E_{S_\pm} - E_{T_x}| = \sqrt{2}\mathcal{N}\, t_{LR}$. Therefore, the ST mixing depends on the competition between these two energy scales. A large (small) difference between the HF coupling intensities, and small (large) interdot tunnelling strength increases (decreases) the ST mixing (see Eqs. (3.10) and (3.12)). Furthermore, x is zero when either the HF couplings have the same value for both dots ($A_L = A_R$) or the nuclei

spins are completely depolarized ($P = 0$). In both cases the usual singlet-triplet basis is recovered. Due to the mixing with T_0 triplet state, $S_\pm$ are not pure singlet states anymore, however, for simplicity we shall continue calling them *singlet* states. Finally, notice that now the eigenenergies of singlet states also depend on the nuclear spin polarization through $\mathcal{N}$ (see Eqs. (3.9) and (3.12)).

The transport scheme in the molecular basis is the following:

$$(0,\sigma) \longrightarrow \begin{cases} S_\pm & \longrightarrow & (0,\sigma') \\ T_x & \longrightarrow & \begin{cases} (0,\sigma') & \text{if} \quad x \neq 0 \\ T_0\,(\text{SB}) & \text{if} \quad x = 0 \end{cases} \\ T_\pm & (\text{SB}) & \end{cases} \tag{3.13}$$

This transport scheme shows that for the coherent interdot tunnelling regime, when having different Overhauser fields in the dots, a current channel ($(0,\sigma) \rightarrow T_x \rightarrow (0,\sigma')$) is opened. Therefore, there are two possible situations: i) $x = 0$. In this case the incoming electron will fall either in a singlet state ($S_\pm$) or in a triplet state (T_0 or $T_\pm$). Thus, there are *two* transport channels and *three* SB states; ii) $x \neq 0$. The incoming electron will fall either in a singlet state ($S_\pm$), the T_x state or in the $T_\pm$ triplets. Therefore, now there are *three* transport channels and *two* SB states. However, once the electrons drop in a SB state, the current drops to zero.

3.3 Rate equations

The Hamiltonian in Eq. (5.1) can be written now as follows:

$$\hat{H} = \hat{H}_0 + \hat{V}_T + \hat{V}_{sf} + \hat{H}_{leads}, \tag{3.14}$$

where the eigenstates of $\hat{H}_0$ (see Eq. (3.10)) are the unperturbed states. $\hat{V}_T$ induces transitions between the leads and the DQD, namely, between one-electron and two-electron states. $\hat{V}_{sf}$ is responsible for the spin flip-flop transitions between the DQD electron spins and the surrounding nuclei spins. The time evolution of the DQD molecular states are obtained with the following rate equations:

$$\begin{aligned}
\dot{\rho}_{T_\pm} &= W_{T_\pm,S_+}\rho_{S_+} + W_{T_\pm,S_-}\rho_{S_-} + W_{T_\pm,T_x}\rho_{T_x} + \Gamma_{T_\pm,\pm}\rho_\pm \\
&- (W_{S_+,T_\pm} + W_{S_-,T_\pm} + W_{T_x,T_\pm})\rho_{T_\pm} \\
\dot{\rho}_{T_x} &= W_{T_x,T_+}\rho_{T_+} + W_{T_x,T_-}\rho_{T_-} + \Gamma_{T_x,+}\rho_+ + \Gamma_{T_x,-}\rho_- \\
&- (W_{T_+,T_x} + W_{T_-,T_x} + \Gamma_{+,T_x} + \Gamma_{-,T_x})\rho_{T_x} \\
\dot{\rho}_{S_\pm} &= W_{S_\pm,T_+}\rho_{T_+} + W_{S_\pm,T_-}\rho_{T_-} + \Gamma_{S_\pm,+}\rho_+ + \Gamma_{S_\pm,-}\rho_- \\
&- (W_{T_+,S_\pm} + W_{T_-,S_\pm} + \Gamma_{+,S_\pm} + \Gamma_{-,S_\pm})\rho_{S_\pm} \\
\dot{\rho}_\pm &= \Gamma_{\pm,S_+}\rho_{S_+} + \Gamma_{\pm,S_-}\rho_{S_-} + \Gamma_{\pm,T_x}\rho_{T_x} - (\Gamma_{S_+,\pm} + \Gamma_{S_-,\pm} + \Gamma_{T_x,\pm} + \Gamma_{T_\pm,\pm})\rho_\pm
\end{aligned} \tag{3.15}$$

where ρ_i is the occupation of the i-th state. $\Gamma_{f,i}$ ($W_{f,i}$) are the tunnelling (spin-flip) rates between an initial DQD state $|i\rangle$ and a final DQD molecular state $|f\rangle$. Both tunnelling and spin-flip rates are computed in Section 3.4.

The spin electron-nuclei flip-flop processes induce a non-negligible nuclear spin polarization, which will be positive or negative depending on the specific spin-flip processes. In the following scheme we show the spin-flip processes which contribute to each nuclear spin polarization direction:

$$\begin{aligned} T_+ \rightarrow \{S_+, S_-, T_x\} &\Rightarrow \dot{P} > 0 \\ T_- \rightarrow \{S_+, S_-, T_x\} &\Rightarrow \dot{P} < 0 \\ \{S_+, S_-, T_x\} \rightarrow T_+ &\Rightarrow \dot{P} < 0 \\ \{S_+, S_-, T_x\} \rightarrow T_- &\Rightarrow \dot{P} > 0. \end{aligned} \tag{3.16}$$

E.g., the process $T_+ \rightarrow \{S_+, S_-, T_x\}$ flips down an electron spin and up a nuclear spin, thus, polarizes positively the nuclei spins. Furthermore, the nuclear spin polarization becomes dynamical due to the electrons tunnelling through the DQD. Therefore, we describe the time evolution for the induced nuclear spin polarization using the following rate equation:

$$\begin{aligned} \dot{P} &= \left(W_{T_-,S_+} - W_{T_+,S_+}\right)\rho_{S_+} + \left(W_{T_-,S_-} - W_{T_+,S_-}\right)\rho_{S_-} \\ &+ \left(W_{T_-,T_x} - W_{T_+,T_x}\right)\rho_{T_x} + (W_{S_+,T_+} + W_{S_-,T_+} + W_{T_x,T_+})\rho_{T_+} \\ &- (W_{S_+,T_-} + W_{S_-,T_-} + W_{T_x,T_-})\rho_{T_-} - W_{\mathrm{rel}}\, P \end{aligned} \tag{3.17}$$

where W_{rel} is a phenomenological rate that accounts for the nuclear dipole-dipole spin interaction which is responsible for nuclear spin depolarization. In this equation we have assumed that in absence of spin-flip processes ($W_{f,i}$ all zero), the nuclei spins completely depolarize, namely, that temperature is much larger than the nuclei spin level splittings. As will be shown in Section 3.4, both the tunnelling and the spin-flip rates depend on the nuclear spin polarization. Therefore, Eqs. (3.15) and (3.17) form a set of eight non-linear equations which we must be solved numerically (see chapter 4).

3.3.1 Reduced model

In order to get physical insight on the results which will be discussed in chapter 4, we have developed a simplified model for the rate equations in Eqs. (3.15) and (3.17) through the following assumptions: i) we consider that spin-flip processes are effective when the electrons are in a SB state. Thus, once the electrons are in a singlet state it is much more probable for them to tunnel out of the DQD than to flip its spin to a $T_\pm$ triplet state. Therefore, we neglect the singlet to triplet spin-flip transitions ($W_{T_\pm,S_+}$ and $W_{T_\pm,S_-}$). ii) The singlet states and the one electron states empty much faster than the $T_\pm$ triplets (SB) and the T_x state. Thus, in the time scale on which spin-flip transitions are relevant we assume that the occupation of the one electron state and of the singlet states have reached their stationary value, namely, $\dot{\rho}_\pm \approx \dot{\rho}_{S_\pm} \approx 0$. iii) The nuclei relaxation time due to the spin dipole-dipole interaction is long enough to be neglected ($W_{\mathrm{rel}} \rightarrow 0$). Under these conditions, the rate equation for the nuclei spin polarization Eq. (3.17) is related to the rate equations for

the triplet states Eq. (3.15) through the relation $\dot{\rho}_{T_-} - \dot{\rho}_{T_+} = \dot{P}$, thus, $\rho_{T_-} - \rho_{T_+} = P$ (where we consider $\rho_{T_-}(0) - \rho_{T_+}(0) - P(0) = 0$ and $\rho_{\pm}(0) = \rho_{S_\pm}(0) = 0$ as initial condition). Taking these considerations into account the rate equations in Eq. (3.15) become:

$$\begin{aligned}
\dot{\rho}_T &= \left(2\omega_+^{tt} + \beta\right)\rho_{T_x} - (\omega_+^{st} + \omega_+^{tt})\rho_T + (\omega_-^{st} + \omega_-^{tt})P && \text{(3.18a)}\\
\dot{\rho}_{T_x} &= (\omega_+^{st} + \omega_+^{tt})\rho_T - (\omega_-^{st} + \omega_-^{tt})_- P - (2\omega_+^{tt} + \beta)\rho_{T_x} && \text{(3.18b)}\\
\dot{P} &= 2\omega_-^{tt}\rho_{T_x} + (\omega_-^{st} + \omega_-^{tt})\rho_T - (\omega_+^{st} + \omega_+^{tt})P && \text{(3.18c)}
\end{aligned}$$

where $\rho_T = \rho_{T_+} + \rho_{T_-}$ and,

$$\begin{aligned}
\omega_\pm^{tt} &= \frac{1}{2}\left(W_{T_-,T_x} \pm W_{T_+,T_x}\right)\\
\omega_\pm^{st} &= \frac{1}{2}\frac{(W_{S_+,T_+} + W_{S_-,T_+}) \pm (W_{S_+,T_-} + W_{S_-,T_-})}{1 + \Gamma/\Gamma_{+,S_+}}\\
\beta &= \frac{2\Gamma_{+,T_x}}{1 + \Gamma_{+,S_+}/\Gamma}. && \text{(3.19)}
\end{aligned}$$

We have considered the same value of the tunnelling coupling for both contact barriers, $\Gamma_L = \Gamma_R = \Gamma$ (see Section 3.4.2). Finally, by summing Eqs. (3.18a) and (3.18b) we find that $\rho_T + \rho_{T_x} = 1$, where we consider as initial condition: $\rho_T(0) + \rho_{T_x}(0) = 1$, thus, the rate equations become:

$$\begin{aligned}
\dot{\rho}_{T_x} &= (\omega_+^{tt} + \omega_+^{st}) - (3\omega_+^{tt} + \beta + \omega_+^{st})\rho_{T_x} - (\omega_-^{tt} + \omega_-^{st})P\\
\dot{P} &= (\omega_-^{tt} + \omega_-^{st}) + (\omega_-^{tt} - \omega_-^{st})\rho_{T_x} - (\omega_+^{tt} + \omega_+^{st})P && \text{(3.20)}
\end{aligned}$$

The rates $\omega_\pm^{st}$ account for the SB lifting due to ST spin relaxation: $T_\pm \xrightarrow{\omega_\pm^{st}} \{S_+, S_-\}$. $\omega_\pm^{tt}$ (β) account for the spin-flip (tunnelling) rates from T_x to $T_\pm$ (T_x to $|\pm\rangle$). In Section 3.4.2, we will see that the rate $\Gamma_{+,S_+} \simeq \Gamma/2$, hence, it can be regarded as constant. In chapter 4, it will be shown that the current through the DQD depends on ratio between ω_+^{tt} and β. The following scheme offers a qualitative description of this dependence for the case of $A_- \neq 0$:

$$T_x \longrightarrow \begin{cases} \xrightarrow{\omega_+^{tt} \ll \beta} & (0,\sigma) \longrightarrow \text{High Current Regime} \\ \xrightarrow{\omega_+^{tt} \gg \beta} & T_\pm \longrightarrow \text{Low Current Regime.} \end{cases} \qquad \text{(3.21)}$$

When $\omega_+^{tt} \gg \beta$ electrons in T_x state have a larger probability to spin-flip to the $T_\pm$ triplets than to tunnel out of the DQD, and only the leakage current coming from the $T_\pm \to \{S_+, S_-\}$ transitions provide a leakage current, which we define as the *low current regime*. On the contrary, when $\omega_+^{tt} \ll \beta$ electrons in T_x state have a larger probability to tunnel out of the DQD than to spin-flip to the blocked $T_\pm$ triplets, and the current is enhanced. We define this case as the *high current regime*. In chapter 4, we will see that the competition between spin-flip and tunnelling transition rates

determine the behaviour of the leakage current. Moreover, we will see that the transition between the low current regime and the high current regime is obtained by varying either the interdot tunnelling strength or the HF coupling intensity.

3.4 Transition rates

3.4.1 Spin-flip rates

The transition rates between $\hat{H}_0$ eigenstates (see Eq. (3.10)) due to spin-flip processes are calculated in perturbation theory by means of Fermi's Golden Rule [14, 51, 53]. The left (right) dot electron spin z-projection is given by $m_{L(R)} = \pm 1/2$, hence, the total spin projection in the z-direction for a DQD two electron state is $M = m_L + m_R$ ($M = -1, 0, 1$ for triplets, and $M = 0$ for singlets). The spin-flip interaction term $\hat{V}_{sf}$ (see Eq. (3.4)) increases an electron spin by one while decreasing a nuclei spin by one also (and vice versa), thus, $M: -1 \overset{\hat{V}_{sf}}{\longleftrightarrow} 0 \overset{\hat{V}_{sf}}{\longleftrightarrow} 1$. We consider the initial state $|i_N\rangle|\alpha_M\rangle$ which consists of the initial nuclei states $|i_N\rangle$ and the DQD electron states $|\alpha_M\rangle$. $|i_N\rangle$ is given by $|i_N\rangle = |m_1, m_2, \ldots, m_j, \cdots, m_N\rangle$, where $m_j = \pm 1/2$ is the spin of the j-th nuclei, and $|\alpha_M\rangle \in \{|S_\pm\rangle, |T_x\rangle, |T_\pm\rangle\}$. The final state $|f_N\rangle|\beta_{M'}\rangle$ is connected to the initial one by having the j-th nuclear spin flipped and a different electronic state $|\beta_{M'}\rangle$ with $|M - M'| = 1$. Therefore the spin-flip rate for the transition that flips up an electron spin and down a nuclei spin is:

$$\begin{aligned} W_{\beta_{M+1}\alpha_M} &= 2\pi \sum_{j=1}^{N} \sum_{i_N} |\langle \beta_{M+1}|\langle f_N|\hat{V}_{sf}|i_N\rangle|\alpha_M\rangle|^2 \, \mathcal{W}_{i_N} \, \delta\left(E_{\beta_{M+1}} - \delta_j - E_{\alpha_M}\right) \\ &= 2\pi \frac{1}{N^2} \frac{1}{2^2} \left| \sum_{l=L,R} A_l \langle \beta_{M+1}|\hat{S}_l^+|\alpha_M\rangle \right|^2 \sum_{j=1}^{N} \sum_{i_N} \langle i_N|\hat{I}_j^+ \hat{I}_j^-|i_N\rangle \, \mathcal{W}_{i_N} \\ &\times \delta\left(E_{\beta_{M+1}} - \delta_j - E_{\alpha_M}\right). \end{aligned} \tag{3.22}$$

where $|f_N\rangle = \hat{I}_j^-|i_N\rangle$ and we have taken $\hbar = 1$. The sum over initial states runs over all configurations of the internal degrees of freedom, i_N, that give the state $|i_N\rangle$. Each state is weighted by the probability of having that configuration, which is given by the distribution function $\mathcal{W}_{i_N}$. E_{α_M} ($E_{\beta_{M+1}}$) is the energy of the initial (final) electronic state $|\alpha_M\rangle$ ($|\beta_{M+1}\rangle$), and δ_j is the energy splitting between the up-down levels of the j-th nuclei spin. We assume independent nuclei spins, hence, $\mathcal{W}_{i_N} = \mathcal{W}_{m_1} \times \mathcal{W}_{m_2} \times \ldots \times \mathcal{W}_{m_N}$, where $\mathcal{W}_{m_j}$ is the probability that nuclear spin j has the value m_j. Thus, the sum over initial nuclear states becomes:

$$\sum_{i_N} \langle i_N|\hat{I}_j^+ \hat{I}_j^-|i_N\rangle \, \mathcal{W}_{i_N} = \sum_{m_j} \langle m_j|\hat{I}_j^+ \hat{I}_j^-|m_j\rangle \, \mathcal{W}_{m_j} \tag{3.23}$$

where we have used the normalization condition $\mathcal{W}_{m_k=1/2} + \mathcal{W}_{m_k=-1/2} = 1$ to eliminate all other sums over m_k except m_j. The probability of having nuclear spin j in

a certain state is related to the overall nuclear spin polarization as:

$$\begin{aligned} \mathcal{W}_{m_j=1/2} &= \frac{\langle N_\uparrow \rangle}{N} = \frac{1+P}{2} \\ \mathcal{W}_{m_j=-1/2} &= \frac{\langle N_\downarrow \rangle}{N} = \frac{1-P}{2}. \end{aligned} \tag{3.24}$$

In general, the g-factor is much smaller for nuclei spins than for electrons [62]. Therefore, under experimental conditions [33,35–37,43], the nuclear splitting is usually negligible compared to temperature and the energy difference between electronic levels, hence, $\delta_j \ \forall j = 1 \dots N$ can be safely neglected. Thus, the spin-flip rate becomes:

$$W_{\beta_{M+1}\alpha_M} = \frac{\pi}{2N} \left| \sum_{l=L,R} A_l \langle \beta_{M+1} | \hat{S}_l^+ | \alpha_M \rangle \right|^2 \frac{1+P}{2} \, \delta\left(E_{\beta_{M+1}} - E_{\alpha_M}\right). \tag{3.25}$$

Repeating the same procedure we have that the spin-flip rate for the transition that flips down an electron spin and up a nuclei spin is the following:

$$W_{\beta_{M-1}\alpha_M} = \frac{\pi}{2N} \left| \sum_{l=L,R} A_l \langle \beta_{M-1} | \hat{S}_l^- | \alpha_M \rangle \right|^2 \frac{1-P}{2} \, \delta\left(E_{\beta_{M-1}} - E_{\alpha_M}\right). \tag{3.26}$$

Notice that these spin flip-rates depend on how much the nuclei are polarized. When the nuclei spins are fully polarized in the positive (negative) direction $W_{\beta_{M-1}\alpha_M}$ ($W_{\beta_{M+1}\alpha_M}$) vanishes.

We see that the derived spin-flip rate requires energy conservation, so strictly speaking leads to zero spin-flip for $E_{\alpha_M} \neq E_{\beta_{M\pm1}}$. However, in reality it is possible to exchange energy [63] with the environment e.g. as phonons. We model this by replacing the Dirac delta by the following expression:

$$\delta\left(E_{\beta_{M\pm1}} - E_{\alpha_M}\right) \to \frac{1}{\pi} \frac{\gamma}{\left(E_{\beta_{M\pm1}} - E_{\alpha_M}\right)^2 + \gamma^2} \times \mathcal{C}_{\beta_{M\pm1}\alpha_M} \tag{3.27}$$

where:

$$\mathcal{C}_{\beta_{M\pm1}\alpha_M} = \begin{cases} 1 & \text{if} \quad E_{\beta_{M\pm1}} > E_{\alpha_M} \quad \text{(Emission)} \\ \exp\left(\frac{E_{\beta_{M\pm1}} - E_{\alpha_M}}{k_B T}\right) & \text{if} \quad E_{\beta_{M\pm1}} < E_{\alpha_M} \quad \text{(Absorption)} \end{cases} \tag{3.28}$$

where T is the temperature and k_B the Boltzmann constant. The Lorentzian is maximal for the elastic case and falls off with increasing energy exchange on the characteristic scale γ. This parameter is assumed to be of the order of the typical phonon energy, $\gamma \sim \mu$eV [63]. The function $\mathcal{C}_{\beta_{M\pm1}\alpha_M}$ accounts for the low temperature energy emission/absorption asymmetry [63, 64], i.e., it is much easier to emit than absorb energy from e.g. a phonon bath. Formally, one can include the

electron-phonon coupling as a perturbation together with $\hat{V}_{sf}$ and thereafter use a T-matrix approach to find the phonon-mediated HF spin-flip rate [65–67]. However, here we do not pursue an exact modeling of the way the energy is exchanged with the environment, but simply include the fact that the spin-flip rate decreases as the energy involved in the flip-flop processes increases [51, 53]. Therefore, the spin-flip rates we obtain are the following:

$$W_{\beta_{M\pm1}\alpha_M} = \frac{1}{2N}\left|\sum_{l=L,R} A_l \langle \beta_{M\pm1}|\hat{S}_l^{\pm}|\alpha_M\rangle\right|^2 \frac{1\pm P}{2}\,\frac{\gamma}{\left(E_{\beta_{M\pm1}}-E_{\alpha_M}\right)^2+\gamma^2}\,\mathcal{C}_{\beta_{M\pm1}\alpha_M}. \tag{3.29}$$

In chapter 4, we will show that the amount of induced nuclear spin polarization depends on the competition between emission and absorption processes. The energies that appear in the function $\mathcal{C}_{\beta_{M\pm1}\alpha_M}$ (see Eq. (3.28)) are the eigenenergies shown in Eq. (3.9). Thus, the energy differences in $\mathcal{C}_{\beta_{M\pm1}\alpha_M}$ depend on the interdot tunnel strength, the HF coupling and the external magnetic field. Therefore, for a given temperature the emission/absorption asymmetry can be controlled through these parameters. Finally, the only matrix elements between the DQD states which are different from zero in Eq. (3.29) are:

$$\langle T_x|\left(A_L\hat{S}_L^{\pm}+A_R\hat{S}_R^{\pm}\right)|T_{\mp}\rangle = \frac{\sqrt{2}\,A_+}{\mathcal{N}} \tag{3.30a}$$

$$\langle S_{\pm}|\left(A_L\hat{S}_L^{-}+A_R\hat{S}_R^{-}\right)|T_{+}\rangle = -\left(A_- \mp \frac{xA_+}{\mathcal{N}}\right) \tag{3.30b}$$

$$\langle S_{\pm}|\left(A_L\hat{S}_L^{+}+A_R\hat{S}_R^{+}\right)|T_{-}\rangle = A_- \pm \frac{xA_+}{\mathcal{N}} \tag{3.30c}$$

From these expressions we distinguish between two different HF mediated spin relaxation processes: i) the triplet-triplet relaxation Eq. (3.30a), and ii) the singlet-triplet relaxation (Eqs. (3.30b) and (3.30c)). Notice that if the HF coupling intensities have the same value for each dot ($A_- = 0$, and then $x = 0$) only the triplet-triplet spin relaxation survives ($T_{\mp} \to T_x = T_0$) while ST relaxation probabilities become zero. Thus, SB lifting involves having $A_- \neq 0$, as discussed in section 3.2 (see Eq. (3.13)). Finally, the matrix elements also depend on the interdot tunnel through the ST mixing parameter x (see Eq. (3.12)).

3.4.2 Tunnelling rates

The tunnelling rates between the leads and the DQD are calculated using Fermi's Golden Rule [14,64]. Given an initial DQD state with n electrons $|\alpha_n\rangle$ the tunnelling rate for an incoming electron to the final DQD state $|\beta_{n+1}\rangle$ with $n+1$ electrons is:

$$\Gamma^l_{\beta_{n+1},\alpha_n} = \Gamma_l f(\mu_D-\mu_l)\sum_{\sigma}|\langle\beta_{n+1}|\hat{d}^{\dagger}_{l\sigma}|\alpha_n\rangle|^2. \tag{3.31}$$

And the tunnelling rate for an outcoming electron to the final DQD state $|\beta_{n-1}\rangle$ with $n-1$ electrons is:

$$\Gamma^{l}_{\beta_{n-1},\alpha_n} = \Gamma_l \left(1 - f(\mu_D - \mu_l)\right) \sum_{\sigma} |\langle \beta_{n-1}|\hat{d}_{l\sigma}|\alpha_n\rangle|^2 \tag{3.32}$$

where $l = L, R$. $\Gamma_l = 2\pi\,|\gamma_{lk}|^2\, D_l$, where it is assumed that the density of states in both leads D_l and the the tunnelling couplings γ_{lk} (see Eq. (3.2)) are energy-independent. $f(\mu_D - \mu_{L(R)})$ is the Fermi distribution function for the left (right) lead, $\mu_{L(R)}$ is the chemical potential of the left (right) lead and μ_D is the DQD chemical potential. The DQD states that appear in the matrix elements in the tunnelling rates are the eigenstates of $\hat{H}_0$ (see Eq. (3.10)). The chemical potentials (μ_l) are tuned such that the system is in the SB regime, and we define $\Gamma_{\beta_{n\pm1},\alpha_n} = \sum_{l=L,R} \Gamma^{l}_{\beta_{n\pm1},\alpha_n}$. Therefore, the tunnelling rates different from zero are:

$$\begin{aligned}
\Gamma_{T_\pm,\pm} &= \Gamma_L \\
\Gamma_{S_+,\pm} &= \frac{\Gamma_L}{4}\left(1 + \frac{x^2}{\mathcal{N}^2} \mp \frac{2x}{\mathcal{N}}\right) \\
\Gamma_{S_-,\pm} &= \frac{\Gamma_L}{4}\left(1 + \frac{x^2}{\mathcal{N}^2} \pm \frac{2x}{\mathcal{N}}\right) \\
\Gamma_{T_x,\pm} &= \frac{\Gamma_L}{2}\frac{1}{\mathcal{N}^2}.
\end{aligned} \tag{3.33}$$

for electrons tunnelling from the leads into the DQD, and:

$$\begin{aligned}
\Gamma_{\pm,S_+} &= \Gamma_{\pm,S_-} = \frac{\Gamma_R}{2}\frac{1}{\mathcal{N}^2} \\
\Gamma_{\pm,T_x} &= \Gamma_R \frac{x^2}{\mathcal{N}^2}
\end{aligned} \tag{3.34}$$

for electrons tunnelling out of the DQD to the leads. As pointed out in section 3.3, the tunnelling rates also depend on the nuclear spin polarization. Additionally, $\Gamma_{\pm,T_x}$ becomes zero if $x = 0$ (see Eq. (3.12)), i.e., when the HF couplings within each dot are the same ($A_- = 0$), or the nuclei spins are completely depolarized ($P = 0$).

Finally, the tunnelling current through the DQD is given by [14]:

$$I_l = (-e) \sum_{n} \sum_{\alpha_n,\beta_{n\pm1}} \left(\Gamma^{l}_{\beta_{n+1},\alpha_n} - \Gamma^{l}_{\beta_{n-1},\alpha_n}\right) \rho_{\alpha_n} \tag{3.35}$$

where $l = L, R$.

Chapter 4

Hyperfine interaction in electron transport in double quantum dots: Results

In this chapter, we present the results obtained by solving numerically the full system of rate equations derived in chapter 3 (Eqs. (3.15) *and* (3.17)*).*

4.1 Introduction

The system has three main relaxation time scales: i) the tunnelling through the contact barriers, ii) the electron-nuclei spin-flip, and iii) the nuclear spin relaxation ($\propto W_{\rm rel}$). The nuclear relaxation time is the largest one ($\sim$ minutes [34, 37, 68]). We are mainly interested in investigating the system on a time scale for which the tunnelling and the spin-flip are the relevant relaxation times, whereas the nuclear spin relaxation time is much larger.

We will discuss the behaviour of the electronic current and the induced nuclei spin polarization versus the external magnetic field for different HF couplings and interdot tunnelling strengths. The HF interaction constant is not well known for all materials, thus, we have considered values for the HF coupling intensity in the range $A_L = 70 - 90\,\mu$eV [35, 37, 58]. The difference between the HF couplings in each dot is held constant for all cases ($A_R = 0.8A_L$). The plots described below have been obtained by solving numerically the rate equations derived in chapter 3, Eqs. (3.15) and (3.17), sweeping the external magnetic field from negative to positive values. We have performed the calculations for three cases: i) In order to observe only the effect of the dynamical nuclear spin polarization, we consider that the nuclei spins are initially fully depolarized for each value of the external magnetic field. Thus, the sweeping rate is much slower than the nuclear spin relaxation rate $W_{\rm rel}$ (see

Eq. (3.17)). Nevertheless, for each value of the external field the rate equations are solved in a time scale much smaller than the nuclear spin relaxation rate in order to capture only the tunnelling and spin-flip events. ii) Initially the nuclei spins are completely depolarized, however, while the magnetic field is swept, nuclear spin polarization is built up. Thus, the sweeping rate is much faster than the nuclear spin relaxation rate, and a *feedback* processes between nuclear spins and electronic current occurs. iii) we proceed as in ii) sweeping the external field forwards and backwards. In this case we observe hysteresis, as has been widely observed experimentally for different DQD devices. [34, 35, 37, 41]

As stated in chapter 3, we consider the zero detuning case (i.e., $|\sigma, \sigma'\rangle$ and $|S_{02}\rangle$ are degenerate). In previous works [55, 56], finite detuning was considered, therefore only transitions close to one ST level crossing are important. Now, different energy levels approaches participate and we take into account all HF mediated electron spin relaxation processes, at a fixed external magnetic field. Fig. 4.1 shows the energy levels for the different regimes considered. $B_{S_\pm,T_\mp}$ ($B_{S_\pm,T_\pm}$) corresponds to the value of the external field for which the $S_\pm T_\mp$ ($S_\pm T_\pm$) crossings occur, and B_{TT} the value for which the $T_\pm T_x$ crossing occurs. Notice that the different $S_\pm T_\mp$ crossings occur for the same value of the external field (see Eq. (3.9)), and the same happens for the different $S_\pm T_\pm$ crossings. The energy emission spin-flip rates which contribute for each range of the external field in Fig. 4.1 are given in the following scheme:

$$B_{\text{ext}} < B_{S_\pm,T_\mp} \quad \Rightarrow \quad W_{S_\pm,T_-}, W_{T_x,T_-}, W_{T_+,T_x} \quad \Rightarrow \quad P < 0 \tag{4.1a}$$

$$B_{S_\pm,T_\mp} < B_{\text{ext}} < B_{TT} \quad \Rightarrow \quad \begin{cases} W_{S_-,T_-}, W_{T_x,T_-}, W_{T_+,T_x} & \Rightarrow \quad P < 0 \\ W_{S_-,T_+} & \Rightarrow \quad P > 0 \end{cases} \tag{4.1b}$$

$$B_{TT} < B_{\text{ext}} < B_{S_\pm,T_\pm} \quad \Rightarrow \quad \begin{cases} W_{S_-,T_-} & \Rightarrow \quad P < 0 \\ W_{S_-,T_+}, W_{T_x,T_+}, W_{T_-,T_x} & \Rightarrow \quad P > 0 \end{cases} \tag{4.1c}$$

$$B_{S_\pm,T_\pm} < B_{\text{ext}} \quad \Rightarrow \quad W_{S_\pm,T_+}, W_{T_x,T_+}, W_{T_-,T_x} \quad \Rightarrow \quad P > 0 \tag{4.1d}$$

where the sign of the nuclear spin polarization in each case is described in Eq. (3.16). Only emission spin-flip rates are shown because at low temperatures they dominate over the absorption rates, hence, they will determine the sign of nuclear spin polarization. Thus, depending on the intensity of the external magnetic field there will be different spin-flip processes dominating.

4.2 Dependence on the hyperfine interaction intensity

4.2.1 Small magnetic fields

In this section we consider small external magnetic field intensities. We will focus on the $B_{S_\pm,T_\mp} < B_{\text{ext}} < B_{S_\pm,T_\pm}$ range of magnetic fields. The main spin-flip transition rates corresponding to this range of magnetic fields are shown in Eqs. (4.1b) and (4.1c), and the energy levels scheme is plotted in Figs. 4.1b and 4.1c (see also

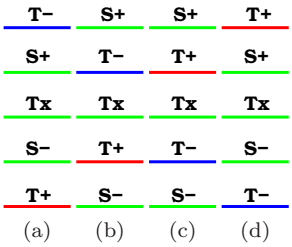

Figure 4.1: Schematic energy level arrangement for the DQD eigenstates in the different external magnetic field regions that are investigated. a) $B_{\text{ext}} < B_{S_\pm,T_\mp}$, b) $B_{S_\pm,T_\mp} < B_{\text{ext}} < B_{TT}$, c) $B_{TT} < B_{\text{ext}} < B_{S_\pm,T_\pm}$ and d) $B_{S_\pm,T_\pm} < B_{\text{ext}}$.

.

Fig. 4.3). In this case, the transitions around the $T_\pm T_x$ crossing give the main contribution to the current, although other possible opposite spin level transitions participate (see Eqs. (4.1b) and (4.1c)). The $S_\pm T_\mp$ and $S_\pm T_\pm$ crossings occur for larger magnetic field intensities and will be studied in section 4.2.3. Fig. 4.2 shows the induced nuclear spin polarization and the leakage current through the DQD versus the external magnetic field for different values of the HF coupling (A_L), in this range of the external field.

The induced nuclear spin polarization versus the external field is shown in Figs. 4.2a (without feedback), 4.2b (with feedback) and 4.2c (sweeping forwards and backwards with feedback). Fig. 4.3 shows the energy levels. When $B_{\text{ext}} < B_{TT}$ ($B_{\text{ext}} > B_{TT}$) the net induced nuclear spin polarization is negative (positive): Emission processes are stronger than absorption processes, hence, they mainly determine the sign of the nuclear spin polarization. In Eq. (4.1b) it is shown that when $B_{\text{ext}} < B_{TT}$ ($B_{\text{ext}} > B_{TT}$) the dominating spin-flip rates are W_{S_-,T_-}, W_{T_x,T_-} and W_{T_+,T_x} ($W_{S_\pm,T_+}$, W_{T_x,T_+} and W_{T_-,T_x}), which polarize the nuclei negatively (positively). Nevertheless, in this regime absorption processes have the effect of partially compensating emission processes resulting in a finite but not complete spin polarization of the nuclei. In Figs. 4.2a, 4.2b and 4.2c it is shown that increasing the HF coupling increases the nuclei spin polarization. In this region, since $|E_{S_\pm} - E_{T_x}| \gg |E_{T_\pm} - E_{T_x}|$, the $T_\pm \leftrightarrow T_x$ transitions are the most important (see Figs. 4.1b, 4.1c and 4.3). The absolute energy difference between these levels is given by the total effective Zeeman splitting (see Eq. (3.9)):

$$\Delta_{\text{tot}} = \left(g\mu_B B_{\text{ext}} + \frac{A_+}{2} P \right). \tag{4.2}$$

As the HF coupling intensity increases, so does the energy difference between the initial and the final states. Therefore, absorption processes become weaker with respect to the emission processes as A_L increases (see Eq. (3.28)), allowing the nuclei spins to become more polarized (Fig. 4.2).

Fig. 4.3 shows the energy levels of the DQD versus the external magnetic field. Electron-nuclei spin feedback is taken into account, and the external field is swept forwards and backwards. Fig. 4.3a shows the energy levels for the smallest HF coupling considered ($A_L = 70\,\mu$eV). In this case: i) the induced Overhauser field is always parallel to the external field (see Eq. (3.6)); and ii) the $T_\pm T_x$ crossing occurs at $B_{\rm ext} = B_{TT} = 0\,$T. Fig. 4.3b shows that for the largest value of the HF coupling ($A_L = 90\,\mu$eV) considered here, the effect of including the feedback is to renormalize the electronic energy levels in such a way that the $T_\pm T_x$ crossing occurs at larger absolute magnetic field than in the previous case. When sweeping forwards (backwards) from $B_{\rm ext} < 0$ ($B_{\rm ext} > 0$) through $B_{\rm ext} = 0$, there is a negative (positive) nuclei spin polarization built up (Fig. 4.2c), hence, it is still necessary to increase (decrease) the external field in order to compensate the accumulated Overhauser field and reach the $T_\pm T_x$ crossing. This crossing occurs now for $B_{TT} > 0$ ($B_{TT} < 0$) when sweeping forwards (backwards). Thus, Fig. 4.2b shows a small region for positive values of the external field where the Overhauser field and the external field are antiparallel. Finally, Figs. 4.2c and 4.3b show that, precisely in this region where the external and the induced fields are antiparallel, hysteresis is observed as the external field is swept backwards. Notice that the hysteresis is observed only for the largest value of the HF coupling intensity considered. Moreover, the size of the hysteresis loop increases with the HF coupling intensity (not shown in the figures). Summarizing: i) The amount of polarization induced in the nuclei spins depends on the competition between absorption and emission spin-flip processes; ii) the nuclear spin polarization increases with the HF coupling; and iii) for large values of the HF coupling, the nuclear spin polarization versus the external magnetic field presents a bistable region where hysteresis is observed. In this region the external field and the Overhauser field are antiparallel.

We will now analyze the leakage current behaviour versus the external magnetic field. Figs. 4.2d (without feedback), 4.2e (with feedback) and 4.2f (sweeping forwards and backwards with feedback) shows different behaviours for the current depending on the intensity of the HF coupling. The smallest HF coupling intensity considered ($A_L = 70\,\mu$eV) presents a current dip around the $T_\pm T_x$ crossing (Fig. 4.3), whereas the largest one ($A_L = 90\,\mu$eV) presents a current peak. This behaviour can be understood recalling the current behaviour studied in the scheme given in Eq. (3.21). Briefly, this scheme defined a low and a high current regime, comparing the $T_x \to T_\pm$ spin-flip rates ($W_{T_\pm,Tx}$) with the $T_x \to |\pm\rangle$ tunnelling rates ($\Gamma_{\pm,T_x}$). These rates are shown in Fig. 4.4. Fig. 4.4a ($A_L = 70\,\mu$eV) shows that around the $T_\pm T_x$ crossing $W_{T_\pm,T_x} \gg \Gamma_{\pm,T_x}$ ($\omega_+^{tt} \gg \beta$ in diagram Eq. (3.21)). Therefore, it is more probable for electrons to spin-flip from $T_x \to T_\pm$ than to tunnel from $T_x \to |\pm\rangle$ through the contact barrier, so a current dip is observed (low current regime). By contrast, Fig. 4.4c ($A_L = 90\,\mu$eV) shows that around the $T_\pm T_x$ crossing, $W_{T_\pm,T_x} < \Gamma_{\pm,T_x}$ ($\omega_+^{tt} < \beta$ in diagram Eq. (3.21)). Therefore, it is more probable for electrons to tunnel from $T_x \to |\pm\rangle$ than to spin-flip from $T_x \to T_\pm$, so a current is enhanced and a peak is observed (high current regime). Furthermore, Fig. 4.2a shows that for the smallest intensity considered for the HF coupling ($A_L = 70\,\mu$eV), the nuclear spin

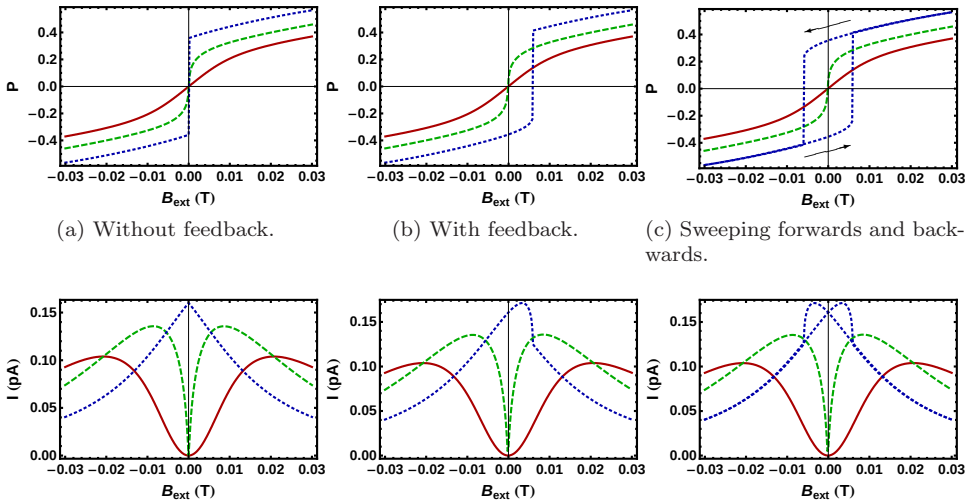

(a) Without feedback. (b) With feedback. (c) Sweeping forwards and backwards.

(d) Without feedback. (e) With feedback. (f) Sweeping forwards and backwards.

Figure 4.2: a), b), c) Induced nuclear spin polarization versus external magnetic field. d), e), f) Leakage current versus external magnetic field. Parameters: $T = 120\,\mathrm{mK}$, $t_{LR} = 50\,\mu\mathrm{eV}$, $\Gamma_L = \Gamma_R = k_B T/3$, $A_R = 0.8 A_L$, $\gamma = 5\,\mu\mathrm{eV}$, $N = 5 \times 10^4$. Initial conditions: $\rho_{1_R}(0) = 1$ and $P(0) = 0$. $A_L = 70\,\mu\mathrm{eV}$ (solid, red online), $A_L = 80\,\mu\mathrm{eV}$ (dashed, green online) and $A_L = 90\,\mu\mathrm{eV}$ (dotted, blue online). Hysteresis is only observed for the largest value of the HF coupling ($A_L = 90\,\mu\mathrm{eV}$). The leakage current shows a dip (peak) for the smallest (largest) value of the HF coupling.

polarization goes to zero around the $T_\pm T_x$ crossing, and so does $\Gamma_{\pm,T_x}$ (see Eq. (3.34) and Fig. 4.4a), thus, a current dip is observed (Fig. 4.2d). However, for the largest intensity considered ($A_L = 90\,\mu\mathrm{eV}$), the nuclear spin polarization is finite around the $T_\pm T_x$ crossing and $\Gamma_{\pm,T_x} > W_{T_\pm,Tx}$ (Fig. 4.4c), thus, a current peak is observed (Fig. 4.2d).

Figs. 4.2d, 4.2e and 4.2f show how the leakage current increases as the HF coupling intensity increases when the external field is close to zero. When increasing the HF coupling, the tunnelling rate $\Gamma_{\pm,T_x}$ (see Eq. (3.34)) also increases (Fig. 4.4) and, therefore, so does the current. For $A_L = 70\,\mu\mathrm{eV}$ and $A_L = 80\,\mu\mathrm{eV}$, a current drops to zero at $B_{\mathrm{ext}} = B_{TT} = 0$, whereas for $A_L = 90\,\mu\mathrm{eV}$ a current peak (Fig. 4.2d) is observed. This peak occurs at $B_{\mathrm{ext}} = B_{TT} \neq 0$ when feedback is considered (Fig. 4.2e). Moreover, Fig. 4.2e shows that the effect of the electron nuclei spin feedback is only appreciable for the largest value of the HF coupling ($A_L = 90\,\mu\mathrm{eV}$). Therefore, only in this case current hysteresis is observed when sweeping backwards the external field (Fig. 4.2f).

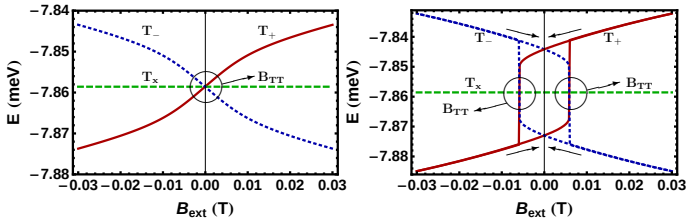

(a) $A_L = 70\,\mu$eV (b) $A_L = 90\,\mu$eV

Figure 4.3: Energy levels versus external magnetic field taking the spin electron-nuclei feedback into account and sweeping forwards and backwards $B_{\rm ext}$, for $A_L = 70\,\mu$eV (a) and $A_L = 90\,\mu$eV (b). T_+ (solid, red online), T_- (dotted, blue online), T_x (dashed, green online). Same parameters and initial conditions than in Fig. 4.2. The magnetic field range considered just includes the $T_\pm T_x$ crossing. Singlet states are far away in energy. As in Fig. 4.2, hysteresis is only observed for the largest value of the HF coupling ($A_L = 90\,\mu$eV).

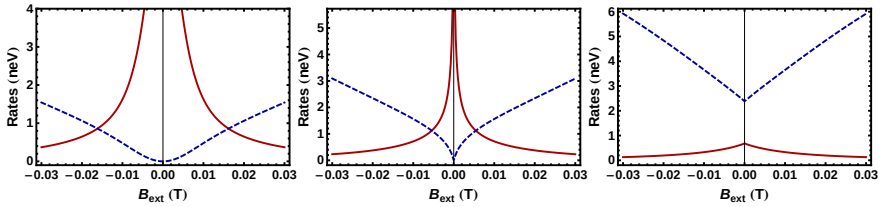

(a) $A_L = 70\,\mu$eV. (b) $A_L = 80\,\mu$eV. (c) $A_L = 90\,\mu$eV.

Figure 4.4: Spin-flip rates (ω_+^{tt}, see Eq. (3.19); solid, red online) and tunnelling rates through contact barriers (β, see Eq. (3.19); dashed, blue online) versus external magnetic field. Same parameters and initial conditions than in Fig. 4.2. In Figs. 4.4a and 4.4b there are two regions: i) $\beta > \omega_+^{tt}$, namely, electron tunnelling from T_x to the right lead is *more* effective than electron spin-flip from T_x to $T_\pm$ triplets (high current regime); and ii) $\beta < \omega_+^{tt}$, namely, electron tunnelling from T_x to the right lead is *less* effective than electron spin-flip from T_x to $T_\pm$ triplets (low current regime). In this case, the current shows a dip around zero external magnetic field (Fig. 4.2). In Fig. 4.4c, $\beta > \omega_+^{tt}$ always. In this case, the current shows a peak (Fig. 4.2).

4.2.2 Simplified model around the triplet-triplet crossing

In the regime described in section 4.2.1, the relations $|E_{T_\pm} - E_{S_+}| \gg \gamma$ and $|E_{T_\pm} - E_{S_-}| \gg \gamma$ are well satisfied, so the rates $\omega_\pm^{st}$ that appear in the reduced rate equations Eq. (3.20) can be safely neglected (see Eqs. (3.19) and (3.29)) and Eq. (3.20) becomes:

$$\begin{aligned} \dot{\rho}_{T_x} &= \omega_+^{tt} - (3\omega_+^{tt} + \beta)\rho_{T_x} - \omega_-^{tt} P \\ \dot{P} &= \omega_-^{tt} + \omega_-^{tt}\rho_{T_x} - \omega_+^{tt} P \end{aligned} \tag{4.3}$$

Considering the stationary limit, we obtain the following equations for the stationary solutions:

$$\rho_{T_x} = \frac{1 - p_t^2}{3 + \frac{\beta}{\omega_+^{tt}} + p_t^2} \tag{4.4a}$$

$$P = \frac{4 + \frac{\beta}{\omega_+^{tt}}}{3 + \frac{\beta}{\omega_+^{tt}} + p_t^2}\, p_t \tag{4.4b}$$

where $p_t = \omega_-^{tt}/\omega_+^{tt}$. The rates $\omega_\pm^{tt}$ and β are complicated functions of P (see Eqs. (3.19), (3.29) and (3.30a)), thus, Eq. (4.4b) cannot be solved analytically. We have obtained numerical solutions for $B_{\text{ext}} = 0$ (Fig. 4.5) case, although Eqs. (4.4a) and (4.4b) hold also for finite external fields. Fig. 4.5 shows that increasing the HF coupling intensity produces a *bifurcation* on the induced nuclei spin polarization. For $A_L \leq 80.43\,\mu$eV, the nuclei spins have *one* stable solution at $P = 0$, namely, the nuclei spins are fully depolarized (solid line). However, for $A_L > 80.43\,\mu$eV, the $P = 0$ solution becomes unstable (dashed line), and *two* stable solutions (solid lines), with the same absolute value but with opposite signs appear. This behaviour is the same found in the full numerical solution (Fig. 4.2a). We have found that the system undergoes the bifurcation as the slope of the linear term of the expansion around $P = 0$ of the right hand side of Eq. (4.4b) is varied [69]. The slope is given by:

$$s = \frac{1}{3}\left(\frac{A_+}{k_B T} - 4\right). \tag{4.5}$$

When $s < 1$, $P = 0$ is the only stable solution, while when $s > 1$ the system presents the two stable solutions mentioned above. The bifurcation occurs at $s = 1$. Putting into Eq. (4.5) the parameters for which Fig. 4.5 is obtained we find that the bifurcation takes place when $A_L = 80.43\,\mu$eV. Therefore, Eq. (4.5) provides an expression that relates the hyperfine coupling intensity with the temperature and the bifurcation which, in addition, can be observed through the hysteresis plots measured for the current through the DQD versus the external field [34, 35, 37, 41]. Finally, we find that the agreement between the induced nuclei spin polarization obtained with the full calculation for $B_{\text{ext}} = 0$, and the one obtained with this simplified model is very good.

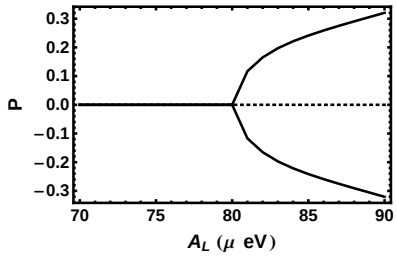

Figure 4.5: Solutions for Eq. (4.4b) for $B_{\text{ext}} = 0$. The induced nuclei spin polarization presents a bifurcation. When $A_L \leq 80.43\,\mu$eV, there is only one stable solution, which corresponds to having the nuclei spins fully depolarized (solid line). However, when $A_L > 80.43\,\mu$eV, $P = 0$ becomes an unstable solution (dashed line) and two stable solutions show up (solid lines). Same parameters as in Fig. 4.2.

From the current through the right contact barrier $I_R = (\Gamma_{+,T_x} + \Gamma_{-,T_x})\rho_{T_x}$ (see Eq. (5.9)), and from Eq. (4.4a) we obtain the following expression for the current through the DQD:

$$I = \left(1 + \frac{1}{2\mathcal{N}^2}\right) \frac{1 - p_t^2}{3 + \frac{\beta}{\omega_+^{tt}} + p_t^2}\,\beta \tag{4.6}$$

Notice that $\beta = 0$ when $P = 0$ (see Eq. (3.19)), thus, the current will be zero when the nuclei spins are fully depolarized. In the previous discussion, we have shown that the induced nuclei spin polarization shows a bifurcation when increasing the HF coupling intensity. Therefore, in the range of A_L where the nuclei spins are fully depolarized (Fig. 4.5) no current flows through the DQD at $B_{\text{ext}} = 0$. However, in the range of A_L where the nuclei have a non zero spin polarization (Fig. 4.5), a finite current flows through the DQD at $B_{\text{ext}} = 0$, since $I(B_{\text{ext}} = 0) \propto P^2$ to lowest order in P. Furthermore, Eq. (4.6) shows that the current depends on the ratio β/ω_+^{tt}. These rates are shown in Fig. 4.4, and motivate the physical picture we have used to understand the transition from a current dip to a current peak. Therefore, this simplified model shows that the bifurcation obtained for the induced nuclei spin polarization together with the ratio β/ω_+^{tt}, describe the transition from a current dip to a current peak (Fig. 4.2d).

4.2.3 Large magnetic fields

In this section, we consider larger magnetic fields than in the previous case in order to account for the ST crossings. This means sweeping the external field from $B_{\text{ext}} < B_{S_\pm,T_\mp}$ to $B_{\text{ext}} > B_{S_\pm,T_\pm}$ (see schematic Figs. 4.1a and 4.1d). Therefore all three level crossings ($S_\pm T_\mp$, $S_\pm T_\pm$ and $T_\pm T_x$) will be considered (see Figs. 4.6a and 4.6b). Fig. 4.6 shows the DQD energy levels, the induced nuclear spin polarization and the leakage current through the DQD versus the external magnetic field, for $A_L = 70\,\mu$eV

and $A_L = 90\,\mu$eV. In this case all figures include feedback and the external field is swept forwards and backwards.

Nuclear spin polarization versus the external field is shown in Figs. 4.6c ($A_L = 70\,\mu$eV) and 4.6d ($A_L = 90\,\mu$eV). The external field sweeping starts for $B_{\rm ext} < B_{S_\pm,T_\mp}$. Initially, the nuclei spins are completely depolarized. The DQD energy level distribution shows that T_+ triplet is the ground state (see Figs. 4.6a and 4.6b). In this case, all spin-flip emission rates polarize negatively the nuclei spins (see Eq. (4.1a)) and, hence, they become almost completely negatively polarized ($P \simeq -1$). Furthermore, since the probability of finding a nuclei with spin $+1/2$ is nearly zero when $P \sim -1$ (see Eq. (3.24)), all emission rates become approximately zero (see Eq. (3.29)), and the nuclei spin polarization remains roughly constant until $B_{\rm ext}$ reaches the $S_\pm T_\mp$ crossings. Only close enough to the $S_\pm T_\mp$ level crossings, spin-flip absorption processes become significant and the nuclei spins dramatically depolarize (Figs. 4.6c and 4.6d). In the $B_{S_\pm,T_\mp} < B_{\rm ext} < B_{S_\pm,T_\pm}$ range of magnetic fields (schematic Figs. 4.1b and 4.1c), several spin-flip rates compete in order to polarize the nuclei spins in opposite directions (see Eqs. (4.1b) and (4.1c)). When $B_{S_\pm,T_\mp} < B_{\rm ext} < B_{TT}$ (scheme in Fig. 4.1d), most of the spin-flip emission rates polarize negatively the nuclei spins (see Eq. (4.1b)), and the resulting nuclear spin polarization is negative in this region. However, as the levels approach the $T_\pm T_x$ crossings, spin-flip absorption processes become more relevant, and the nuclei spins slowly depolarize. When $B_{TT} < B_{\rm ext} < B_{S_\pm,T_\pm}$ (scheme in Fig. 4.1c), most of the spin-flip emission rates polarize positively the nuclei spins (see Eq. (4.1c)), and the nuclear spin polarization is positive in this region. Finally, when $B_{\rm ext} > B_{S_\pm,T_\pm}$, the T_- triplet is the ground state (scheme in Fig. 4.1d), and Eq. (4.1d) shows that all spin-flip emission rates polarize positively the nuclei spins, thus, they become almost completely positively polarized ($P \simeq 1$). The probability of finding a nuclei with spin $-1/2$ is nearly zero as $P \sim 1$ (see Eq. (3.24)), thus, all emission rates become approximately zero (see Eq. (3.29)), and the nuclei spin polarization remains roughly constant.

Figs. 4.6c and 4.6d show that the feedback between electron and nuclei spins produces hysteresis in the nuclear polarization around the ST-crossings. Recall that for small magnetic fields (section 4.2.1), where only $T_\pm T_x$ crossings participate, hysteresis was not observed for small HF intensities, but only the largest HF coupling intensity considered here ($A_L = 90\,\mu$eV). For larger external magnetic fields, however, hysteresis shows up at ST crossings even for the smallest HF intensity considered ($A_L = 70\,\mu$eV). Finally, as for small magnetic fields, hysteresis is larger as the HF coupling increases.

The leakage current through the DQD versus the external field is shown in Figs. 4.6e ($A_L = 70\,\mu$eV) and 4.6f ($A_L = 90\,\mu$eV). The current presents three peaks, each of them corresponding to one of the three possible level crossings. When $B_{\rm ext} < B_{S_\pm T_\mp}$ ($B_{\rm ext} > B_{S_\pm T_\pm}$), the current is zero because electrons are trapped in the T_+ (T_-) triplet state (Figs. 4.6a and 4.6b), thus, in these ranges of the external field spin-flip emission rates are nearly zero. In between these crossings (when $B_{S_\pm,T_\mp} < B_{\rm ext} < B_{S_\pm,T_\pm}$), current is strongly quenched but nevertheless finite. This

case has been discussed in section 4.2.1. Finally, the feedback between the nuclei and the electron spins also produces hysteresis in the current around the ST crossings, when sweeping the external field forwards and backwards.

4.3 Dependence on the interdot tunnelling strength

In this section, we show the leakage current and the induced nuclear spin polarization dependence on the interdot tunnelling intensity. Interdot tunnel varies a lot from one experiment to another and can be externally tuned. For instance, in [33] it is estimated to be around $30\,\mu$eV, while in [34] around $0.2\,\mu$eV. This justifies the large difference between the two values that we have chosen. We consider small external magnetic fields, and two different interdot tunnel values (Figs. 4.7a and 4.7b). For the largest value of the interdot tunnel ($t_{LR} = 50\,\mu$eV) only the $T_{\pm}T_x$ crossing participate in the current. However, for the smallest value of the interdot tunnel ($t_{LR} = 0.01\,\mu$eV), all crossings: $S_{\pm}, T_{\mp}$, $T_{\pm}T_x$ and $S_{\pm}, T_{\pm}$ participate in the current, for the same range of the external field. Fig. 4.7 shows also the induced nuclear spin polarization (Figs. 4.7c and 4.7d) and the leakage current through the DQD (Figs. 4.7e and 4.7f) versus the external magnetic field for the two interdot tunnelling intensities chosen: $t_{LR} = 50\,\mu$eV and $t_{LR} = 0.01\,\mu$eV, and for $A_L = 80\,\mu$eV.

Figs. 4.7c and 4.7d show that for the smallest interdot tunnelling ($t_{LR} = 0.01\,\mu$eV), the behaviour of the polarization versus the external magnetic field is smoother than for the largest interdot tunnelling considered ($t_{LR} = 50\,\mu$eV), due to the stronger competition between the energy absorption and emission processes in the former case. For the small interdot tunnelling, absorption is more efficient than for the large interdot tunnelling value.

Figs. 4.7e and 4.7f show that decreasing the interdot tunnelling, the current versus the magnetic field presents again a transition from a dip to a peak. As in the previous case, where we discussed the current behaviour as a function of the intensity of the HF interaction, a dip or a peak features observed in the current can be understood comparing the spin-flip rate between $T_{\pm}$ and T_x and the tunnelling rate through the barrier contact between T_x and $|\pm\rangle$ states (Fig. 4.4b). However, unlike in the previous case, where the HF coupling had to be increased to observe the transition, now, in order to go from a dip to a peak, the interdot tunnelling must decrease.

4.4 Conclusions

We have studied the leakage current through a coherently coupled DQD in SB regime. Spin relaxation due to HF interaction between the spins of the electrons in the DQD and the nuclei spins lifts SB producing leakage current. Moreover, the spin interaction between electrons tunnelling through the DQD and nuclei, induces dynamical nuclear spin polarization that is in general non-negligible. We have investigated the

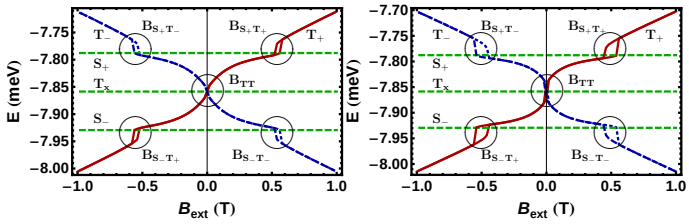

(a) $A_L = 70\,\mu$eV (b) $A_L = 90\,\mu$eV

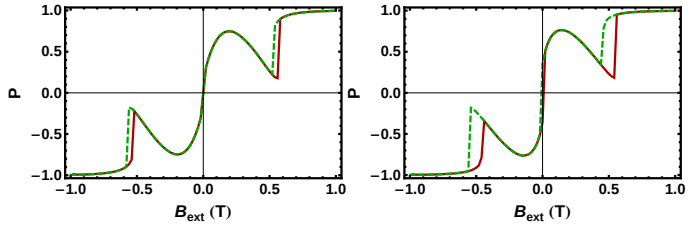

(c) $A_L = 70\,\mu$eV (d) $A_L = 90\,\mu$eV

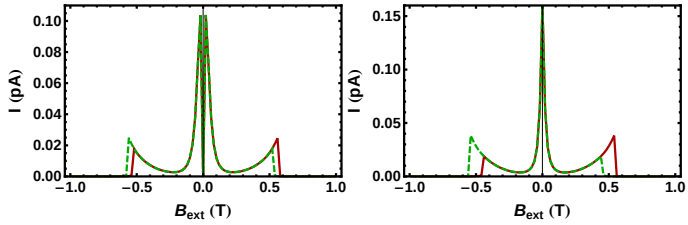

(e) $A_L = 70\,\mu$eV (f) $A_L = 90\,\mu$eV

Figure 4.6: a), b) Energy levels versus external magnetic field. T_+ (solid, red online), T_- (dotted, blue online), T_x, S_+, S_- (dashed, green online); c), d) induced nuclear spin polarization, and e), f) leakage current versus external magnetic field sweeping forwards (solid, red online) and backwards (dashed, green online). Same parameters and initial conditions than in Fig. 4.2. The range of magnetic fields considered includes both ST and the $T_\pm T_x$ crossings. Hysteresis is observed for both values of the HF coupling intensity at the ST crossings. Recall that in Fig. 4.2, where only the $T_\pm$ crossing was shown, hysteresis was only found for the largest value of the HF intensity ($A_L = 90\,\mu$eV). The current shows now three peaks corresponding mainly to each of the levels crossings.

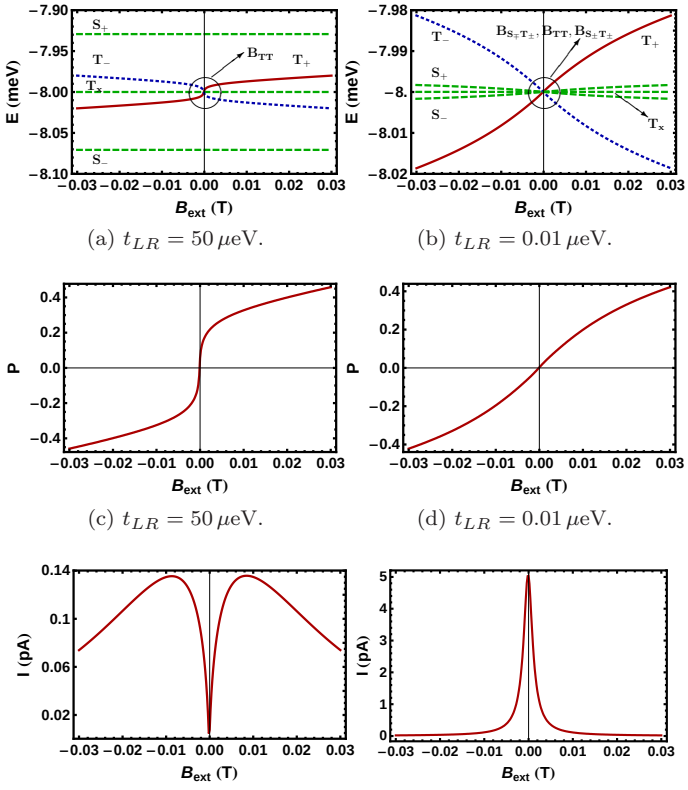

(a) $t_{LR} = 50\,\mu$eV. (b) $t_{LR} = 0.01\,\mu$eV.

(c) $t_{LR} = 50\,\mu$eV. (d) $t_{LR} = 0.01\,\mu$eV.

(e) $t_{LR} = 50\,\mu$eV. (f) $t_{LR} = 0.01\,\mu$eV.

Figure 4.7: a), b) Energy levels versus external magnetic field. T_+ (solid, red online), T_- (dotted, blue online), T_x, S_+, S_- (dashed, green online); c), d) induced nuclear spin polarization, and e), f) leakage current versus external magnetic field. $A_L = 80\,\mu$eV. The remaining parameters and the initial conditions are the same as in Fig. 4.2. The current shows a dip (peak) for the largest (smallest) value of the interdot tunnel intensity. Although feedback between the electron and the nuclear spin polarization is taken into account in these figures, hysteresis is not observed for this set of parameters.

behaviour of both the induced nuclear spin polarization and the leakage current as a function of an external magnetic field. Our three main results are: i) the leakage current shows a dip or a peak depending on the intensities of both the HF interaction and the interdot tunnel strength. We have shown that for large (small) HF coupling (interdot tunnelling) intensities the current shows a peak. On the contrary, for small (large) HF coupling (interdot tunnelling) intensities the current shows a dip. Large (small) HF couplings (interdot tunnelling) indicate strong mixing between the singlet-triplet subspaces, namely, the effective Zeeman splitting difference between the dots is non-negligible with respect to the exchange energy. In this case the leakage current shows a peak. On the contrary, small (large) HF couplings (interdot tunnelling) indicate a weak mixing between the singlet-triplet subspaces, the Zeeman splitting difference between dots becomes negligible with respect to the exchange energy, and the system is mostly blocked in the triplet subspace. In this case the leakage current shows a dip. The crossover from a dip to a peak is, thus, obtained by increasing (decreasing) the HF interaction (interdot tunnelling strength). ii) For a wide external magnetic field sweeping range, we have shown that the leakage current shows three main peaks. Two satellite peaks corresponding to the ST crossings and a central peak corresponding to the triplets crossing. iii) We have observed hysteresis in both the leakage current and the induced nuclear spin polarization as a function of an external magnetic field. This hysteretic behaviour is a consequence of the dynamical nuclear spin polarization interacting with the electron spin that tunnel through the DQD structure. Finally, we have shown that the size of the hysteresis region strongly depends on the HF interaction intensity and the interdot tunnel strength.

Our results are a contribution to ongoing efforts at understanding and controlling spin relaxation in qubits, which limitate their performance for quantum information and quantum computation purposes.

Chapter 5

Spin induced nonlinear electron transport in a quantum dot

In this chapter we investigate non-linear magneto-transport through a single level quantum dot driven by a spin-dependent bias, where the electron spin is coupled to a large, external (pseudo-)spin via an anisotropic exchange interaction. We find regimes where the average current through the dot displays self-sustained oscillations that reflect the limit-cycles and chaos and map the dependence of this behavior on magnetic field strength and the tunnel coupling to the external leads.

5.1 Introduction

Single-electron transport through nanostructures has developed into a powerful spectroscopic tool for probing correlations, quantum coherence, and interactions with the environment on a microscopic level [70–73]. Some recent examples include experiments with semiconductor quantum dots that have provided detailed insight into level structures [3, 71, 74], Coulomb and spin-blockade effects [33], phonon emission [75], or the statistics of individual electron tunnel events [76–78].

In this work, we propose the time-dependent, average current of electrons through a single level quantum dot as probe for classical non-linear dynamics and chaos [69]. Specifically, we consider electronic magneto-transport through a quantum dot containing two spin-split levels with an anisotropic coupling between the electron spin and an external, classical magnetic moment or pseudo-spin. In order to have a spin-polarizied current through the quantum dot, the source-drain chemicals potentials are taken to be different for spin-up and spin-down electrons (see Refs. [79, 80] and references there in), meaning the bias voltage that drives the current is spin-

dependent.

Previous works have analyzed the anisotropic interaction between two spins in a *closed* system under an external magnetic field [81–85], showing either regular (integrable) or chaotic (nonintegrable) classical orbits. The results presented here demonstrate that the signatures of non-linear dynamics and classical chaos of the closed system also persist in the non-equilibrium regime, where the additional coupling to the electronic reservoirs leads to an even richer dynamics that can be probed, e.g., by varying the magnetic field and the tunnel rates. In particular, one finds a transition from a regime with damped current transients and a constant current, to a situation where the current displays self-sustained regular limit-cycle oscillations, or chaotic behaviour. Limit-cycles in transport have also been found recently in theoretical calculations in mesoscopic systems coupled to mechanical degrees of freedom [86, 87].

Experimental inspiration for our model comes from the hyperfine interaction in quantum dots. The interaction of electron spins in quantum dots with surrounding nuclear spins is usually viewed as simply giving rise to spin relaxation and decoherence [46, 88]. Recently, however, transport experiments through semiconductor double quantum dots have shown non-linear current behaviour which has been attributed to hyperfine interaction inducing a dynamical nuclear spin polarization [34, 41, 44]. The feedback between electron and nuclei spin polarization gives rise to nontrivial features in the current, including self-sustained oscillations [34, 41]. In this setting, the large spin of our model represents an effective description of the collective nuclear spin system [89] and the electronic part provides a minimal model for investigating the effects on transport of coupled spin-spin dynamics.

A further potential realisation of the large spin in our model is a magnetic impurity in a quantum dot. Several recent works have considered the influence of such an impurity on the transport properties through the dot [90–93]. In this context, our model can be viewed as the large-spin counterpart of the previously studied models and in particular the spin-1/2 impurity model of Refs. [91, 93]. This possibility is also closely related to transport through single molecular magnets [94–96], for which our large spin would map to a magnetic atom and the isolated levels of our quantum dot to molecular orbitals.

We mention that our study of classical chaos in a quantum dot with coupling to an external pseudo-spin is also complementary to previous studies of intrinsic *quantum* chaos of, e.g., ballistic quantum dots. Those latter systems are often analysed with statistical tools such as random matrix theory [97, 98].

The outline of this work is as follows. In Section II, we introduce the model Hamiltonian and the equations of motion. Section III presents results and a classification of various non-linear regimes in the form of a map in parameter space, and we conclude with a brief discussion of the experimental relevance of our finding in Section IV.

5.2 Model

5.2.1 Hamiltonian

We investigate a quantum dot (QD) with a single orbital level, coupled to an emitter (left electron lead), a collector (right electron lead) and to a *large* spin $\hat{\mathbf{J}}$ (Fig. 5.1a). An external magnetic field B_z is applied in z-direction which splits the QD spin levels (Fig. 5.1b). The Hamiltonian for this model is

$$\hat{H} \;=\; \hat{H}_{FA} + \hat{H}_J + \hat{V}. \tag{5.1}$$

Here, $\hat{H}_{FA}$ is the Fano-Anderson model for the QD coupled to the leads, which is exactly solvable; $\hat{H}_J$ is the Hamiltonian for the free motion of the large spin due the external magnetic field; and $\hat{V}$ is the coupling between a dot electron and the large spin. These individual Hamiltonians read:

$$\begin{aligned}
\hat{H}_{FA} &= \sum_{\sigma} \epsilon_d \hat{d}^\dagger_\sigma \hat{d}_\sigma + B_z \hat{S}_z \\
&+ \sum_{lk\sigma} \epsilon_{lk\sigma} \hat{c}^\dagger_{lk\sigma} \hat{c}_{lk\sigma} + \sum_{lk\sigma} \left(\gamma_{lk} \hat{c}^\dagger_{lk\sigma} \hat{d}_\sigma + \text{h.c.} \right), && (5.2a)\\
\hat{H}_J &= B_z \hat{J}_z \,, && (5.2b)\\
\hat{V} &= \sum_{i=x,y,z} \lambda_i \hat{S}_i \hat{J}_i \,, && (5.2c)
\end{aligned}$$

where ϵ_d is the energy of the QD level, $\hat{d}^\dagger_\sigma / \hat{d}_\sigma$ creates/annihilates a spin-σ electron in the dot, $\hat{S}_i$ is the i-th component of the electron spin operator in second quantization, $\hat{J}_i$ is the i-th component of large spin operator, and λ_i is the coupling between the i-th components of the electron and the large spin, $\hat{c}^\dagger_{lk\sigma} / \hat{c}_{lk\sigma}$ creates/annihilates an electron with momentum k and spin σ in lead $l \in \{L, R\}$, and γ_{lk} is the coupling between the QD and the l-th lead. Coulomb interaction in the QD is neglected, and thus double occupation is allowed. For simplicity, we absorb the Bohr magneton and the g-factors into the definition of B_z, and assume identical g-factors for the electron and the large spin. A generalization to different g-factors is straightforward.

The classical counterpart of the closed system ($\gamma_{lk} = 0$) is, for zero external magnetic field ($B_z = 0$), a completely integrable system for arbitrary λ_i [84], while the isotropic model ($\lambda_x = \lambda_y = \lambda_z$) is also completely integrable for finite external magnetic fields. However, in presence of a finite magnetic field, an *anisotropic* coupling between the electron spin and the large spin, makes the model non-integrable and can lead to a chaotic spin dynamics [85]. Therefore, in this work we take the coupling between the electron spin and the large spin to be anisotropic, and for simplicity we will focus on the choice

$$\lambda_x = \lambda_z = \lambda, \quad \lambda_y = 0. \tag{5.3}$$

Finally, the spin-dependent chemical potentials of the leads are chosen so that only spin-up electrons can tunnel out of the QD (Fig. 5.1b), namely, $B_z \gg k_B T$ where

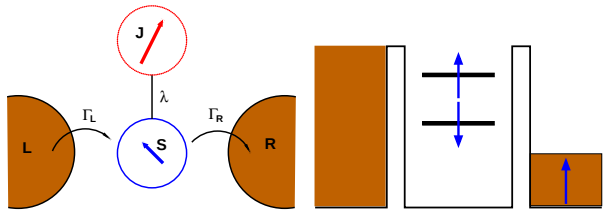

Figure 5.1: Scheme and setup of the investigated system. a) An electron spin $\hat{\mathbf{S}}$ (blue arrow) in a QD is coupled via the exchange interaction λ with a large spin $\hat{\mathbf{J}}$ (red arrow). The QD is attached to electron reservoirs (brown regions), allowing electrons to tunnel through the QD. The large spin is isolated. b) The spin-dependent chemical potentials of the leads are tuned so that a spin down electron is always trapped in the QD, while spin up electrons can tunnel through it (see details in the text). The large spin interacts with the spin of the electron trapped in the QD, allowing its spin to flip and, hence, escape form the QD into the right lead.

T is the temperature of the leads and k_B is Boltzmann's constant. In the following, we restrict ourselves to the zero temperature case. In this regime, current can flow only through the spin-up level of the QD. When an electron enters the spin-down level, it remains trapped until a spin-flip process (due to the interaction with the large spin) produces a transition from the spin-down to the spin-up level, allowing the trapped electron to escape the QD. Notice that because we have taken identical g-factors for both the electron spin and the large spin, the spin-flip transition from the QD spin-down to the spin-up level conserves energy and the energy that the electron absorbs in the spin-flip is emitted by the large spin.

5.2.2 Equations of Motion

The equation of motion (EOM) for the expectation value of an operator $\hat{A}$ is

$$\frac{d}{dt}\langle \hat{A}\rangle \quad = \quad \frac{1}{i\hbar}\langle[\hat{A},\hat{H}]\rangle + \left\langle \frac{\partial \hat{A}}{\partial t}\right\rangle . \tag{5.4}$$

Using this formula, we derive the EOM of each operator in Eq. (5.2a), Eq. (5.2b) and Eq. (5.2c).

We first observe that the length of the large spin $j = |\hat{\mathbf{J}}|$ is a conserved quantity since $[\hat{\mathbf{J}}^2, \hat{H}] = 0$. Next, due to the interaction $\hat{V}$, the EOMs do not close and lead to an infinite hierarchy of equations that needs to be truncated. In order to do so, we use a factorization approximation by invoking a *mean-field* approximation for $\hat{V} \to \hat{V}_{MF}$,

$$\hat{V}_{MF} \quad = \quad \sum_{i=x,y,x} \lambda_i \left(\hat{S}_i \langle \hat{J}_i\rangle + \hat{J}_i \langle \hat{S}_i\rangle - \langle \hat{S}_i\rangle\langle \hat{J}_i\rangle \right) \tag{5.5}$$

which neglects the term $\delta\hat{S}_i\delta\hat{J}_i$ with $\delta\hat{S}_i = \hat{S}_i - \langle\hat{S}_i\rangle$ and $\delta\hat{J}_i = \hat{J}_i - \langle\hat{J}_i\rangle$, i.e. the quantum fluctuations of the electron spin and the external spin. We expect this to be a good approximation when $j \gg 1$ and the external spin $\hat{\mathbf{J}}$ can essentially be treated as a classical object due to its interaction with other environmental degrees of freedom. Furthermore, as in the semiclassical approximation we neglect quantum fluctuations of the large spin, we have no spin decay, meaning the large spin is a constant of motion.

We furthermore neglect terms proportional to $\gamma_{lk}\lambda_i$, namely, second order transitions due to the coupling of the large spin with the contacts. This is a good approximation for weak coupling to the electron leads, for which we perform the usual Born-Markov and white band approximations and consider them to be in thermal equilibrium. Moreover, we consider the infinite bias regime. However, in order to allow current to flow only through the spin-up dot level, we choose the left and right lead chemical potentials to be $\mu_L \to \infty$, and $\mu_{R\uparrow} \to -\infty$ and $\mu_{R\downarrow} \to \infty$, respectively (see Appendix C.1 for details). The resulting EOMs read

$$\begin{aligned}
\frac{d}{dt}\langle\hat{n}_\sigma\rangle &= \lambda\langle\hat{J}_x\rangle\langle\hat{S}_y\rangle\left(\delta_{\sigma\uparrow} - \delta_{\sigma\downarrow}\right) - \Gamma\langle\hat{n}_\sigma\rangle \\
&+ \frac{\Gamma_L}{2} + \Gamma_{R\downarrow}\delta_{\sigma\downarrow} \\
\frac{d}{dt}\langle\hat{S}_x\rangle &= -\left(\lambda\langle\hat{J}_z\rangle + B_z\right)\langle\hat{S}_y\rangle - \Gamma\langle\hat{S}_x\rangle \\
\frac{d}{dt}\langle\hat{S}_y\rangle &= -\lambda\langle\hat{J}_x\rangle\langle\hat{S}_z\rangle + \left(\lambda\langle\hat{J}_z\rangle + B_z\right)\langle\hat{S}_x\rangle - \Gamma\langle\hat{S}_y\rangle \\
\frac{d}{dt}\langle\hat{S}_z\rangle &= \lambda\langle\hat{J}_x\rangle\langle\hat{S}_y\rangle - \Gamma\langle\hat{S}_z\rangle - \Gamma_{R\downarrow} \\
\frac{d}{dt}\langle\hat{J}_x\rangle &= -\left(\lambda\langle\hat{S}_z\rangle + B_z\right)\langle\hat{J}_y\rangle \\
\frac{d}{dt}\langle\hat{J}_y\rangle &= -\lambda\langle\hat{S}_x\rangle\langle\hat{J}_z\rangle + \left(\lambda\langle\hat{S}_z\rangle + B_z\right)\langle\hat{J}_x\rangle \\
\frac{d}{dt}\langle\hat{J}_z\rangle &= \lambda\langle\hat{S}_x\rangle\langle\hat{J}_y\rangle,
\end{aligned} \tag{5.6}$$

where $\hat{n}_\sigma = \hat{d}^\dagger_\sigma\hat{d}_\sigma$, $\delta_{\sigma,\sigma'}$ is the Kronecker delta and $\Gamma = \Gamma_L/2 + \Gamma_{R(\sigma}$ where $\sigma = \uparrow, \downarrow$, Γ_L and $\Gamma_{R\sigma}$ are the tunnelling rates through the left and right contact barriers, respectively.

The EOM for the total number of electrons in the QD ($\hat{N} = \hat{n}_\uparrow + \hat{n}_\downarrow$) is independent of both the electron and the large spin components and is exactly solvable (see Appendix C.1). Thus, as $2\hat{S}_z = \hat{n}_\uparrow - \hat{n}_\downarrow$, the level occupations can be obtained through the following expression:

$$\begin{aligned}
\langle\hat{n}_\sigma(t)\rangle &= \frac{1}{2}\left(\langle\hat{N}(0)\rangle\, e^{-\Gamma t} + \frac{\Gamma_L + \Gamma_{R\downarrow}}{\Gamma}\left(1 - e^{-\Gamma t}\right)\right) \\
&+ (\delta_{\sigma\uparrow} - \delta_{\sigma\downarrow})\langle\hat{S}_z(t)\rangle
\end{aligned} \tag{5.7}$$

which relates the level occupation with the z-component of the electron spin. If the coupling between the electron and the large spins is isotropic ($\lambda_x = \lambda_y = \lambda_z$), it is straightforward to see that in the stationary limit the spins decouple, and the well known Fano-Anderson solution is obtained (see Appendix C.2). In contrast, we show below that the situation is drastically different for the anisotropic case where the stationary solutions for the EOMs depend on the coupling between the spins.

The average electron current $\langle \hat{I} \rangle$ through the QD is solely due to a decay at rate $\Gamma_{R\uparrow}$ from the spin-up QD level into the right lead,

$$\langle \hat{I}(t) \rangle = e\Gamma_{R\uparrow} \langle \hat{n}_\uparrow(t) \rangle, \tag{5.8}$$

where e denotes the electron charge. In the long-time limit of the current can be written as (see Eq. (5.7))

$$\frac{\langle \hat{I}(t) \rangle}{e\Gamma_{R\uparrow}} = \frac{1}{2} \frac{\Gamma_L + \Gamma_{R\downarrow}}{\Gamma} + \langle \hat{S}_z(t) \rangle. \tag{5.9}$$

Henceforth, for convenience we take $\Gamma_{R\downarrow} = \Gamma/4$. Other options give similar behaviour except for the transient solutions.

5.3 Regions in parameter space

The stationary solutions of the EOMs, Eq. (5.6), can be obtained analytically and we find eight fixed points. Two of these fixed points, however, always have a finite imaginary component, and as they have no physical meaning, we leave them out of the subsequent analysis. The remaining fixed points serve to divide the parameter space of the model into distinct regions, as shown in Fig. 5.2.

Introducing the notation

$$\mathcal{P} = \left(\langle \hat{S}_x \rangle, \langle \hat{S}_y \rangle, \langle \hat{S}_z \rangle, \langle \hat{J}_x \rangle, \langle \hat{J}_y \rangle, \langle \hat{J}_z \rangle \right), \tag{5.10}$$

the six relevant fixed points are

$$\mathcal{P}_\pm = \left(0, 0, -\frac{1}{4}, 0, 0, \pm j \right), \tag{5.11a}$$

$$\mathcal{P}_{\mathrm{II},1_\pm} = \left(0, \mathcal{B}_2, -\frac{B_z}{\lambda}, \frac{\Gamma}{B_z}\mathcal{B}_2, \pm\mathcal{B}_1, -\frac{B_z}{\lambda} \right), \tag{5.11b}$$

$$\mathcal{P}_{\mathrm{II},2_\pm} = \left(0, -\mathcal{B}_2, -\frac{B_z}{\lambda}, -\frac{\Gamma}{B_z}\mathcal{B}_2, \pm\mathcal{B}_1, -\frac{B_z}{\lambda} \right), \tag{5.11c}$$

where

$$\mathcal{B}_1 = -\sqrt{j^2 - \left(\frac{\lambda}{4B_z} - 1 \right) \left(\frac{\Gamma}{\lambda} \right)^2 - \left(\frac{B_z}{\lambda} \right)^2}, \tag{5.12a}$$

$$\mathcal{B}_2 = -\sqrt{\frac{B_z}{\lambda} \left(\frac{1}{4} - \frac{B_z}{\lambda} \right)}. \tag{5.12b}$$

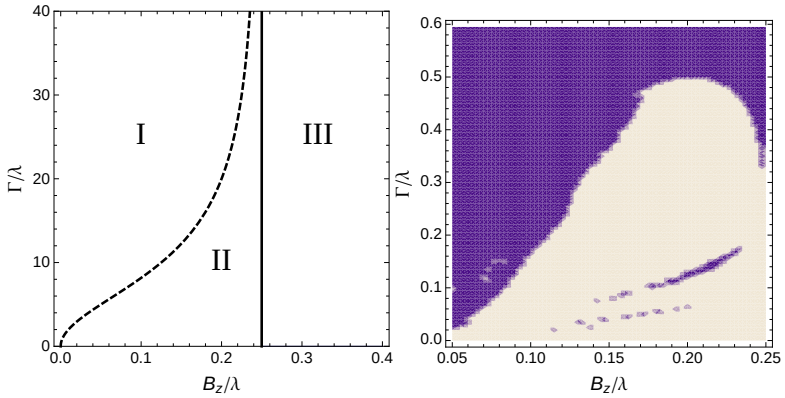

Figure 5.2: (a) Parameter space with three regions describing the behaviour of solutions of EOMs (Eq. (5.6)). Boundaries between the regions are obtained analytically from Eq. (5.13). Region I: damped oscillations (Fig. 5.3); region II (mixed region in between I and III): both damped and self-sustained oscillations; region III: only self-sustained oscillations (Fig. 5.6). (b) Numerically obtained zoom of the region in mixed region II where self-sustained oscillations are found. Dark region: damped oscillations are obtained; light region: self-sustained oscillations. Initial conditions: $\langle \hat{S}_x \rangle_{t=0} = 1/2$ and $\langle \hat{S}_y \rangle_{t=0} = \langle \hat{S}_z \rangle_{t=0} = 0$, $\langle \hat{J}_x \rangle_{t=0} = \langle \hat{J}_y \rangle_{t=0} = j/2$ and $\langle \hat{J}_x \rangle_{t=0} = j/\sqrt{2}$.

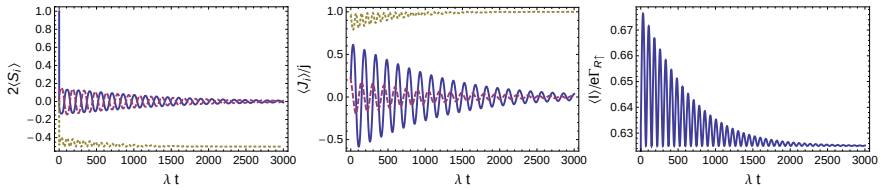

(a) (b) (c)

Figure 5.3: Time evolution in region I of a) the electron spin components, b) the large spin components, and c) the current through the QD obtained by solving numerically the EOMs of Eq. (5.6). Plotted are: $2\langle\hat{S}_x\rangle$ ($\langle\hat{J}_x\rangle/j$), solid line; $2\langle\hat{S}_y\rangle$ ($\langle\hat{J}_y\rangle/j$), dashed line; and $2\langle\hat{S}_z\rangle$ ($\langle\hat{J}_z\rangle/j$), dotted line. In this region, the solutions exhibit a slow damped behaviour. In the stationary limit, the large spin is completely polarized in the direction parallel to the external magnetic field, and a QD electron trapped in the spin-down state. Current is due only to tunnelling through the spin up level and in the stationary limit tends to a constant value of 5/8. The parameters here are $B_z/\lambda = 0.1$ and $\Gamma/\lambda = 9$, with initial conditions $\langle\hat{S}_x\rangle_{t=0} = 1/2$, $\langle\hat{S}_y\rangle_{t=0} = \langle\hat{S}_z\rangle_{t=0} = 0$, $\langle\hat{J}_x\rangle_{t=0} = \langle\hat{J}_y\rangle_{t=0} = (5/\sqrt{2})(\sqrt{5}-1)/2$ and $\langle\hat{J}_z\rangle_{t=0} = (5/\sqrt{2})\sqrt{5+\sqrt{5}}$.

For certain values of B_z, Γ and λ, the quantities $\mathcal{B}_1$ and $\mathcal{B}_2$ ((5.12a) and Eq. (5.12b)) can have finite imaginary components and therefore, points $\mathcal{P}_{\mathrm{II},1_\pm}$ and $\mathcal{P}_{\mathrm{II},2_\pm}$ only have physical meaning in the region of parameter space where $\mathcal{B}_1$ and $\mathcal{B}_2$ are real. Fig. 5.2a shows a projection of the 3-dimensional parameter space on the Γ versus B_z plane for a fixed λ. This diagram is divided in three regions. In region I, $\mathcal{B}_1$ is a pure imaginary number, and hence, $\mathcal{P}_{\mathrm{II},1_\pm}$ and $\mathcal{P}_{\mathrm{II},2_\pm}$ are nonphysical, and $\mathcal{P}_\pm$ the only physical fixed points. In region II, $\mathcal{B}_1$ and $\mathcal{B}_2$ are both real, and all six fixed points are physical. In region III, $\mathcal{B}_2$ is purely imaginary, and again $\mathcal{P}_\pm$ are the only physical fixed points. Points $\mathcal{P}_\pm$ are thus physical solutions for the EOMs Eq. (5.6) in all three regions, whereas the fixed points $\mathcal{P}_{\mathrm{II},\pm}$ are physical only in region II. The boundaries between the regions are obtained by solving the equations $\mathcal{B}_1 = 0$ and $\mathcal{B}_2 = 0$, namely

$$\begin{aligned} \mathcal{B}_1 = 0 \quad &\Rightarrow \quad \Gamma = \sqrt{\frac{j^2 - (B_z/\lambda)^2}{1/4 - B_z/\lambda}\,\frac{B_z}{\lambda}}, \\ \mathcal{B}_2 = 0 \quad &\Rightarrow \quad \frac{B_z}{\lambda} = \frac{1}{4}, \end{aligned} \tag{5.13}$$

and these two equations give the lines plotted in Fig. 5.2a.

Region I

In order to obtain the time evolution of the electron and large spin components and the electronic current through the QD, the EOMs Eq. (5.6) are solved numerically.

Fig. 5.3 shows the time evolution of the electron spin and the large spin components, and the current through the QD in region I of the parameter space. All exhibit completely damped oscillations. In the previous discussion, we have seen that in region I, $\mathcal{P}_{\pm}$ Eq. (5.11a) are the only physical fixed points. Depending on the choice of parameters and initial conditions, the system will evolve to $\mathcal{P}_{+}$ or $\mathcal{P}_{-}$. For the parameters and initial conditions chosen in Fig. 5.3, the system evolves towards the fixed point $\mathcal{P}_{+}$. In this case, the large spin becomes completely polarized in the direction parallel to the external magnetic field (Fig. 5.3b), and a spin-down electron remains trapped in the QD (Fig. 5.3a) and the interaction between the electron spin and the large spin is no longer effective. Spin-up electrons, however, can still tunnel through the QD (Fig. 5.3c), and in the stationary limit the current becomes (see Eq. (5.9))

$$\frac{\langle \hat{I}(t) \rangle}{e\Gamma_{R\uparrow}} = \frac{5}{8}. \tag{5.14}$$

In region I, then, the coupling of the two spin systems with the external leads results in complete damping of the transient oscillations of the electron and the large spin components and the current. A finite, fully spin-polarized electron current flows through the QD that in the stationary limit is not influenced by the interaction with the large spin.

Region II

In region II, the EOMs Eq. (5.6) exhibit both damped and self-sustained oscillatory solutions, depending on the choice of parameters and initial conditions. Fig. 5.2b shows the part of region II where the self-sustained oscillations are found. This behaviour can be seen for all intensities of the external magnetic field in region II, but only for small values of coupling Γ with the leads. Comparing Fig. 5.2a and 5.2b we see that most values for B_z and Γ in region II lead to damped oscillations. Furthermore, although we have given analytical expressions for the boundaries between the different regions Eq. (5.13), we have not found an expression for the boundary between the regions inside region II where self-sustained and damped oscillations are found. Fig. 5.2b has been obtained by solving the EOMs Eq. (5.6) in region II. As can be seen, the boundary between both regions is fuzzy in contrast with the ones obtained between regions I, II and III Eq. (5.13). Moreover, Fig. 5.2b shows small "islands" in the oscillatory region, where damped solutions are obtained.

Damped Oscillations

Figs. 5.4a, 5.4b and 5.4c, show the time evolution of the electron and the large spin components, and the current in region II with parameters B_z and Γ such that they all exhibit damped oscillations. Previously we have seen that in region II all the six fixed points are physical. For the parameters and initial conditions chosen in Figs. 5.4a, 5.4b and 5.4c, the system evolves towards the fixed point $\mathcal{P}_{\mathrm{II},1+}$. The large spin

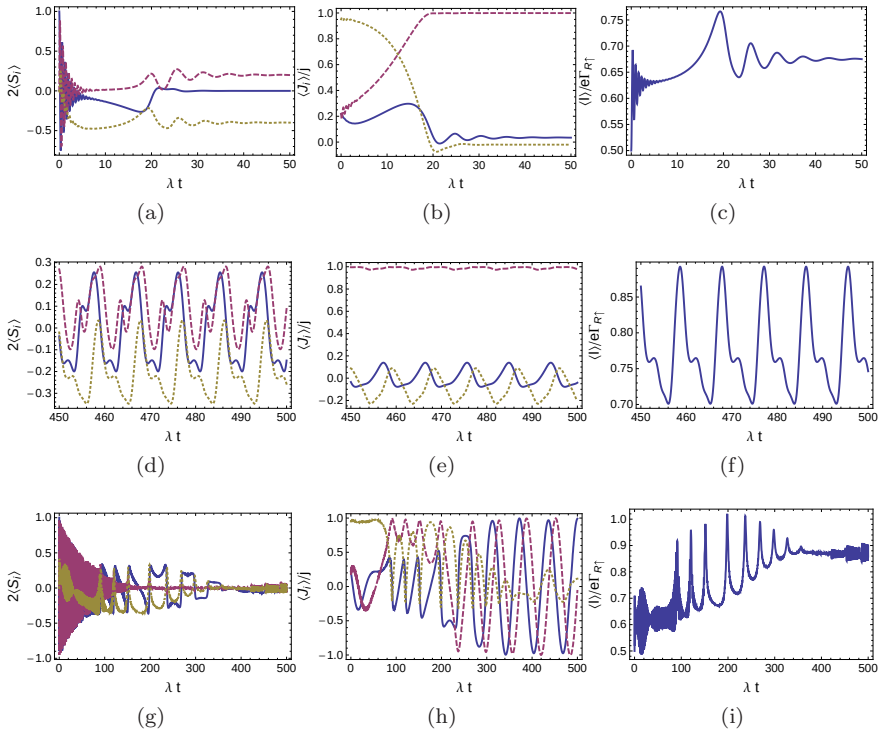

Figure 5.4: Same as Fig. 5.3 but in region II. Results for three different parameter sets are shown, each of which gives rise to very different system behaviour. Figs. a), b), c) show fast damping behaviour ($B_z/\lambda = 0.2$, $\Gamma/\lambda = 0.7$, dark region in Fig. 5.2b). In the long-time limit the large spin is almost completely polarized in the direction perpendicular to the external field, but unlike in region I, the spin down electron can escape from the QD into the right lead due to the interaction with the large spin. Figs. d), e), f) show periodic self-sustained oscillations ($B_z/\lambda = 0.1$, $\Gamma/\lambda = 0.16$, light region in Fig. 5.2b), which is a signature of limit-cycles in phase space (see Fig. 5.6). Figs. g), h), i) show chaotic self-sustained oscillations ($B_z/\lambda = 0.1$, $\Gamma/\lambda = 0.015$, light region in Fig. 5.2b). In the oscillatory cases, the oscillations are captured in the current through the QD, and in particular, the chaotic behaviour is observed in the current (Fig. 5.4i). The initial conditions are $\langle \hat{S}_x \rangle_{t=0} = 1/2$, $\langle \hat{S}_y \rangle_{t=0} = \langle \hat{S}_z \rangle_{t=0} = 0$, $\langle \hat{J}_x \rangle_{t=0} = \langle \hat{J}_y \rangle_{t=0} = (5/\sqrt{2})(\sqrt{5}-1)/2$ and $\langle \hat{J}_z \rangle_{t=0} = (5/\sqrt{2})\sqrt{5+\sqrt{5}}$.

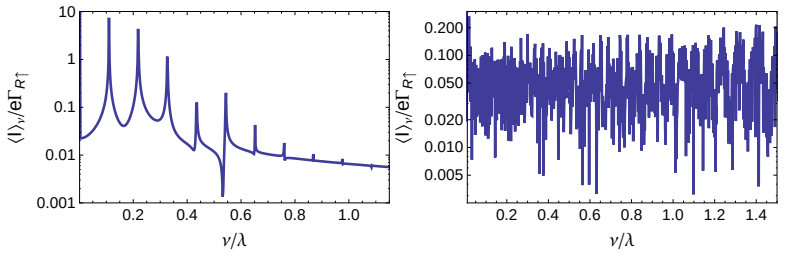

(a) (b)

Figure 5.5: Fourier spectra of the non-damped current time evolutions shown in Fig. 5.4 in the long-time limit. Figs. a) and b) show the Fourier transform of Fig 5.4f and 5.4i, respectively, where ν is the frequency. Figure a) shows peaks at well defined frequencies, meaning that behaviour of the current is periodic. However, figure c) shows a uniform frequency distribution, which is a signature of chaotic dynamics.

becomes almost completely polarized in the y-direction (Fig. 5.4b), perpendicular to the external magnetic field. and the current becomes (see Eq. (5.9))

$$\frac{\langle \hat{I} \rangle}{e\Gamma_{R\uparrow}} = \frac{7}{8} - \frac{B_z}{\lambda}. \tag{5.15}$$

Thus, the stationary current increases if either the external magnetic field decreases or the coupling between the spins increases. Since in region II $B_z/\lambda < 1/4$, the coupling between the electron and the large spins enhances the current through the QD, compared with the current obtained in region I (Eq. (5.14)). Nevertheless, the result of coupling the two spins to the leads stills yields complete damping of both spin oscillations, as in region I.

Self-Sustained Oscillations and Chaos

We shall now focus on the small region in region II where self-sustained oscillatory solutions are found (Fig. 5.2b). Figs. 5.4d, 5.4e and 5.4f, show the time evolution of the electron and the large spin components, and the current through the QD. The chosen values of B_z and Γ lead to complicated, but periodic, undamped oscillations. Fig. 5.5a shows the Fourier spectrum of the current time evolution of Fig. 5.4f in the long-time limit. The spectrum exhibits peaks at well defined frequencies, which clearly confirms the periodic behaviour of the current. Furthermore, in non-linear systems, self-sustained oscillations are a signature of *limit-cycles* and in Figs. 5.6a and 5.6b we plot the electron and the large spin trajectories in phase space, projected on the x-z plane, in the long-time limit. These figures show that the spin trajectories are precisely limit-cycles. For all the initial conditions chosen, the system always converges to them. Finally, Figs. 5.4g, 5.4h and 5.4i show that decreasing Γ turns

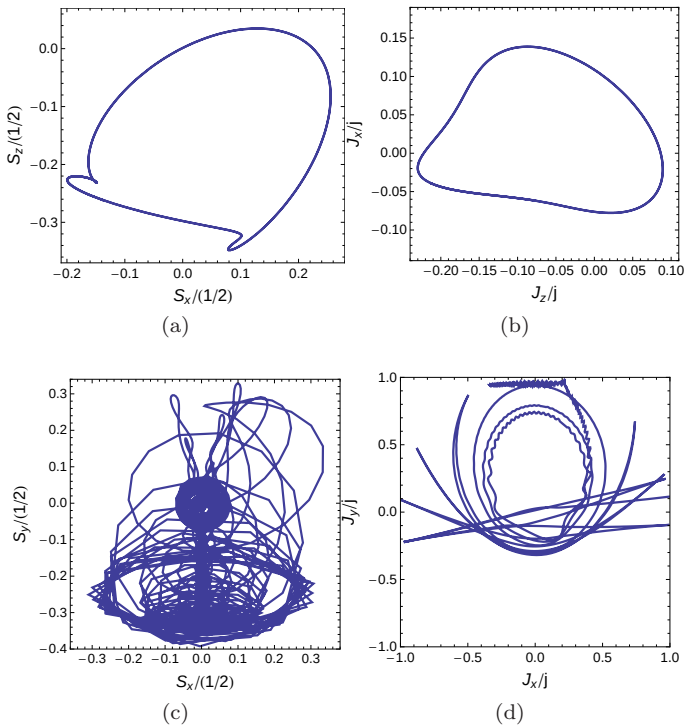

Figure 5.6: Electron spin (left figures) and large spin (right) trajectories projected on a two dimensional plane for the non-damped solutions in region II (light region in Fig. 5.2a). Figs. a) and b) show the formation of a limit-cycle as seen in the time evolution plots, Fig. 5.4d, 5.4e, and 5.4f ($B_z/\lambda = 0.1$, $\Gamma/\lambda = 0.16$). Figs. c) and d) correspond to the time evolution plots of Figs. 5.4g, 5.4h, and 5.4i which suggest that the trajectories are chaotic ($B_z/\lambda = 0.1$, $\Gamma/\lambda = 0.015$).

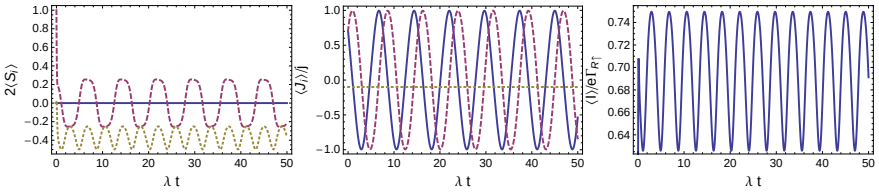

(a) (b) (c)

Figure 5.7: Same as Fig. 5.3 but for region III. In this region the solutions exhibit periodic self-sustained oscillations, which are reflected in the current. The corresponding limit-cycles are shown in Fig. 5.8). The parameters chosen here are $B_z/\lambda = 1.0$, $\Gamma/\lambda = 10$. The initial conditions are $\langle \hat{S}_y \rangle_{t=0} = 1/2$, $\langle \hat{S}_x \rangle_{t=0} = \langle \hat{S}_z \rangle_{t=0} = 0$, $\langle \hat{J}_x \rangle_{t=0} = \langle \hat{J}_y \rangle_{t=0} = 3\sqrt{11/2}$ and $\langle \hat{J}_z \rangle_{t=0} = -1$.

the periodic self-sustained oscillations chaotic. In this case, the Fourier spectrum of the current, shown in Fig. 5.5b, is uniformly distributed through all frequencies, which is a clear signature of chaos. Figs. 5.6c and 5.6d show the electron and large spin trajectories in the long-time limit, where it can be seen that they perform complicated non-periodic paths. In this area of region II, the coupling between the interacting spins and the leads does not produce damping of the spins as in the previous cases. Moreover, the electron current through the QD captures the complicated dynamics due to the interaction between the electron and the large spin, as seen in Figs. 5.4f and 5.4i.

Region III

Figs. 5.7a, 5.7b and 5.7c show the time evolution of the spin components and current for typical parameters in region III. They all exhibit periodic self-sustained oscillations. Fig. 5.8 shows the different limit-cycles performed by the electron spin in phase space, projected in the y-z plain, when the value of the external magnetic field is increased. The trajectories found for the large spin in the long-time limit suggest that this behaviour can be understood by means of an effective model in which the large spin simply acts on the QD electrons as an ac magnetic field in x-direction with amplitude

$$B_{\rm ac}(t) \quad = \quad \frac{\lambda j}{\sqrt{2}} \left(\cos(B_z t) - \sin(B_z t)\right). \tag{5.16}$$

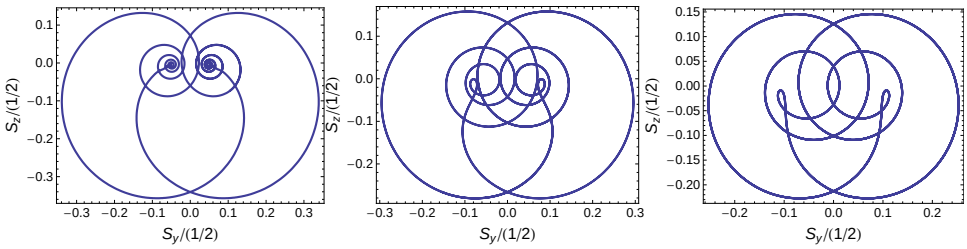

(a) $B_z/\lambda = 0.4$ (b) $B_z/\lambda = 0.8$ (c) $B_z/\lambda = 1.2$

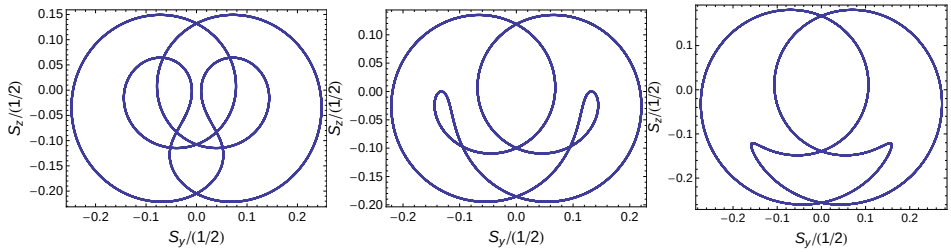

(d) $B_z/\lambda = 1.6$ (e) $B_z/\lambda = 2.0$ (f) $B_z/\lambda = 2.4$

Figure 5.8: Electron spin trajectories projected in the $\langle \hat{S}_y \rangle$-$\langle \hat{S}_z \rangle$ plane in region III. The solutions of the EOMs given in Eq. (5.6) are periodic self-sustained oscillations (Fig. 5.7). Figs. a)-f) show the different limit-cycles obtained when varying the external magnetic field. $\Gamma/\lambda = 1$.

The EOMs for this effective model are (see Appendix C.3 for details)

$$\begin{aligned}
\frac{d}{dt}\langle\hat{S}_x\rangle &= -B_z\langle\hat{S}_y\rangle - \Gamma\langle\hat{S}_x\rangle \\
\frac{d}{dt}\langle\hat{S}_y\rangle &= B_z\langle\hat{S}_x\rangle - B_{\rm ac}(t)\langle\hat{S}_z\rangle - \Gamma\langle\hat{S}_y\rangle \\
\frac{d}{dt}\langle\hat{S}_z\rangle &= B_{\rm ac}(t)\langle\hat{S}_y\rangle - \Gamma\langle\hat{S}_z\rangle - \Gamma_{R\downarrow}.
\end{aligned} \tag{5.17}$$

Thus, in this region the six autonomous non-linear equations Eq. (5.6) can be approximated by a set of three non-autonomous linear equations Eq. (5.17). The agreement between the solutions obtained with this effective model and the full EOMs is very good.

In region III, the coupling between the two spin system leads to self-sustained oscillations which are visible in the electron current through the QD, as shown in Fig. 5.7c.

5.4 Conclusions

We have studied electron transport through a quantum dot driven by a spin-dependent bias, in which the electron spin interacts with a large spin while an external magnetic field is applied. We have found that the motion of the electron spin, the large spin and the current through the QD strongly depend on the coupling between spins. When the electron spin and the large spin are isotropically coupled, the large spin becomes completely polarized and decouples from the electron spin. Conversely, when the electron spin and the large spin are anisotropicaly coupled, we have found that their motion and the current through the QD can either behave as in the isotropic case or show self-sustained oscillations which, furthermore, can be periodic or chaotic. Switching between different behaviours can be obtained by varying either the strength coupling with the leads or the intensity of the external magnetic field.

We foresee two possible experimental realisations of the large spin of our model. The first is as an effective model on a hyperfine bath. Here a semi-classical treatment may be justified by considering that the number of nuclei spins in semiconductor QDs interacting with an electron spin is very large (e.g., for GaAs QDs there are typically 10^5-10^6 nuclei spins). Situations in which the hyperfine interaction is anisotropic have been discussed in Refs. [99–101]. The second realisation is that our large spin represents the spin of a magnetic impurity of a doped semiconductor or a magnetic atom in a single molecular magnet. While in this case the spin may not be so large, mean-field analyses such as pursued here can still provide useful information, e.g. Ref. [102].

From the theoretical point of view, it would be interesting to investigate how the features of this semiclassical treatment are reflected in a quantum master equation approach, in which the electron and the large spin are both treated as quantum

objects. This opens a path to investigate the quantum/classical divide in a nonequillibrium context.

Appendix A

The spin blockade regime

In chapters 3 and 4 we studied electron transport through a double quantum dot in the spin-blockade regime. We assumed the bias and the gate voltages were chosen such that the system was already in the SB regime. In this appendix we take a step back and obtain the SB current-voltage characteristic (see, for e.g. Ref. [33]) using the rate equations technique as in those chapters.

A.1 Model

Since we assume only one orbital level per quantum dot, there can be at most four electrons in it ($|\uparrow\downarrow,\uparrow\downarrow\rangle$). However, in the bias window we are interested in we consider that the the maximum number of electrons in the DQD is two. Therefore, the relevant states for the transport process are $\{|0,0\rangle, |1,0\rangle,\ |0,1\rangle,\ |1,1\rangle,\ |2,0\rangle,\ |0,2\rangle\}$.

The Hamiltonian is:

$$\hat{H} = \hat{H}_{DQD} + \hat{V}_{LR}, \tag{A.1}$$

with

$$\hat{H}_{DQD} = \sum_{l\sigma} \epsilon_l \hat{n}_{l\sigma} + \sum_{l} U_l \hat{n}_{l\uparrow}\hat{n}_{l\downarrow} + U_{LR} \sum_{\sigma\sigma'} \hat{n}_{L\sigma}\hat{n}_{R\sigma'} \tag{A.2}$$

$$\hat{V}_{LR} = t_{LR} \sum_{\sigma} \left(\hat{d}^{\dagger}_{L\sigma}\hat{d}_{R\sigma} + \text{h.c} \right), \tag{A.3}$$

where $l = L$ (left dot), R (right dot) and $\sigma = \uparrow, \downarrow$. We consider the two quantum dots are weakly coupled, so we can treat the interdot tunneling term $\hat{V}_{LR}$ as a perturbation[1]. Moreover, we are interested in the particular case where $\mu_D(1,1) = \mu_D(0,2)$, namely, when states $|1,1\rangle$ and $|0,2\rangle$ are aligned (*resonant transport*), meaning we

[1] Although the complete Hamiltonian is diagonalizable in general, the expressions obtained are too large to use them.

must use degenerate perturbation theory. In this case we first have to diagonalize $\hat{V}_{LR}$ in the degenerate subspace $\{|1,1\rangle, |0,2\rangle\}$. Taking into account the spin degrees of freedom it leaves us with a five dimensional space, but as tunnel must conserve the total spin, $|T_+\rangle = |\uparrow,\uparrow\rangle$ and $|T_-\rangle = |\downarrow,\downarrow\rangle$ triplets do not couple with $|0,2\rangle$, so at the end, the matrix we have to diagonalize is three dimensional. The eigenstates and eigenenergies of this matrix are:

$$\begin{aligned} |T_0\rangle &= \frac{1}{\sqrt{2}}\left(|\uparrow,\downarrow\rangle + |\downarrow,\uparrow\rangle\right) \\ |S_\pm\rangle &= \frac{1}{2}\left(|\uparrow,\downarrow\rangle - |\downarrow,\uparrow\rangle \pm \sqrt{2}\,|0,\uparrow\downarrow\rangle\right) \end{aligned} \tag{A.4}$$

and:

$$\begin{aligned} E_{T_0} &= 2\Delta + U_{LR} \\ E_{S_\pm} &= 2\Delta + U_{LR} \pm \sqrt{2}\,t_{LR} \end{aligned} \tag{A.5}$$

where $2\Delta \equiv \epsilon_L + \epsilon_R$. The basis we are left with now is $\{|0,0\rangle, |1,0\rangle, |0,1\rangle, |S_\pm\rangle, |2,0\rangle, |T_0\rangle, |T_\pm\rangle\}$ where the degeneration has been removed. The next step would be to use non-degenerate perturbation theory in order to couple $|1,0\rangle$ and $|0,1\rangle$, and $|S_\pm\rangle$ and $|2,0\rangle$. Nevertheless, the condition $\mu_D(1,1) = \mu_D(0,2)$ means that:

$$2\delta = U_R - U_{LR} \tag{A.6}$$

where $2\delta \equiv \epsilon_L - \epsilon_R$ is the *detunning*. The first order corrections are proportional to t_{LR}/δ which are small enough -compared to the strong mixing between $|1,1\rangle$ and $|0,2\rangle$- for us to safely neglect them. Therefore, from now on we will consider these new states as the eigenbasis of DQD.

A.2 Rate equations

The DQD is coupled to the leads through the term $\hat{V}_T$ (see Eq. (3.2)). The rate equations for the occupations of the DQD states is written in matrix form as follows:

$$\dot{\rho} = T\rho \tag{A.7}$$

where:

$$T_{mn} = \begin{cases} \Gamma_{mn} & \text{if} \quad m \neq n \\ -\sum_{n\neq m}\Gamma_{nm} & \text{if} \quad n = m \end{cases} \tag{A.8}$$

and $\Gamma_{mn} = \Gamma^L_{mn} + \Gamma^R_{mn}$, where Γ^l_{mn} is the tunneling rate from the initial state n to the final state m through the l-th. The tunneling rate for the transition between the DQD states $|\alpha_N\rangle$ and $|\beta_{N+1}\rangle$ (incoming electrons) through the l-th barrier is obtained by Fermi's Golden Rule:

$$\Gamma^l_{\beta_{N+1},\alpha_N} = 2\pi \sum_{i_l k\sigma} |\langle \beta_{N+1}|\langle i_l|\hat{c}^\dagger_{lk\sigma}\hat{V}_T|i_l\rangle|\alpha_N\rangle|^2\, W_{i_l}\, \delta(E_{\beta_{N+1}} - \epsilon_{lk} - E_{\alpha_N})$$

with the final state being $\hat{c}_{lk\sigma}|i_l\rangle|\beta_{N+1}\rangle$ where $|i_l\rangle$ is the initial lead state, $|\beta_{N+1}\rangle$ the final dot state and N the number of electrons in the DQD. The sum over initial states runs over all configurations of the internal degrees of freedom, i_l, that give the state $|\alpha_N\rangle$ each weighted by a thermal distribution W_{i_l}. Introducing $\hat{V}_T$ we obtain:

$$\Gamma^l_{\beta_{N+1},\alpha_N} = 2\pi \sum_{k\sigma} |\gamma_{lk\sigma}|^2 |\langle \beta_{N+1}|\hat{d}^\dagger_{l\sigma}|\alpha_N\rangle|^2 \, f(\epsilon_{lk}-\mu_l)\, \delta(E_{\beta_{N+1}} - \epsilon_{lk\sigma} - E_{\alpha_N}),$$

where we have assumed the leads are in thermal equilibrium, thus

$$\sum_{i_l} \langle i_l|\hat{c}^\dagger_{lk\sigma}\hat{c}_{lk\sigma}|i_l\rangle \, W_{i_l} = f(\epsilon_{lk}-\mu_l) \tag{A.9}$$

and $f(\epsilon)$ is the Fermi distribution and μ_l the chemical potential of lead l. The next step is to deal with the summation over the k-states. Assuming the tunneling matrix γ_{lk} and the density of states D_l of the lead do not depend on energy, then

$$2\pi \sum_k |\gamma_{lk}|^2 \, f(\epsilon_{lk}-\mu_l)\, \delta(E_{\beta_{N+1}} - \epsilon_{lk} - E_{\alpha_N}) =$$

$$2\pi \int d\epsilon \, |\gamma(\epsilon)|^2 D(\epsilon)\, f(\epsilon-\mu_l)\delta(E_{\beta_{N+1}} - \epsilon - E_{\alpha_N}) = \Gamma_l f(\mu_D - \mu_l) \tag{A.10}$$

where $\Gamma_l = 2\pi D_l |\gamma_{lk}|^2$ and $\mu_D = E_{\beta_{N+1}} - E_{\alpha_N}$ is the chemical potential of the DQD. Finally, the expression we arrive to for the tunneling rate is:

$$\Gamma^l_{\beta_{N+1},\alpha_N} = \Gamma_l f(\mu_D - \mu_l) \sum_\sigma |\langle \beta_{N+1}|\hat{d}^\dagger_{l\sigma}|\alpha_N\rangle|^2 \tag{A.11}$$

In the same fashion, the rate for outcoming electrons is given by:

$$\Gamma^l_{\beta_{N-1},\alpha_N} = \Gamma_l [1 - f(\mu_D - \mu_l)] \sum_\sigma |\langle \beta_{N-1}|\hat{d}_{l\sigma}|\alpha_N\rangle|^2$$

The probability $P(N)$ of having N electrons in the DQD is the sum over the probabilities of each DQD state with N electrons. Hence, the average total number of electrons in the DQD is $N_T = P(1) + 2P(2)$. The current through the l-th lead is:

$$I_l = (-e) \sum_N \left(\Gamma^l_{N+1,N} - \Gamma^l_{N-1,N}\right) P(N) \tag{A.12}$$

A.3 Results

Fig. A.2 a) shows N_T and b) $P(0)$, $P(1)$ and $P(2)$, in the stationary limit, as a function of the gate voltage (Δ) for $V_{SD} = 0$. In this figure we see that when $\Delta \in (2, 4]$ meV $N_T = 0$ and $P(0) = 1$, the DQD is empty because the chemical potential of all the DQD states is larger than the source-drain voltage ($\mu_D > V_{SD}$).

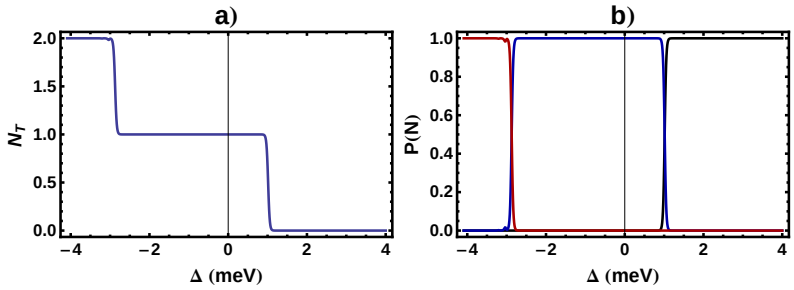

Figure A.1: a) Total number of electrons inside the DQD. b) Probability for the DQD of being empty, $P(0)$ (black line), for it to have one electron inside, $P(1)$ (blue line) and for it to have two electrons inside (red line). Parameters: $V_{SD} = 0$, $t_{LR} = 0.1\,\text{meV}$, $U_L = U_R = U$, $U_{LR} = U/2$, $U = 4$ meV, $k_B T = 0.02\,\text{meV}$ and $\Gamma_L = \Gamma_R = 0.01\,\text{meV}$.

When $\Delta \in (-3, 1)\,\text{meV}$ $N_T = 1$ and $P(1) = 1$, thus, there is one electron inside the DQD because the chemical potential of some or all of the one electron states is larger than the source-drain voltage. And, finally, when $\Delta \in [-4, -3)\,\text{meV}$ $N_T = 2$ and $P(2) = 1$, and there are two electrons inside the DQD because the chemical potential of some or all of the two electron states is larger than the source-drain voltage. When $\Delta \approx 1\,\text{meV}$ $0 < N_T < 1$, i.e., the number of electrons inside the DQD varies between zero and one, therefore for a finite source-drain voltage current can flow through it. Likewise, when $\Delta \approx -3\,\text{meV}$ $1 < N_T < 2$, i.e., the number of electrons inside the DQD varies between one and two, therefore for a finite source-drain voltage current can flow through it.

Figs. A.2 a), b) and c) show the total number of electrons, the current and occupations of the DQD levels in the stationary limit as a function the source-drain voltage. Fig. A.2 a) shows that in the range $V_{SD} \in (0.5, 3.5)\,\text{meV}$, there are two electrons trapped in the DQD. Fig. A.2 b) shows that in this region the current is zero. Finally, Fig. A.2 c) shows that the occupied states are the triplet states. Therefore, for these values of source-drain voltage the system is in the SB regime.

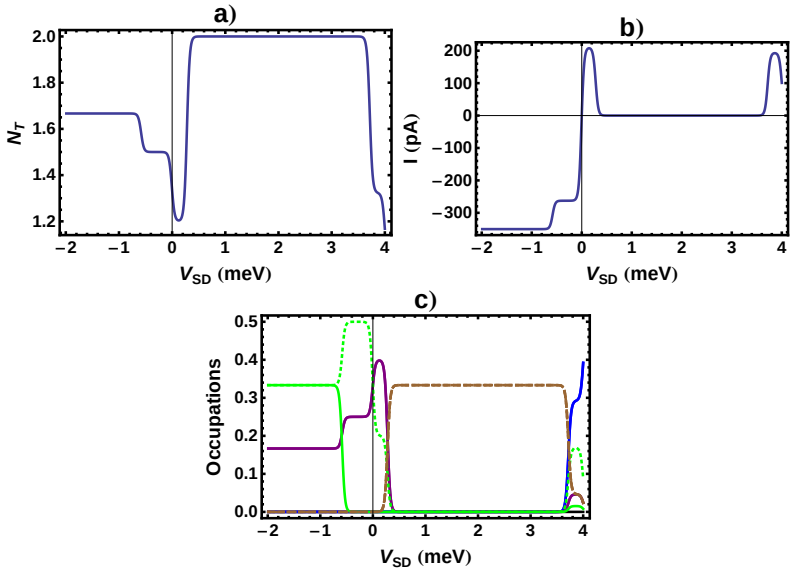

Figure A.2: a) Total number of electrons inside the DQD (N_T). b) Current through the DQD. Notice how for $V_{SD} \in (0.5, 3.5)$ meV current goes to zero due to SB. c) DQD occupations. Green (dotted) lines correspond to singlet S_+ (S_-), brown to triplet states, purple to $|0,1\rangle$ blue to $|1,0\rangle$ and black to the empty state, the occupations for $|2,0\rangle$ is always zero. Notice that in the SB region only triplet states are occupied (brown lines), namely, $T_\pm$ and T_0. The parameters are the same as in Fig. except for $\Delta = \sqrt{2}\, t_{LR} - 3U/4$ ($P(1) = P(2)$, see Fig. A.2 b)).

Appendix B

Hyperfine interaction in quantum dots

B.1 Atomic hyperfine interaction

Hyperfine structure effects are responsible for splittings of the energy levels in atoms. These effects result from the fact that the nucleus may possess *electromagnetic multipole moments* (of higher order than the electric monopole) which can interact with the electromagnetic field produced at the nucleus by electrons. The most important of these moments are the *magnetic dipole moment* (associated with the nuclear spin) and the *electrical quadrupole moment* (caused from the departure from a spherical charge distribution of nucleus). In this thesis we are mainly concerned with the magnetic dipole moment.

A nuclei with a finite spin, considered as a "point dipole", has a magnetic dipole moment

$$\hat{\mathbf{m}}_n = g_n \mu_n \hat{\mathbf{I}}. \tag{B.1}$$

where g_n is a dimensionless number (whose order of magnitude is unity) called the *nuclear g-factor* or *nuclear Landé factor*, and the quantity μ_n is called the *nuclear magneton*, which is defined

$$\mu_n = \frac{e\hbar}{2m_p} = \frac{m_e}{m_p}\,\mu_B \tag{B.2}$$

where m_e is the mass of the electron, m_p the mass of the proton and μ_B the Bohr magneton. Thus, the nuclear magneton μ_n is smaller that the Bohr magneton by the factor $m_e/m_p = 1/1836.15$. The numerical value of the nuclear magneton is

$$\mu_n = 5.05082 \times 10^{-27}\text{Joule/Tesla}. \tag{B.3}$$

The Hamiltonian for a magnetic dipole moment in a magnetic field is

$$\hat{H} = -\hat{\mathbf{m}}_n \cdot \mathbf{B}. \tag{B.4}$$

In absence of external magnetic fields, the only magnetic field felt by the nuclei is the one produced by the electron, which is due to its angular momentum, $\hat{\mathbf{L}}$, and its spin, $\hat{\mathbf{S}}$: $\mathbf{B}_{\rm el} = \mathbf{B}_l + \mathbf{B}_s$. The magnetic field due to the angular momentum of the electron can be written as:

$$\mathbf{B}_l = -2\mu_B \frac{\mu_0}{4\pi} \frac{\hat{\mathbf{l}}}{r^3} \tag{B.5}$$

where $\hat{\mathbf{l}} = \hat{\mathbf{L}}/\hbar$ and μ_0 is the vacuum permeability. The electron spin has a magnetic dipole moment:

$$\hat{\mathbf{m}}_s = -g_s \mu_B \hat{\mathbf{S}}, \tag{B.6}$$

which also is responsible for a magnetic field. Thus, the Hamiltonian (B.4) is shown to be [62]

$$\begin{aligned}
\hat{H} &= -\hat{\mathbf{m}}_n \cdot \mathbf{B}_{\rm el} = -\hat{\mathbf{m}}_n \cdot (\mathbf{B}_l + \mathbf{B}_s) \\
&= \frac{\mu_0}{4\pi} \left[2\mu_B \frac{\hat{\mathbf{m}}_\mathbf{n} \cdot \hat{\mathbf{l}}}{r^3} - \frac{3(\hat{\mathbf{m}}_n \cdot \mathbf{n})(\hat{\mathbf{m}}_s \cdot \mathbf{n}) - \hat{\mathbf{m}}_n \cdot \hat{\mathbf{m}}_s}{r^3} - \frac{8\pi}{3} \hat{\mathbf{m}}_n \cdot \hat{\mathbf{m}}_s \, \delta(\mathbf{r}) \right] \\
&= \mu_0 g_n \mu_n \mu_B \frac{1}{2\pi r^3} \hat{\mathbf{I}} \cdot \hat{l} && \text{(B.7)} \\
&+ \mu_0 g_n \mu_n g_s \mu_B \frac{1}{4\pi r^3} \left[3(\hat{\mathbf{I}} \cdot \mathbf{n})(\hat{\mathbf{S}} \cdot \mathbf{n}) - \hat{\mathbf{I}} \cdot \hat{\mathbf{S}} \right] && \text{(B.8)} \\
&+ \mu_0 g_n \mu_n g_s \mu_B \frac{2}{3} \hat{\mathbf{I}} \cdot \hat{\mathbf{S}} \, \delta(\mathbf{r}). && \text{(B.9)}
\end{aligned}$$

The term (B.7), as said above, may be interpreted as the interaction between the nuclear dipole moment $\hat{\mathbf{m}}_n$ with the magnetic field created at the nucleus by the rotation of the electronic charge (Eq. (B.5)). The term (B.8) represents the dipole-dipole interaction between the magnetic moments of the electron and the nucleus. Note that Eqs. (B.7) and (B.8) are the same as in the classical limit. Both terms, have non-zero matrix elements between states with finite orbital angular momentum, $l \neq 0$, since they are only valid for $r \neq 0$. However, the last term, Eq. (B.9), will only be relevant for states with zero angular momentum, $l = 0$ (s-states), and will vanish for $r \neq 0$. Eq. (B.9) is known as the *Fermi contact interaction* term. Therefore, as long as the electronic wave function is a p-state, d-state, or other states of non-zero angular momentum, we expect the classical approach (Eqs. (B.7) and (B.8)) to be a good approximation, while for s-states, since the electron wave function is non-zero at the nucleus ($r = 0$), the Hyperfine interaction is given by (B.9).

B.2 Hyperfine interaction in a quantum dot system

The contact interaction (B.9) term is the most important term for describing hyperfine interaction in materials with s-type conduction band electrons, in particular, III-V semiconductors and Silicon. For an electron interacting with many nuclear

spins in a solid the Fermi contact interaction (B.9) term can be written as:

$$\hat{H}_c = \mu_0 \mu_n g_s \mu_B \frac{2}{3} \sum_i g_{ni} \hat{\mathbf{I}}_i \cdot \hat{\mathbf{S}}\, \delta(\mathbf{r}_i) \tag{B.10}$$

where we have assumed only one nuclear species. $\hat{\mathbf{I}}_i$ is a spin operator for a nucleus at the atomic site i. We have seen in chapter 1 that in the envelope-function approximation (section 1.3) the wave function

$$\Psi_{0\sigma}(\mathbf{r}_i) = \sqrt{\nu_0} u_0(\mathbf{r}_i) \chi(\mathbf{r}_i) |\sigma\rangle \tag{B.11}$$

describes an electron confined in quantum dot with a single nondegenerate orbital level, where we have also included the spin states $\sigma = \uparrow, \downarrow$. ν_0 is the atomic volume [99], $u_0(\mathbf{r})$ is the $\mathbf{k} = 0$ Bloch function and $\chi(\mathbf{r})$ the slowly varying envelope function (see Fig. 1.4). When the electron orbital level spacing is large compared to $k_B T$ and the scale of the hyperfine coupling, the electron-nuclear spin system will be well-described by the effective Hamiltonian, projected onto the single-orbital state [57, 58, 99]

$$\begin{aligned} \hat{H}_{hf} &= \langle \Psi_{0\sigma}(\mathbf{r}) | \hat{H}_c | \Psi_{0\sigma'}(\mathbf{r}) \rangle \\ &= \mu_0 \mu_n g_s \mu_B \frac{2}{3} \nu_0 \sum_i g_{ni} |u_0(\mathbf{r}_i)|^2 |\chi(\mathbf{r}_i)|^2 \langle \sigma | \hat{\mathbf{I}}_i \cdot \hat{\mathbf{S}} | \sigma' \rangle \end{aligned} \tag{B.12}$$

which can be written in the form

$$\hat{H}_{hf} = \sum_i A_i \hat{\mathbf{S}} \cdot \hat{\mathbf{I}}_i, \tag{B.13}$$

where $\hat{\mathbf{S}}$ is now the second quantized spin-operator, which we have assumed does dot depend on the lattice site since the electron is confined in the quantum dot [57], and

$$A_i = \frac{2}{3} \mu_0 \mu_n g_s \mu_B \nu_0 g_{ni} |u_0(\mathbf{r}_i)|^2 |\chi(\mathbf{r}_i)|^2. \tag{B.14}$$

The Hamiltonian (B.13) is the Fermi contact interaction term for describing the hyperfine structure in a quantum dot system.

Appendix C

Derivation of the EOMs (5.6). Isotropic and effective models

C.1 Derivation of the equations of motion (5.6)

In this appendix, we summarize the steps in the derivation of the EOMs (Eq. (5.6)). Under the mean-field approximation considered in this work (see Eq. (5.5)), the closed set of EOMs obtained for the time evolution of operators in the Hamiltonian (Eq. (5.1)) when computed with Eq. (5.4) are:

$$
\begin{aligned}
i\,\frac{d}{dt}\,\langle \hat{d}^{\dagger}_{\sigma}\hat{d}_{\sigma'}\rangle &= \frac{\lambda}{2}\left(\delta_{\sigma'\uparrow}\langle \hat{d}^{\dagger}_{\sigma}\hat{d}_{\downarrow}\rangle + \delta_{\sigma'\downarrow}\langle \hat{d}^{\dagger}_{\sigma}\hat{d}_{\uparrow}\rangle - \delta_{\sigma\uparrow}\langle \hat{d}^{\dagger}_{\downarrow}\hat{d}_{\sigma'}\rangle - \delta_{\sigma\downarrow}\langle \hat{d}^{\dagger}_{\uparrow}\hat{d}_{\sigma'}\rangle\right)\langle \hat{J}_x\rangle \\
&+ \frac{1}{2}\left(\delta_{\sigma'\uparrow}\,\langle \hat{d}^{\dagger}_{\sigma}\hat{d}_{\uparrow}\rangle - \delta_{\sigma'\downarrow}\,\langle \hat{d}^{\dagger}_{\sigma}\hat{d}_{\downarrow}\rangle - \delta_{\sigma\uparrow}\,\langle \hat{d}^{\dagger}_{\uparrow}\hat{d}_{\sigma'}\rangle + \delta_{\sigma\downarrow}\,\langle \hat{d}^{\dagger}_{\downarrow}\hat{d}_{\sigma'}\rangle\right) \\
&\times \left(\lambda\langle \hat{J}_z\rangle + B_z\right) - \sum_{l,\,k}\left(\gamma_{lk}\langle \hat{c}^{\dagger}_{lk\sigma}\hat{d}_{\sigma'}\rangle - \gamma^{*}_{lk}\langle \hat{d}^{\dagger}_{\sigma}\hat{c}_{lk\sigma'}\rangle\right) \\
i\,\frac{d}{dt}\,\langle \hat{c}^{\dagger}_{lk\sigma}\hat{d}_{\uparrow}\rangle &= \frac{\lambda}{2}\langle \hat{J}_x\rangle\langle \hat{c}^{\dagger}_{lk\sigma}\hat{d}_{\downarrow}\rangle + \frac{1}{2}\left(\lambda\langle \hat{J}_z\rangle + B_z\right)\langle \hat{c}^{\dagger}_{lk\sigma}\hat{d}_{\uparrow}\rangle \\
&+ \sum_{l',\,k'}\gamma^{*}_{l'k'}\langle \hat{c}^{\dagger}_{lk\sigma}\hat{c}_{l'k'\uparrow}\rangle - \epsilon_{lk\sigma}\langle \hat{c}^{\dagger}_{lk\sigma}\hat{d}_{\uparrow}\rangle - \gamma^{*}_{lk}\langle \hat{d}^{\dagger}_{\sigma}\hat{d}_{\uparrow}\rangle \\
i\,\frac{d}{dt}\,\langle \hat{c}^{\dagger}_{lk\sigma}\hat{d}_{\downarrow}\rangle &= \frac{\lambda}{2}\langle \hat{J}_x\rangle\langle \hat{c}^{\dagger}_{lk\sigma}\hat{d}_{\uparrow}\rangle - \frac{1}{2}\left(\lambda\langle \hat{J}_z\rangle + B_z\right)\langle \hat{c}^{\dagger}_{lk\sigma}\hat{d}_{\downarrow}\rangle \\
&+ \sum_{l',\,k'}\gamma^{*}_{l'k'}\langle \hat{c}^{\dagger}_{lk\sigma}\hat{c}_{l'k'\downarrow}\rangle - \epsilon_{lk\sigma}\langle \hat{c}^{\dagger}_{lk\sigma}\hat{d}_{\downarrow}\rangle - \gamma^{*}_{lk}\langle \hat{d}^{\dagger}_{\sigma}\hat{d}_{\downarrow}\rangle
\end{aligned}
\tag{C.1}
$$

and

$$\begin{aligned}
\frac{d}{dt}\langle \hat{J}_x\rangle &= -\left(\lambda\langle \hat{S}_z\rangle + B_z\right)\langle \hat{J}_y\rangle \\
\frac{d}{dt}\langle \hat{J}_y\rangle &= -\lambda\langle \hat{S}_x\rangle\langle \hat{J}_z\rangle + \left(\lambda\langle \hat{S}_z\rangle + B_z\right)\langle \hat{J}_x\rangle \\
\frac{d}{dt}\langle \hat{J}_z\rangle &= \lambda\langle \hat{S}_x\rangle\langle \hat{J}_y\rangle
\end{aligned} \tag{C.2}$$

where we have used the choice $\lambda_x = \lambda_z = \lambda$ and $\lambda_y = 0$. Since the EOMs for the large spin components have already the desired form (see Eq. (5.6)), hereinafter we shall focus on the time evolution of the electron operators (Eq. (C.1)). Under the Born approximation the leads are are assumed to be in thermal equilibrium for all time,

$$\langle \hat{c}^\dagger_{lk\sigma}\hat{c}_{l'k'\sigma'}\rangle = f_{l\sigma}\,\delta_{ll'}\,\delta_{\sigma\sigma'}\,\delta(k'-k), \tag{C.3}$$

being $f_{l\sigma}$ the equilibrium Fermi-Dirac distribution for electrons in lead l,

$$f_{l\sigma} = \frac{1}{e^{(\epsilon_{lk\sigma}-\mu_{l\sigma})/k_BT}+1}. \tag{C.4}$$

Therefore, applying the Laplace transformation

$$\langle \hat{A}\rangle_s = \int_0^\infty e^{-st}\langle \hat{A}\rangle_t\, dt \tag{C.5}$$

to Eq. (C.1) we obtain:

$$\begin{aligned}
is\,\langle \hat{d}^\dagger_\sigma \hat{d}_{\sigma'}\rangle_s &= \frac{\lambda}{2}\left(\delta_{\sigma'\uparrow}\langle \hat{d}^\dagger_\sigma\hat{d}_\downarrow\rangle_s + \delta_{\sigma'\downarrow}\langle \hat{d}^\dagger_\sigma\hat{d}_\uparrow\rangle_s - \delta_{\sigma\uparrow}\langle \hat{d}^\dagger_\downarrow\hat{d}_{\sigma'}\rangle_s - \delta_{\sigma\downarrow}\langle \hat{d}^\dagger_\uparrow\hat{d}_{\sigma'}\rangle_s\right)\langle \hat{J}_x\rangle_s \\
&+ \frac{1}{2}\left(\delta_{\sigma'\uparrow}\,\langle \hat{d}^\dagger_\sigma\hat{d}_\uparrow\rangle_s - \delta_{\sigma'\downarrow}\,\langle \hat{d}^\dagger_\sigma\hat{d}_\downarrow\rangle_s - \delta_{\sigma\uparrow}\,\langle \hat{d}^\dagger_\uparrow\hat{d}_{\sigma'}\rangle_s + \delta_{\sigma\downarrow}\,\langle \hat{d}^\dagger_\downarrow\hat{d}_{\sigma'}\rangle_s\right) \\
&\times \left(\lambda\langle \hat{J}_z\rangle_s + B_z\right) - \sum_{l,\,k}\left(\gamma_{lk}\langle \hat{c}^\dagger_{lk\sigma}\hat{d}_{\sigma'}\rangle_s - \gamma^*_{lk}\langle \hat{d}^\dagger_\sigma\hat{c}_{lk\sigma'}\rangle_s\right) \\
&+ i\,\langle \hat{d}^\dagger_\sigma\hat{d}_{\sigma'}\rangle_0
\end{aligned} \tag{C.6a}$$

$$\begin{aligned}
is\,\langle \hat{c}^\dagger_{lk\sigma}\hat{d}_\uparrow\rangle_s &= \frac{\lambda}{2}\langle \hat{J}_x\rangle_s\langle \hat{c}^\dagger_{lk\sigma}\hat{d}_\downarrow\rangle_s + \frac{1}{2}\left(\lambda\langle \hat{J}_z\rangle_s + B_z\right)\langle \hat{c}^\dagger_{lk\sigma}\hat{d}_\uparrow\rangle_s + f_{l\sigma}\,\delta_{\sigma\uparrow}\,\gamma^*_{lk} \\
&- \epsilon_{lk\sigma}\langle \hat{c}^\dagger_{lk\sigma}\hat{d}_\uparrow\rangle_s - \gamma^*_{lk}\langle \hat{d}^\dagger_\sigma\hat{d}_\uparrow\rangle_s
\end{aligned} \tag{C.6b}$$

$$\begin{aligned}
is\,\langle \hat{c}^\dagger_{lk\sigma}\hat{d}_\downarrow\rangle_s &= \frac{\lambda}{2}\langle \hat{J}_x\rangle_s\langle \hat{c}^\dagger_{lk\sigma}\hat{d}_\uparrow\rangle_s - \frac{1}{2}\left(\lambda\langle \hat{J}_z\rangle_s + B_z\right)\langle \hat{c}^\dagger_{lk\sigma}\hat{d}_\downarrow\rangle_s + f_{l\sigma}\,\delta_{\sigma\downarrow}\,\gamma^*_{lk} \\
&- \epsilon_{lk\sigma}\langle \hat{c}^\dagger_{lk\sigma}\hat{d}_\downarrow\rangle_s - \gamma^*_{lk}\langle \hat{d}^\dagger_\sigma\hat{d}_\downarrow\rangle_s
\end{aligned} \tag{C.6c}$$

where $s = \eta + i\varepsilon$ and we have taken $\langle \hat{c}^\dagger_{lk\sigma} \hat{d}_{\sigma'} \rangle_0 = 0$. After some algebra, Eq. (C.6b) and Eq. (C.6c) become:

$$\begin{aligned}
\langle \hat{c}^\dagger_{lk\sigma} \hat{d}_\uparrow \rangle_s &= \gamma^*_{lk} \frac{(f_{l\sigma}\, \delta_{\sigma\uparrow} - \langle \hat{d}^\dagger_\sigma \hat{d}_\uparrow \rangle_s)}{\epsilon_{lk\sigma} - \frac{1}{2}(\lambda \langle \hat{J}_z \rangle_s + B_z) + is + \frac{1}{2} \frac{\lambda^2 \langle \hat{J}_x \rangle_s^2}{\lambda \langle \hat{J}_z \rangle_s + B_z + 2(is + \epsilon_{lk\sigma})}} \\
&+ \frac{2\gamma^*_{lk} \lambda \langle \hat{J}_x \rangle_s (\langle \hat{d}^\dagger_\sigma \hat{d}_\downarrow \rangle_s - f_{l\sigma})}{(\lambda \langle \hat{J}_z \rangle_s + B_z)^2 - 4(is + \epsilon_{lk\sigma})^2 + \lambda^2 \langle \hat{J}_x \rangle_s^2} \\
\langle \hat{c}^\dagger_{lk\sigma} \hat{d}_\downarrow \rangle_s &= \gamma^*_{lk} \frac{(f_{l\sigma}\, \delta_{\sigma\downarrow} - \langle \hat{d}^\dagger_\sigma \hat{d}_\downarrow \rangle_s)}{\epsilon_{lk\sigma} + \frac{1}{2}(\lambda \langle \hat{J}_z \rangle_s + B_z) + is - \frac{1}{2} \frac{\lambda^2 \langle \hat{J}_x \rangle_s^2}{\lambda \langle \hat{J}_z \rangle_s + B_z - 2(is + \epsilon_{lk\sigma})}} \\
&+ \frac{2\gamma^*_{lk} \lambda \langle \hat{J}_x \rangle_s (\langle \hat{d}^\dagger_\sigma \hat{d}_\uparrow \rangle_s - f_{l\sigma})}{(\lambda \langle \hat{J}_z \rangle_s + B_z)^2 - 4(is + \epsilon_{lk\sigma})^2 + \lambda^2 \langle \hat{J}_x \rangle_s^2}
\end{aligned} \tag{C.7}$$

We consider that the interaction between the large spin and the electrons in the leads is negligible, therefore, after expanding in λ and neglecting all terms proportional to $\gamma_{lk}\lambda$, Eqs. (C.7) become:

$$\langle \hat{c}^\dagger_{lk\sigma} \hat{d}_{\sigma'} \rangle_s = \gamma^*_{lk} \left(\frac{1}{\epsilon_{lk\sigma} - (\delta_{\sigma'\uparrow} - \delta_{\sigma'\downarrow}) \frac{B_z}{2} + is} \, (f_{l\sigma}\, \delta_{\sigma\sigma'} - \langle \hat{d}^\dagger_\sigma \hat{d}_{\sigma'} \rangle_s) + \mathcal{O}(\lambda) \right). \tag{C.8}$$

The left lead chemical potential is considered spin-independent ($\mu_{L\uparrow} = \mu_{L\downarrow}$). We focus on the infinite bias regime. Thus, for the left lead $\mu_L \to \infty$, while for the right lead we take $\mu_{R\uparrow} \to -\infty$ and $\mu_{R\downarrow} \to \infty$. Therefore, spin-up electrons are allowed to tunnel through the QD, whereas spin-down electrons become trapped in it. Moreover, this choice of the chemical potentials allows to neglect the effect of the large spin polarization in the Fermi functions, which is the meaning of the approximation done in Eq. (C.8). This choice along with Eq. (C.8) allows us to rewrite the summation that appears in Eq. (C.6a) as follows:

$$\begin{aligned}
&\textstyle\sum_{lk} \left(\gamma_{lk} \langle \hat{c}^\dagger_{lk\sigma} \hat{d}_{\sigma'} \rangle_s - \gamma^*_{lk} \langle \hat{d}^\dagger_\sigma \hat{c}_{lk\sigma'} \rangle_s \right) = \\
&\tfrac{1}{2\pi} \textstyle\int_{-\infty}^{\infty} d\epsilon \left[\frac{\Gamma_{L\sigma}(\epsilon)}{\epsilon - (\delta_{\sigma'\uparrow} - \delta_{\sigma'\downarrow}) \frac{B_z}{2} + is} - \frac{\Gamma_{L\sigma'}(\epsilon)}{\epsilon - (\delta_{\sigma\uparrow} - \delta_{\sigma\downarrow}) \frac{B_z}{2} - is} \right] \times (\delta_{\sigma\sigma'} - \langle \hat{d}^\dagger_\sigma \hat{d}_{\sigma'} \rangle_s) + \\
&\tfrac{1}{2\pi} \textstyle\int_{-\infty}^{\infty} d\epsilon \left[\frac{\Gamma_{R\sigma}(\epsilon)}{\epsilon - (\delta_{\sigma'\uparrow} - \delta_{\sigma'\downarrow}) \frac{B_z}{2} + is} - \frac{\Gamma_{R\sigma'}(\epsilon)}{\epsilon - (\delta_{\sigma\uparrow} - \delta_{\sigma\downarrow}) \frac{B_z}{2} - is} \right] \times (\delta_{\sigma\downarrow} - \langle \hat{d}^\dagger_\sigma \hat{d}_{\sigma'} \rangle_s)
\end{aligned}$$

where:

$$\Gamma_{l\sigma}(\epsilon) = 2\pi\, \rho_{l\sigma}(\epsilon) |\gamma_l(\epsilon)|^2. \tag{C.9}$$

where $\rho_{l\sigma}(\epsilon)$ is the l-the lead density of states. Furthermore, we assume energy-independent tunneling rates $\Gamma_{l\sigma}(\epsilon) = \Gamma_{l\sigma}$ (white band approximation), and use the

Sokhatsky-Weierstrass theorem:

$$\lim_{\eta\to 0}\frac{1}{x\pm i\eta} \;=\; \mathbb{P}\,\frac{1}{x}\mp i\pi\delta(x).$$

Thus, we find that in the long time limit $\varepsilon\to 0$

$$\begin{aligned}\sum_{l,\,k}\left(\gamma_{lk}\langle\hat{c}^{\dagger}_{lk\sigma}\hat{d}_{\sigma'}\rangle_s-\gamma^{*}_{lk}\langle\hat{d}^{\dagger}_{\sigma}\hat{c}_{lk\sigma'}\rangle_s\right) &= \frac{i}{2}\sum_{l}(\Gamma_{l\sigma}+\Gamma_{l\sigma'})\langle\hat{d}^{\dagger}_{\sigma}\hat{d}_{\sigma'}\rangle_s\\ &- i\Gamma_{L\sigma}\delta_{\sigma\sigma'}-i\Gamma_{R\downarrow}\delta_{\sigma\downarrow}. \end{aligned}\tag{C.10}$$

We consider the left lead density of states spin-independent ($\Gamma_{L\uparrow}=\Gamma_{L\downarrow}$). Thus, replacing the previous expression in Eq. (C.6a) gives:

$$\begin{aligned}\langle\hat{n}_\sigma\rangle_s &= \lambda\langle\hat{J}_x\rangle_s\langle\hat{S}_y\rangle_s\,(\delta_{\sigma\uparrow}-\delta_{\sigma\downarrow})-\Gamma\langle\hat{n}_\sigma\rangle_s+\frac{\Gamma_L}{2}+\Gamma_{R\downarrow}\delta_{\sigma\downarrow}\\ s\,\langle S_x\rangle_s &= -\langle\hat{S}_y\rangle_s\left(\lambda\langle\hat{J}_z\rangle_s+B_z\right)-\Gamma\,\langle\hat{S}_x\rangle_s+\langle\hat{S}_x\rangle_0\\ s\,\langle\hat{S}_y\rangle_s &= -\lambda\langle\hat{S}_z\rangle_s\langle\hat{J}_x\rangle_s+\langle\hat{S}_x\rangle_s\left(\lambda\langle\hat{J}_z\rangle_s+B_z\right)-\Gamma\,\langle\hat{S}_y\rangle_s+\langle\hat{S}_y\rangle_0\\ s\,\langle\hat{S}_z\rangle_s &= \lambda\langle\hat{J}_x\rangle_s\langle\hat{S}_y\rangle_s-\Gamma\langle\hat{S}_z\rangle_s-\Gamma_{R\downarrow}\end{aligned}\tag{C.11}$$

where $\Gamma_L=\Gamma_{L\uparrow}+\Gamma_{L\downarrow}$, $\Gamma=\Gamma_L/2+\Gamma_{R(\uparrow,\downarrow)}$ and the identities:

$$\begin{aligned}\hat{S}_x &= \frac{1}{2}\left(\hat{d}^{\dagger}_{\uparrow}\hat{d}_{\downarrow}+\hat{d}^{\dagger}_{\downarrow}\hat{d}_{\uparrow}\right)\\ \hat{S}_y &= \frac{1}{2i}\left(\hat{d}^{\dagger}_{\uparrow}\hat{d}_{\downarrow}-\hat{d}^{\dagger}_{\downarrow}\hat{d}_{\uparrow}\right)\\ \hat{S}_z &= \frac{1}{2}\left(\hat{d}^{\dagger}_{\uparrow}\hat{d}_{\uparrow}-\hat{d}^{\dagger}_{\downarrow}\hat{d}_{\downarrow}\right)\end{aligned}\tag{C.12}$$

have been used. Finally, inverse Laplace transforming Eqs. (C.11) yields the EOMs (5.6) for the occupation and the spin components of the electron in the QD.

The EOM for the total occupancy of the QD is obtained by summing the EOMs of the spin-up and spin-down occupations,

$$\frac{d}{dt}\,\langle\hat{N}\rangle \;=\; -\Gamma\langle\hat{N}\rangle+\Gamma_L+\Gamma_{R\downarrow}.\tag{C.13}$$

Notice that this EOM is independent of the electron and large spins, moreover, it is exactly solvable giving:

$$\langle\hat{N}(t)\rangle \;=\; \langle\hat{N}(0)\rangle\,e^{-\Gamma t}+\frac{\Gamma_L+\Gamma_{R\downarrow}}{\Gamma}\left(1-e^{-\Gamma t}\right)\tag{C.14}$$

C.2 Isotropic model

The EOMs for the completely isotropic case $\lambda_x = \lambda_y = \lambda_z = \lambda$ are

$$\begin{aligned}
\frac{d}{dt}\langle\hat{n}_\sigma\rangle &= \lambda\left(\langle\hat{J}_x\rangle\langle\hat{S}_y\rangle - \langle\hat{J}_y\rangle\langle\hat{S}_x\rangle\right)(\delta_{\sigma\uparrow} - \delta_{\sigma\downarrow}) - \Gamma\langle\hat{n}_\sigma\rangle + \frac{\Gamma_L}{2} + \Gamma_{R\downarrow}\delta_{\sigma\downarrow} \\
\frac{d}{dt}\langle\hat{S}_x\rangle &= \lambda\langle\hat{J}_y\rangle\langle\hat{S}_z\rangle - \left(\lambda\langle\hat{J}_z\rangle + B_z\right)\langle\hat{S}_y\rangle - \Gamma\langle\hat{S}_x\rangle \\
\frac{d}{dt}\langle\hat{S}_y\rangle &= -\lambda\langle\hat{J}_x\rangle\langle\hat{S}_z\rangle + \left(\lambda\langle\hat{J}_z\rangle + B_z\right)\langle\hat{S}_x\rangle - \Gamma\langle\hat{S}_y\rangle \\
\frac{d}{dt}\langle\hat{S}_z\rangle &= \lambda\left(\langle\hat{J}_x\rangle\langle\hat{S}_y\rangle - \langle\hat{J}_y\rangle\langle\hat{S}_x\rangle\right) - \Gamma\langle\hat{S}_z\rangle - \Gamma_{R\downarrow} \\
\frac{d}{dt}\langle\hat{J}_x\rangle &= \lambda\langle\hat{S}_y\rangle\langle\hat{J}_z\rangle - \left(\lambda\langle\hat{S}_z\rangle + B_z\right)\langle\hat{J}_y\rangle \\
\frac{d}{dt}\langle\hat{J}_y\rangle &= -\lambda\langle\hat{S}_x\rangle\langle\hat{J}_z\rangle + \left(\lambda\langle\hat{S}_z\rangle + B_z\right)\langle\hat{J}_x\rangle \\
\frac{d}{dt}\langle\hat{J}_z\rangle &= \lambda\left(\langle\hat{S}_x\rangle\langle\hat{J}_y\rangle - \langle\hat{S}_y\rangle\langle\hat{J}_x\rangle\right).
\end{aligned} \tag{C.15}$$

To find the solutions in the stationary limit we put to zero the time derivatives. Therefore, it can be seen right away that in the long time limit the quantum dot occupations decouple from the large spin components and becomes

$$\langle\hat{n}_\sigma\rangle = \frac{1}{\Gamma}\left(\frac{\Gamma_L}{2} + \Gamma_{R\downarrow}\delta_{\sigma\downarrow}\right). \tag{C.16}$$

Thus, the spin dynamics can not be observed in the current.

C.3 Effective model for region III

In this appendix, we summarize the steps in the derivation of the effective EOMs (Eq. (5.17)) for region III of the parameter space (Fig. 5.2a). Applying the transformation $\langle\hat{\mathbf{S}}\rangle = e^{-\Gamma t}\,\mathcal{R}(t)\cdot\langle\tilde{\mathbf{S}}\rangle$ and $\langle\hat{\mathbf{J}}\rangle = \mathcal{R}(t)\cdot\langle\tilde{\mathbf{J}}\rangle$ with

$$\mathcal{R}(t) = \begin{pmatrix} \cos(B_z t) & -\sin(B_z t) & 0 \\ \sin(B_z t) & \cos(B_z t) & 0 \\ 0 & 0 & 1 \end{pmatrix}, \tag{C.17}$$

to the EOMs (Eq. (5.6)) they become:

$$\begin{aligned}
\frac{d}{dt}\langle\tilde{S}_x\rangle &= -\lambda\left\{\langle\hat{J}_z\rangle\langle\tilde{S}_y\rangle + \left[\langle\tilde{J}_x\rangle\cos(B_z t) - \langle\tilde{J}_y\rangle\sin(B_z t)\right]\langle\tilde{S}_z\rangle\sin(B_z t)\right\} \\
\frac{d}{dt}\langle\tilde{S}_y\rangle &= \lambda\left\{\langle\hat{J}_z\rangle\langle\tilde{S}_x\rangle - \left[\langle\tilde{J}_x\rangle\cos(B_z t) - \langle\tilde{J}_y\rangle\sin(B_z t)\right]\langle\tilde{S}_z\rangle\cos(B_z t)\right\} \\
\frac{d}{dt}\langle\tilde{S}_z\rangle &= \lambda\big[\langle\tilde{J}_x\rangle\langle\tilde{S}_y\rangle\cos^2(B_z t) - \langle\tilde{J}_y\rangle\langle\tilde{S}_x\rangle\sin^2(B_z t) \\
&+ \Big(\langle\tilde{J}_x\rangle\langle\tilde{S}_x\rangle - \langle\tilde{J}_y\rangle\langle\tilde{S}_y\rangle\Big)\sin(B_z t)\cos(B_z t)\big] - \Gamma_{R\downarrow}\, e^{\Gamma t} \\
\frac{d}{dt}\langle\tilde{J}_x\rangle &= -\lambda e^{-\Gamma t}\left\{\langle\tilde{S}_z\rangle\langle\tilde{J}_y\rangle + \left[\langle\tilde{S}_x\rangle\cos(B_z t) - \langle\tilde{S}_y\rangle\sin(B_z t)\right]\langle\hat{J}_z\rangle\sin(B_z t)\right\} \\
\frac{d}{dt}\langle\tilde{J}_y\rangle &= \lambda e^{-\Gamma t}\left\{\langle\tilde{S}_z\rangle\langle\tilde{J}_x\rangle - \left[\langle\tilde{S}_x\rangle\cos(B_z t) - \langle\tilde{S}_y\rangle\sin(B_z t)\right]\langle\hat{J}_z\rangle\cos(B_z t)\right\} \\
\frac{d}{dt}\langle\tilde{J}_z\rangle &= \lambda e^{-\Gamma t}\big[\langle\tilde{S}_x\rangle\langle\tilde{J}_y\rangle\cos^2(B_z t) - \langle\tilde{S}_y\rangle\langle\tilde{J}_x\rangle\sin^2(B_z t) \\
&+ \Big(\langle\tilde{S}_x\rangle\langle\tilde{J}_x\rangle - \langle\tilde{S}_y\rangle\langle\tilde{J}_y\rangle\Big)\sin(B_z t)\cos(B_z t)\big]
\end{aligned} \tag{C.18}$$

Since in the long-time limit $d\langle\tilde{J}_i\rangle/dt \to 0$, we assume $\langle\tilde{\mathbf{J}}\rangle$ to be stationary. Therefore, the EOMs for the electron spin in the original frame become:

$$\frac{d}{dt}\langle\hat{\mathbf{S}}\rangle = \mathbf{B}_{\text{eff}} \times \langle\hat{\mathbf{S}}\rangle - \Gamma\langle\hat{\mathbf{S}}\rangle - \Gamma_{R\downarrow}\,\mathbf{u}_z \tag{C.19}$$

where $\mathbf{B}_{\text{eff}} = (B_{\text{ac}}(t), 0, B_z)$.

Conclusions

In this chapter we enumerate the most relevant conclusions obtained throughout this thesis.

Chapters 3 and 4:

1. The HF interaction between electrons tunneling through a DQD and the nuclei of the host material, induces a dynamical nuclear spin polarization that is in general non-negligible.

2. For strong mixing between the singlet-triplet subspaces, the effective Zeeman splitting difference between the dots is non-negligible with respect to the exchange energy. In this case the leakage current shows a peak. On the contrary, for weak mixing between the singlet-triplet subspaces, the Zeeman splitting difference between dots becomes negligible with respect to the exchange energy, and the system is mostly blocked in the triplet subspace. In this case the leakage current shows a dip. The crossover from a current dip to a current peak is obtained by increasing the HF interaction or decreasing interdot tunneling strength.

3. For a wide external magnetic field sweeping range, the leakage current shows three peaks. Two satellite peaks corresponding to the ST crossings and a central peak corresponding to the triplets crossing.

4. We have observed hysteresis in both the leakage current and the induced nuclear spin polarization as a function of an external magnetic field. This hysteresis behavior is a consequence of the dynamical nuclear spin polarization interacting with the electron spin that tunnel through the DQD structure. We have shown that the size of the hysteresis region strongly depends on the HF interaction intensity and the interdot tunnel strength.

From chapter 5:

1. When the electron spin and the large spin are isotropically coupled, the large spin becomes completely polarized and decouples from the electron spin.

2. When the electron spin and the large spin are anisotropically coupled, we have found that their motion and the current through the QD can either behave as in the isotropic case or show self-sustained oscillations which, furthermore, can be periodic or chaotic. Switching between different behaviors can be obtained by varying either the strength coupling with the leads or the intensity of the external magnetic field.

Conclusiones

En este capítulo enumeramos las conlusiones más importantes derivadas de este trabajo.

De los capítulos 3 y 4:

1. La interacción HF entre los electrones que atraviesan el DQD y los electrones del material hospedador, induce una polarizaión nuclear de espín que, en general, no puede ser ignorada.

2. Cuando los subespacios triplete y singlete están fuertemente mezclados, la diferencia entre los desdoblamientos Zeeman efectivos de cada punto cuántico no es despreciable con respecto a la energía de intercambio. En este caso la corriente de fuga presenta un pico. En cambio, cuando los subespacios triplete y singlete están debilmente mezclados, la differencia entre los desdoblamientos Zeeman es despreciable respecto de la energía de intercambio, y el sistema está mayormente bloqueado en el subespacio de tripletes. En este caso la corriente de fuga presenta un valle. La transición entre el valle y el pico de corriente es obtenida incrementando la intensidad del acoplo HF o disminuyendo la del acoplo túnel entre los puntos cuánticos.

3. Para un barrido amplio del campo magnético externo, la corriente de fuga presenta tres picos. Dos picos satélites que corresponden a los cruces ST y un pico central que corresponde al cruce entre tripletes.

4. Hemos observado histérersis en la corriente de fuga y en la polarización nuclear inducida, en función del campo magnético externo. La histéresis es consecuencia de la interacción entre polarización nuclear dinámica inducida y el espín de los electrones que atraviesan el DQD. El tamaño de la histéresis depende fuertemente de la intensidad del acoplo HF y del acoplo túnel.

Del capítulo 5:

1. Cuando el espín electrónico y el espín grande están acoplados isotrópicamente, el espín grande se polariza completamente y se desacopla del espín del electrón.

2. Cuando el espín del electrón y el espín grande están acoplados anisotrópicamente, sus trayectorias y la corriente a través del QD pueden comportarse como en el caso isotrópico o presentar oscilaciones automantenidas que, a su vez, pueden ser periódicas o caóticas. La transición entre los distintos comportamientos puede obtenerse variando la intensidad del acoplo con los contactos o el campo magnético externo.

Publications

Journal Articles

- *Limit cycles and chaos in the current through a quantum dot*
  C. López-Monís, C. Emary, G. Kiesslich, G. Platero and T. Brandes
  Submitted to Phys. Rev. B (arXiv:1104.3995v1).

- *Dynamical nuclear spin polarization induced by current through double quantum dots*
  C. López-Monís, J. Iñarrea and G. Platero
  New J. Phys. **13**, 053010 (2011).

- *Coherent spin rotations in open driven double quantum dots*
  R. Sánchez, **C. López-Monís**, and G. Platero
  Phys. Rev. B **77**, 165312 (2008)
  Erratum: Coherent spin rotations in open driven double quantum dots [Phys. Rev. B **77***, 165312 (2008)]*
  Phys. Rev. B **79**, 119903 (2009).

- *Tunable nuclear polarization with external stationary fields in weakly coupled quantum dots*
  J. Iñarrea, **C. López-Monís** and G. Platero
  Appl. Phys. Lett. **94**, 252106 (2009).

- *Hysteretic behavior in weakly coupled double-dot transport in spin blockade regime*
  J. Iñarrea, **C. López-Monís**, Allan H. MacDonald and G. Platero
  Appl. Phys. Lett. **91**, 252112 (2007).

Proceedings

- Proceedings of the international conference Frontiers of Quantum and Mesoscopic Thermodynamics FQMT'08.

  - *Spin dynamics in double quantum dots in the spin blockade regime*
    M. Busl, **C. López-Monís**, R. Sánchez, J. Iñarrea and G. Platero
    Physica E **42**, 643-648 (2010).

- Proceedings of the 17th International Conference on Electronic Properties of Two-Dimensional Systems.

  - *Dynamical nuclear polarization in double quantum dots induced by hyperfine interaction*
    J. Iñarrea, **C. López-Monís**, G. Platero and Allan H. MacDonald
    Physica E **40**, 1189-1190 (2008).
  - *Electron spin resonance in double quantum dots*
    R. Sánchez, **C. López-Monís** and G. Platero
    Physica E **40**, 1457-1459 (2008).

- Proceedings of the international conference Trends in Nanotechnology (TNT2007)

  - *Overhauser field-induced electron transport through weakly coupled double quantum dots*
    J. Iñarrea, Allan H. MacDonald, **C. López-Monís** and G. Platero
    Phys. Stat. Sol. (a) **205**, 1266-1269 (2008).

Bibliography

[1] U. Woggon, Optical Properties of Semiconductor Quantum Dots. Berlin Heidelberg New York: Springer-Verlag, 1996.

[2] E. Borovitskaya and M. S. Shur, eds., Quantum Dots. New Jersey London Singapure Hong Kong: World Scientific, 2002.

[3] M. A. Reed, J. N. Randall, R. J. Aggarwal, R. J. Matyi, T. M. Moore, and A. E. Wetsel, "Observation of discrete electronic states in a zero-dimensional semiconductor nanostructure," Phys. Rev. Lett., vol. 60, pp. 535–537, Feb 1988.

[4] H. P. Rooksby, "The colour of selenium ruby glasses," J. Soc. Glass Techn., vol. XVI, p. 171, 1932.

[5] A. I. Ekimov and A. A. Onushchenko, "Quantum size effect in three-dimensional microscopic semiconductor crystals," Pis'ma Zh. Eksp. Teor. Fiz., vol. 34, pp. 363–366, September 1981.

[6] A. I. Ekimov, A. I. Efros, and A. A. Onushchenko, "Quantum size effect in semiconductor microcrystals," Sol. State Comm., vol. 56, pp. 921–924, September 1985.

[7] R. Rossetti, S. Nakahara, and L. E. Brus, "Quantum size effects in the redox potentials, resonance raman spectra, and electronic spectra of cds crystallites in aqueous solution," J. Chem. Phys, vol. 79, no. 2, pp. 1086–1088, 1983.

[8] R. Rossetti, J. L. Ellison, J. M. Gibson, and L. E. Brus, "Size effects in the excited electronic states of small colloidal cds crystallites," J. Chem. Phys, vol. 80, no. 9, pp. 4464–4469, 1984.

[9] P. A. Maksym and T. Chakraborty, "Quantum dots in a magnetic field: Role of electron-electron interactions," Phys. Rev. Lett., vol. 65, pp. 108–111, Jul 1990.

[10] M. A. Kastner, "Artificial atoms," vol. 46, no. 1, pp. 24–31, 1993.

[11] S. Tarucha, D. G. Austing, T. Honda, R. J. van der Hage, and L. P. Kouwenhoven, "Shell filling and spin effects in a few electron quantum dot," Phys. Rev. Lett., vol. 77, pp. 3613–3616, Oct 1996.

[12] J. H. Davies, The Physics of Low-Dimensional Semiconductors. Cambridge: Cambridge University Press, 1998.

[13] T. Chakraborty, Quantum Dots. Amsterdam: Elsevier Science S. V., 1999.

[14] H. Bruus and K. Flensberg, Many-Body Quantum Theory in Condensed Matter Physics. Oxford: Oxford University Press, 2004.

[15] R. L. Liboff, Introductory Quantum Mechanics. U.S.A.: Addison-Wesley, 1980.

[16] N. W. Ashcroft and N. D. Mermin, Solid State Physics. U.S.A.: Harcourt College Publishers, 1976.

[17] V. I. Klimov, ed., Semiconductor and Metal Nanocrystals. U.S.A.: Marcel Dekker, 2004.

[18] A. T. Johnson, L. P. Kouwenhoven, W. de Jong, N. C. van der Vaart, C. J. P. M. Harmans, and C. T. Foxon, "Zero-dimensional states and single electron charging in quantum dots," Phys. Rev. Lett., vol. 69, pp. 1592–1595, Sep 1992.

[19] V. Fock Z. Phys., vol. 47, pp. 446–448, 1928.

[20] C. G. Darwin Proc. Cambridge Philos. Soc., vol. 27, p. 86, 1930.

[21] L. P. Kouwenhoven, T. H. Oosterkamp, M. W. S. Danoesastro, M. Eto, D. G. Austing, T. Honda, and S. Tarucha, "Excitation spectra of circular, few-electron quantum dots," Science, vol. 278, no. 5344, pp. 1788–1792, 1997.

[22] R. Hanson, L. P. Kouwenhoven, J. R. Petta, S. Tarucha, and L. M. K. Vandersypen, "Spins in few-electron quantum dots," Rev. Mod. Phys., vol. 79, pp. 1217–1265, Oct 2007.

[23] S. Datta, Electronic Transport in Mesoscopic Systems. Cambridge: Cambridge University Press, 1995.

[24] H. Grabert and M. H. Devoret, eds., Single Charge Tunneling. New York: Plenum Press, 1992.

[25] D. Weinmann, "The physics of mesoscopic systems," lectures held during the seventh petra school of physics, Institut de Physique et Chimie des Matériaux de Strasbourg, 2005.

[26] T. Ihm, Semiconductor Nanostructures. Oxford: Oxford University Press, 2010.

[27] Y. Meir, N. S. Wingreen, and P. A. Lee, "Transport through a strongly interacting electron system: Theory of periodic conductance oscillations," Phys. Rev. Lett., vol. 66, pp. 3048–3051, Jun 1991.

[28] C. W. J. Beenakker, "Theory of coulomb-blockade oscillations in the conductance of a quantum dot," Phys. Rev. B, vol. 44, pp. 1646–1656, Jul 1991.

[29] G. D. Mahan, Many-Particle Physics. New York: Kluwer Academic / Plenum Publishers, 2000.

[30] A. C. Hewson, ed., The Kondo Problem to Heavy Fermions. Cambridge: Cambridge University Press, 1993.

[31] P. W. Anderson, "Localized magnetic states in metals," Phys. Rev., vol. 124, pp. 41–53, Oct 1961.

[32] D. Loss and D. P. DiVincenzo, "Quantum computation with quantum dots," Phys. Rev. A, vol. 57, pp. 120–126, Jan 1998.

[33] K. Ono, D. G. Austing, Y. Tokura, and S. Tarucha, "Current Rectification by Pauli Exclusion in a Weakly Coupled Double Quantum Dot System," Science, vol. 297, no. 5585, pp. 1313–1317, 2002.

[34] F. H. L. Koppens, J. A. Folk, J. M. Elzerman, R. Hanson, L. H. W. van Beveren, I. T. Vink, H. P. Tranitz, W. Wegscheider, L. P. Kouwenhoven, and L. M. K. Vandersypen, "Control and Detection of Singlet-Triplet Mixing in a Random Nuclear Field," Science, vol. 309, no. 5739, pp. 1346–1350, 2005.

[35] A. Pfund, I. Shorubalko, K. Ensslin, and R. Leturcq, "Suppression of spin relaxation in an InAs nanowire double quantum dot," Phys. Rev. Lett., vol. 99, p. 036801, Jul 2007.

[36] N. Shaji, C. B. Simmons, M. Thalakulam, L. J. Klein, H. Qin, H. Luo, D. E. Savage, M. Lagally, A. J. Rimberg, R. Joynt, M. Friesen, R. H. Blick, S. N. Coppersmith, and M. A. Eriksson, "Spin-blockade and lifetime-enhanced transport in a few Si/SiGe double quantum dot," Nature Physics, vol. 4, pp. 540–544, July 2008.

[37] B. A. J. Churchill, H. O. H., J. W. Harlow, F. Kuemmeth, D. Marcos, C. H. Stwertka, S. K. Watson, and C. M. Marcus, "Electron-nuclear interaction in C13 nanotube double quantum dots," Nature Physics, vol. 5, pp. 321–326, May 2009.

[38] A. V. Khaetskii and Y. V. Nazarov, "Spin relaxation in semiconductor quantum dots," Phys. Rev. B, vol. 61, pp. 12639–12642, May 2000.

[39] A. C. Johnson, J. R. Petta, C. M. Marcus, M. P. Hanson, and A. C. Gossard, "Singlet-triplet spin blockade and charge sensing in a few-electron double quantum dot," Phys. Rev. B, vol. 72, p. 165308, Oct 2005.

[40] A. B. Vorontsov and M. G. Vavilov, "Spin relaxation in quantum dots due to electron exchange with leads," Phys. Rev. Lett., vol. 101, p. 226805, Nov 2008.

[41] K. Ono and S. Tarucha, "Nuclear-spin-induced oscillatory current in spin-blockaded quantum dots," Phys. Rev. Lett., vol. 92, p. 256803, Jun 2004.

[42] J. R. Petta, A. C. Johnson, J. M. Taylor, E. A. Laird, A. Yacoby, M. D. Lukin, C. M. Marcus, M. P. Hanson, and A. C. Gossard, "Coherent Manipulation of Coupled Electron Spins in Semiconductor Quantum Dots," Science, vol. 309, no. 5744, pp. 2180–2184, 2005.

[43] F. H. L. Koppens, D. Klauser, W. A. Coish, K. C. Nowack, L. P. Kouwenhoven, D. Loss, and L. M. K. Vandersypen, "Universal phase shift and nonexponential decay of driven single-spin oscillations," Phys. Rev. Lett., vol. 99, p. 106803, Sep 2007.

[44] J. Baugh, Y. Kitamura, K. Ono, and S. Tarucha, "Large nuclear overhauser fields detected in vertically coupled double quantum dots," Phys. Rev. Lett., vol. 99, p. 096804, Aug 2007.

[45] J. R. Petta, J. M. Taylor, A. C. Johnson, A. Yacoby, M. D. Lukin, C. M. Marcus, M. P. Hanson, and A. C. Gossard, "Dynamic nuclear polarization with single electron spins," Phys. Rev. Lett., vol. 100, p. 067601, Feb 2008.

[46] D. J. Reilly, J. M. Taylor, J. R. Petta, C. M. Marcus, M. P. Hanson, and A. C. Gossard, "Suppressing Spin Qubit Dephasing by Nuclear State Preparation," Science, vol. 321, no. 5890, pp. 817–821, 2008.

[47] J. Danon, I. T. Vink, F. H. L. Koppens, K. C. Nowack, L. M. K. Vandersypen, and Y. V. Nazarov, "Multiple nuclear polarization states in a double quantum dot," Phys. Rev. Lett., vol. 103, p. 046601, Jul 2009.

[48] M. Gullans, J. J. Krich, J. M. Taylor, H. Bluhm, B. I. Halperin, C. M. Marcus, M. Stopa, A. Yacoby, and M. D. Lukin, "Dynamic nuclear polarization in double quantum dots," Phys. Rev. Lett., vol. 104, p. 226807, Jun 2010.

[49] M. Eto, T. Ashiwa, and M. Murata, "Current-induced entanglement of nuclear spins in quantum dots," Journal of the Physical Society of Japan, vol. 73, no. 2, pp. 307–310, 2004.

[50] O. N. Jouravlev and Y. V. Nazarov, "Electron transport in a double quantum dot governed by a nuclear magnetic field," Phys. Rev. Lett., vol. 96, p. 176804, May 2006.

[51] M. S. Rudner and L. S. Levitov, "Self-polarization and dynamical cooling of nuclear spins in double quantum dots," Phys. Rev. Lett., vol. 99, p. 036602, Jul 2007.

[52] F. Qassemi, W. A. Coish, and F. K. Wilhelm, "Stationary and transient leakage current in the pauli spin blockade," Phys. Rev. Lett., vol. 102, p. 176806, Apr 2009.

[53] J. Iñarrea, G. Platero, and A. H. MacDonald, "Electronic transport through a double quantum dot in the spin-blockade regime: Theoretical models," Phys. Rev. B, vol. 76, p. 085329, Aug 2007.

[54] F. Domínguez and G. Platero, "Hyperfine mediated triplet-singlet transition probability in a double-quantum-dot system: Analogy with the double-slit experiment," Phys. Rev. B, vol. 80, p. 201301, Nov 2009.

[55] J. Iñarrea, C. López-Monís, A. H. MacDonald, and G. Platero, "Hysteretic behavior in weakly coupled double-dot transport in the spin blockade regime," Applied Physics Letters, vol. 91, no. 25, p. 252112, 2007.

[56] J. Iñarrea, C. López-Monís, and G. Platero, "Tunable nuclear polarization with external stationary fields in weakly coupled double quantum dots," Applied Physics Letters, vol. 94, no. 25, p. 252106, 2009.

[57] J. Fischer, B. Trauzettel, and D. Loss, "Hyperfine interaction and electron-spin decoherence in graphene and carbon nanotube quantum dots," Phys. Rev. B, vol. 80, p. 155401, Oct 2009.

[58] I. A. Merkulov, A. L. Efros, and M. Rosen, "Electron spin relaxation by nuclei in semiconductor quantum dots," Phys. Rev. B, vol. 65, p. 205309, Apr 2002.

[59] W. A. Coish and D. Loss, "Singlet-triplet decoherence due to nuclear spins in a double quantum dot," Phys. Rev. B, vol. 72, p. 125337, Sep 2005.

[60] B. Erbe and J. Schliemann, "Hyperfine induced spin and entanglement dynamics in double quantum dots: A homogeneous coupling approach," Phys. Rev. B, vol. 81, p. 235324, Jun 2010.

[61] A. Khaetskii, D. Loss, and L. Glazman, "Electron spin evolution induced by interaction with nuclei in a quantum dot," Phys. Rev. B, vol. 67, p. 195329, May 2003.

[62] C. P. Slichter, Principles of Magnetic Resonance. New York: Harper & Row, 1963.

[63] T. Fujisawa, T. H. Oosterkamp, W. G. van der Wiel, B. W. Broer, R. Aguado, S. Tarucha, and L. P. Kouwenhoven, "Spontaneous Emission Spectrum in Double Quantum Dot Devices," Science, vol. 282, no. 5390, pp. 932–935, 1998.

[64] K. Blum, Density Matrix Theory and Applications. New York: Plenum Press, 1996.

[65] J. H. Kim, I. D. Vagner, and L. Xing, "Phonon-assisted mechanism for quantum nuclear-spin relaxation," Phys. Rev. B, vol. 49, pp. 16777–16780, Jun 1994.

[66] S. I. Erlingsson, Y. V. Nazarov, and V. I. Fal'ko, "Nucleus-mediated spin-flip transitions in gaas quantum dots," Phys. Rev. B, vol. 64, p. 195306, Oct 2001.

[67] M. Prada, R. H. Blick, and R. Joynt, "Singlet-triplet relaxation in two-electron silicon quantum dots," Phys. Rev. B, vol. 77, p. 115438, Mar 2008.

[68] A. K. Hüttel, J. Weber, A. W. Holleitner, D. Weinmann, K. Eberl, and R. H. Blick, "Nuclear spin relaxation probed by a single quantum dot," Phys. Rev. B, vol. 69, p. 073302, Feb 2004.

[69] S. H. Strogatz, Nonlinear Dynamics and Chaos. Cambridge: Westview Press, 2000.

[70] H. Grabert and M. H. Devoret, eds., Single Charge Tunneling. New York: Plenum Press, 1992.

[71] R. Hanson, L. P. Kouwenhoven, J. R. Petta, S. Tarucha, and L. M. K. Vandersypen, "Spins in few-electron quantum dots," Rev. Mod. Phys., vol. 79, pp. 1217–1265, Oct 2007.

[72] G. Shinkai, T. Hayashi, T. Ota, and T. Fujisawa, "Correlated coherent oscillations in coupled semiconductor charge qubits," Phys. Rev. Lett., vol. 103, p. 056802, Jul 2009.

[73] S. Andergassen, V. Meden, H. Schoeller, J. Splettstoesser, and M. R. Wegewijs, "Charge transport through single molecules, quantum dots and quantum wires," Nanotechnology, vol. 21, no. 27, p. 272001, 2010.

[74] S. M. Reimann and M. Manninen, "Electronic structure of quantum dots," Rev. Mod. Phys., vol. 74, pp. 1283–1342, Nov 2002.

[75] P. Roulleau, S. Baer, T. Choi, F. Molitor, J. Güttinger, T. Müller, S. Dröscher, K. Ensslin, and T. Ihn, "Coherent electronphonon coupling in tailored quantum systems," Nat. Commun., vol. 2, p. 239, Mar 2011.

[76] Y. V. Nazarov, ed., Quantum Noise in Mesoscopic Physics. Dordrecht: Kluwer Academic Publishers, 2003.

[77] T. Fujisawa, T. Hayashi, R. Tomita, and Y. Hirayama, "Bidirectional counting of single electrons," vol. 312, no. 5780, pp. 1634–1636, 2006.

[78] S. Gustavsson, R. Leturcq, B. Simovič, R. Schleser, T. Ihn, P. Studerus, K. Ensslin, D. C. Driscoll, and A. C. Gossard, "Counting statistics of single electron transport in a quantum dot," Phys. Rev. Lett., vol. 96, p. 076605, Feb 2006.

[79] E. M. Hankiewicz, J. Li, T. Jungwirth, Q. Niu, S.-Q. Shen, and J. Sinova, "Charge hall effect driven by spin-dependent chemical potential gradients and onsager relations in mesoscopic systems," Phys. Rev. B, vol. 72, p. 155305, Oct 2005.

[80] H. Ebrahimnejad, Y. Ren, S. M. Frolov, I. Adagideli, J. A. Folk, and W. Wegscheider, "Measurement of spin-dependent conductivities in a two-dimensional electron gas," Phys. Rev. B, vol. 82, p. 041305, Jul 2010.

[81] M. Feingold and A. Peres, "Regular and chaotic motion of coupled rotators," Physica D: Nonlinear Phenomena, vol. 9, no. 3, pp. 433 – 438, 1983.

[82] A. Peres, "Ergodicity and mixing in quantum theory. i," Phys. Rev. A, vol. 30, pp. 504–508, Jul 1984.

[83] M. Feingold, N. Moiseyev, and A. Peres, "Ergodicity and mixing in quantum theory. ii," Phys. Rev. A, vol. 30, pp. 509–511, Jul 1984.

[84] E. Magyari, H. Thomas, R. Weber, C. Kaufman, and G. Müller, "Integrable and nonintegrable classical spin clusters," Zeitschrift für Physik B Condensed Matter, vol. 65, pp. 363–374, 1987.

[85] D. T. Robb and L. E. Reichl, "Chaos in a two-spin system with applied magnetic field," Phys. Rev. E, vol. 57, pp. 2458–2459, Feb 1998.

[86] R. Hussein, A. Metelmann, P. Zedler, and T. Brandes, "Semiclassical dynamics of nanoelectromechanical systems," Phys. Rev. B, vol. 82, p. 165406, Oct 2010.

[87] N. Bode, S. V. Kusminskiy, R. Egger, and F. von Oppen, "Scattering theory of current-induced forces in mesoscopic systems," 2011.

[88] A. V. Khaetskii, D. Loss, and L. Glazman, "Electron spin decoherence in quantum dots due to interaction with nuclei," Phys. Rev. Lett., vol. 88, p. 186802, Apr 2002.

[89] C. López-Monís, J. I. narrea, and G. Platero, "Dynamical nuclear spin polarization induced by electronic current through double quantum dots," New Journal of Physics, vol. 13, no. 5, p. 053010, 2011.

[90] J. Fernández-Rossier and R. Aguado, "Single-electron transport in electrically tunable nanomagnets," Phys. Rev. Lett., vol. 98, p. 106805, Mar 2007.

[91] G. Kiesslich, G. Schaller, C. Emary, and T. Brandes, "Single spin transport spectroscopy: Current blockade and spin decay," Applied Physics Letters, vol. 95, no. 15, p. 152104, 2009.

[92] F. Elste and C. Timm, "Resonant and kondo tunneling through molecular magnets," Phys. Rev. B, vol. 81, p. 024421, Jan 2010.

[93] B. Sothmann and J. König, "Transport through quantum-dot spin valves containing magnetic impurities," Phys. Rev. B, vol. 82, p. 245319, Dec 2010.

[94] H. B. Heersche, Z. de Groot, J. A. Folk, H. S. J. van der Zant, C. Romeike, M. R. Wegewijs, L. Zobbi, D. Barreca, E. Tondello, and A. Cornia, "Electron transport through single mn_{12} molecular magnets," Phys. Rev. Lett., vol. 96, p. 206801, May 2006.

[95] L. Bogani and W. Wernsdorfer, "Molecular spintronics using single-molecule magnets," Nature Materials, vol. 7, p. 179, 2008.

[96] J. R. Friedman and M. P. Sarachik, "Single-molecule nanomagnets," Annu. Rev. Cond. Mat., vol. 1, p. 109, 2010.

[97] C. W. J. Beenakker, "Random-matrix theory of quantum transport," Rev. Mod. Phys., vol. 69, pp. 731–808, Jul 1997.

[98] Y. Alhassid, "The statistical theory of quantum dots," Rev. Mod. Phys., vol. 72, pp. 895–968, Oct 2000.

[99] W. A. Coish and J. Baugh, "Nuclear spins in nanostructures," physica status solidi (b), vol. 246, no. 10, pp. 2203–2215, 2009.

[100] J. S. Hodges, J. C. Yang, C. Ramanathan, and D. G. Cory, "Universal control of nuclear spins via anisotropic hyperfine interactions," Phys. Rev. A, vol. 78, p. 010303, Jul 2008.

[101] J. Fischer, B. Trauzettel, and D. Loss, "Hyperfine interaction and electron-spin decoherence in graphene and carbon nanotube quantum dots," Phys. Rev. B, vol. 80, p. 155401, Oct 2009.

[102] P. Henelius and R. S. Fishman, "Hybrid quantum-classical monte carlo study of a molecule-based magnet," Phys. Rev. B, vol. 78, p. 214405, Dec 2008.